Development of a Vehicle Stability Control Strategy for a Hybrid Electric Vehicle Equipped With Axle Motors

DISSERTATION

Presented in Partial Fulfillment of the Requirements for the Degree of Doctor of Philosophy in the Graduate School of The Ohio State University

By

Kerem Bayar, B.S., M.S.

Graduate Program in Mechanical Engineering

The Ohio State University

2011

Dissertation Committee:

Prof. Giorgio Rizzoni, Adviser

Prof. Junmin Wang, Co-adviser

Prof. Dennis Guenther

Dr. Gary Heydinger

Dr. Michael Pennell

© Copyright by

Kerem Bayar

2011

Abstract

Hybrid-electric vehicles have been available to consumers for over a decade, and plug-in hybrid and pure electric vehicles are rapidly becoming mainstream products with the introduction of vehicles such as the Chevrolet Volt and the Nissan Leaf in 2011. These vehicles have in common an electric powertrain, comprised of one or more electric motors and of a battery pack which in the case of hybrid vehicles supplements and internal combustion engine. It is well understood that hybrid and electric vehicles have the benefit of significant reduction in CO_2 emissions and in the use of petroleum as a fuel. However, one additional benefit of hybrid and electric vehicles remains so far under-utliized: the use of the electric traction system to enhance vehicle stability control. This potentially or low cost feature could provide additional motivation for customers to choose hybrid or electric vehicles over conventional ones.

This dissertation documents the conception and development of a novel control strategy to allocate braking and tractive forces in a hybrid electric vehicle equipped with axle motors, for the purpose of enhancing the vehicle stability control system. The work described in this dissertation documents the development of a hierarchical control strategy, its design and stability proofs, and its evaluation using software and model in-the-loop methods.

The work includes the development of a dynamic HEV simulator that is capable of evaluating vehicle dynamics responses during emergency maneuvers, to demonstrate its stability. For this purpose, a hybrid powertrain simulation model including batteries, motors, differential, shaft, wheel, and electro-hydraulic brake system models are developed. Furthermore, a simple yet reliable vehicle dynamics model is integrated with the powertrain model to capture longitudinal, lateral, yaw and roll degrees of freedoms of the vehicle. The development of the simulator is a minor, but an original contribution of this dissertation.

The principal contribution of this work is a novel and systematic vehicle stability control (VSC) strategy that distributes the corrective longitudinal force and yaw moment action to generate individual wheel slip ratios by blending regenerative axle motor braking and/or traction with individual wheel braking; so as to track the desired vehicle speed and yaw rate without causing excessive vehicle sideslip angles. This dissertation shows that including the axle electric motors within the proposed VSC frame, improves the performance of vehicle stability control in comparison to production vehicle VSC strategies. The potential benefit of electric motors, namely their ability to provide rapid braking/tractive torque actuation, is utilized in addition to the friction brakes within the proposed VSC scheme. The resulting strategy is the first published result that shows that yaw tracking and vehicle stabilization can be performed without interfering in the driver's longitudinal speed demand. Furthermore, the strategy limits the yaw rate in order to keep the vehicle sideslip angle in the safe range, by increasing the understeer coefficient whenever a sideslip angle safety threshold is exceeded. A secondary benefit of the proposed VSC scheme is its energy saving feature, thanks to the use of highly efficient electric motors and their regenerative braking capability in comparison to a standard vehicle stability control schemes that use only the brake and engine intervention.

Finally, the proposed VSC strategy is tested in real time, by using a model-in-the-loop simulation set-up, using state-of-the-art hardware-in-the-loop computer systems. Model-in-the-loop simulation results for different road conditions and steering maneuvers showed that the proposed VSC performs satisfactorily in real time as well, suggesting that is amenable to in-vehicle implementation.

Dedication.

Leyla Bayar ve Akif Bayar’a adanmıştır.

Acknowledgments

I express my deepest gratitude to my adviser Prof. Giorgio Rizzoni for his guidance, criticism, encouragements and logistic support throughout the research. Special thanks go to my co-adviser Prof. Junmin Wang for the advice and direction he gave me without which this work could not have been conducted.

Also, I am grateful to other members of my dissertation committee, Prof. Dennis Guenther and Dr. Gary Heydinger who have contributed to this work with valuable suggestions. I feel very privileged to have all of you in my dissertation committee.

Finally, I would like to thank my parents, Akif Bayar and Leyla Bayar by heart, for their moral support and self-sacrifice throughout my whole life. I offer sincere thanks to my elder brother Fırat Bayar, my grandparents Özden and Şerafettin Seyhun, and my former “yol arkadaşım” Tuğba Özal for their support in moral and academic respect.

Vita

February, 1982	Born, Ankara, Turkey.
June, 2004	B.S. Mechanical Engineering Middle East Technical University Ankara, Turkey.
July, 2006.	M.S. Mechanical Engineering Middle East Technical University Ankara, Turkey.
October, 2007 to present	Graduate Research Associate, Center for Automotive Research, The Ohio State University, Columbus, OH

Publications

Bayar, K., Wang, J. and Rizzoni, G. 2011. "Development of a vehicle stability control strategy for a hybrid electric vehicle equipped with axle motors", *Proceedings of the IMechE, Part D: Journal of Automobile Engineering*, in revision.

Schacht, E., Bexaire, B., Cooley, B., **Bayar, K.**, and Kruckenberg, J. 2011. “Addressing Drivability in an Extended Range Electric Vehicle Running an Equivalent Consumption Minimization Strategy (ECMS)”, *SAE* paper 2011-01-0911.

Bayar, K., Biasini, R., Onori, S. and Rizzoni. G. 2011 **“**Modeling and control of a brake system for an extended range electric vehicle equipped with axle motors”, *International Journal of Vehicle Design*, in press.

Bayar, K., Bezaire, B., Cooley, B., Kruckenberg, J., Schacht, E., Midlam-Mohler, S., and Rizzoni, G. 2010. “Design of an Extended-Range Electric Vehicle for the EcoCAR Challenge”, *ASME 2010 International Design Engineering Technical Conferences & Computers and Information in Engineering Conference*, Montreal, Canada.

Bayar, K., and Arnett, M. 2008. "Modeling and Testing of a Traction Control System Applied to the Challenge X Competition Vehicle", *SAE All-Wheel Drive Vehicle Symposium*, Ann Arbor, MI, USA.

Sevel, K., Arnett, M., Koprubasi, K., Coburn, C., Shakiba-Herfeh, M., **Bayar, K.,** Rizzoni, G., Guezennec, Y., and Midlam-Mohler, S. 2008 "Cleaner Diesel Using Model-Based Design and Advanced Aftertreatment in a Student Competition Vehicle", *SAE Paper* 2008-01-0868.

Fields of Study

Major Field: Mechanical Engineering

Table of Contents

List of Tables

List of Figures

Abbreviations and Nomenclature

Abbreviations

ABS	Antiblockier/Anti-blocking system
ASR	Antriebsschlupfregelung/Anti-slip regulation
DOF	Degree of freedom
EBD	Electronic brake distribution
EcoDYN	EcoCAR dynamic simulator
ECU	Electronic control unit
EDL	Electronic differential lock
EHB	Electro-hydraulic braking
ESP	Elektronisches Stabilitätsprogramm
EV	Electric vehicle
FEM	Front electric motor
FLOP	Floating point operations
HEV	Hybrid electric vehicle
HIL	Hardware in the loop
ICE	Internal combustion engine
MIL	Model in the loop
NHTSA	National Highway and Traffic Safety Administration

PHEV	Plug-in hybrid electric vehicle
REM	Rear electric motor
RMS	Root mean square
SIL	Software in the loop
SUV	Sport utility vehicle
TCS	Traction control system
VSC	Vehicle stability control

Nomenclature

a	distance from center of gravity to front axle
a_y	lateral acceleration
A	orifice cross sectional area
A_B	brake disc friction area
b	distance from center of gravity to rear axle
c	sliding mode controller coefficient for the error
c_{hs}	half shaft damping coefficient
d	sliding mode controller coefficient for the integral of the error
C_f	cornering stiffness of front tires
C_r	cornering stiffness of rear tires
C_ϕ	roll damping
F_{xi}	longitudinal force for the ith wheel

$\hat{F}_{xi}$	estimated ith longitudinal force
$\tilde{F}_{xi}$	estimation error for the ith longitudinal force
F_{desb}	desired braking torque
F_{dest}	desired tractive torque
F_{yi}	lateral force for the ith wheel
F_{zi}	normal load on the ith wheel
g	gravitational acceleration
h	height of center of gravity
h_s	vertical distance between the roll axis and the center of gravity
i_{in}	differential inner gear reduction ratio
I_{em}	electric motor output shaft inertia
i_{main}	differential main gear reduction ratio
I_{input}	differential input gear inertia
I_{batt}	battery current
I_{cage}	differential cage inertia
I_z/I_{zz}	yaw moment of inertia
I_{zz0}	nominal yaw moment of inertia
I_{xx}	roll moment of inertia
I_{xz}	product of inertia
k	sliding mode controller convergence rate constant
k_{hs}	half shaft stiffness
K	sliding mode controller gain

$K_{\phi f}$	front roll stiffness
$K_{\phi r}$	rear roll stiffness
l	wheelbase
L_{look}	look ahead distance
M_s	sprung mass
M	vehicle mass
M_0	nominal vehicle mass
p	roll rate
p_{acc}	accumulator pressure
p_a	ambient pressure
p_c	wheel brake cylinder pressure
P_{acc}	accessory power
P_{batt}	battery power
q_{acc}	accumulator flow rate
q_c	flow rate into the wheel brake cylinder
$q_{I/O}$	flow rate through the input/output valves
r	yaw rate
r_B	radius between the brake disc contact point and center of the wheel
r_{des}	desired yaw rate
r_w	tire rolling radius
R_{batt}	battery equivalent resistance
R	radius of curvature of the trajectory

s_i	longitudinal slip of the ith wheel
s_{ides}	desired longitudinal slip for the ith wheel
S	sliding mode surface
t	track
T_{EHBi}	electro-hydraulic brake torque for the ith wheel
T_{EMmaxi}	maximum torque limit of the ith electric motor torque
T_{EMmini}	minimum torque limit of the ith electric motor torque
T_{fbref}	reference friction brake torque
T_{fb}	actual friction brake torque
T_i	net wheel torque for the ith wheel
T_{ICE}	engine torque
T_{lhs}	left half shat torque
T_{rhs}	right half shat torque
T_{act}	actual motor torque
T_{req}	requested motor torque
u	control allocation variable vector
$u_{I/Oi}$	control variable for the ith inlet/outlet valve
v	virtual control input
V_{batt}	voltage at the battery terminals
V_0	initial volume of the fluid in the accumulator
V_{oc}	Open circuit voltage
V_x	longitudinal velocity

V_{xdes}	desired longitudinal velocity
V_y	lateral velocity
V_i	velocity across ith wheel plane
V_c	volume of the fluid inside the wheel brake cylinder
W_u	weighting matrix for control energy
W_v	weighting matrix for control accuracy
w_x	disturbance and unmodeled dynamics on longitudinal motion
w_z	disturbance and unmodeled dynamics on yaw motion
x^*	estimated longitudinal distance
y^*	estimated lateral distance
x	actual longitudinal distance
y	actual lateral distance
α	accelerator pedal position
α_i	slip angle of the ith wheel
β	brake pedal position/sideslip angle
δ	steering wheel angle
ϕ	roll angle
Φ	boundary layer thickness of the saturation function
η_{em}	motor efficiency
η_{ice}	engine efficiency
κ	polytropic gas constant
μ	coefficient of friction

ω_{ice}	engine speed
ω_i	ith wheel speed
ω_{fem}	front electric motor speed
ω_{lhs}	left half-shaft speed
ω_{rem}	rear electric motor speed
ω_{rhs}	right half-shaft speed

subscript i	wheel orientation, front right, front left, rear right or rear left

1. Introduction

1.1. Motivation

The concept of Hybrid Electric Vehicles (HEV) is one of the more important trends in today's automotive industry. HEVs are rapidly entering the mainstream and are now produced in a variety of powertrain configurations to meet the high standards of automobile consumers and the stringent requirements of government regulations on fuel economy and emissions. It is predicted by HEV experts that, plug-in hybrid electric vehicles (PHEV), which are one step further in the field of vehicle electrification, will become very popular by 2016 as the demand for energy efficient vehicles increase [1-3]. PHEVs share the characteristics of both a conventional HEV, having an electric motor and an internal combustion engine, and of an all-electric vehicle (EV), also having a plug to connect to the electrical grid.

Another important advancement in the automotive systems is the concept of active safety systems. Contrary to their passive conjugates, active safety systems aim to prevent accidents by detecting any jeopardy of instability and take partial or full control of the vehicle to take appropriate measures necessary for prevention of the accident. With the significant amount of research on safety applications in last few decades, several independent active safety applications have been developed. The oldest, most known and successful example is the anti-lock braking system (ABS) [4] which prevents locking of wheels during braking. After the significant success of ABS, several other independent active safety systems have been developed such as anti slip regulation (ASR) [4], i.e. traction control system which is based on ABS sensor systems but manipulating the actuators during acceleration period rather than during braking. Other systems include electronic brake distribution [4] (EBD) system which controls the distribution of the front and rear brake forces, electronic differential lock (EDL) system for better traction on surfaces with non-uniform friction characteristics and electronic stability program (ESP) [4], or Vehicle Stability Control (VSC), which intends to prevent potentially unstable yaw and lateral motion (drifting, spinning etc.) by controlling the individual brakes, and creating a contra-yaw moment.

In this context, the motivation that initiated this study is the potential to integrate vehicle hybridization and active safety systems. An observation that leads to this motivation is that the aforementioned active safety systems ABS, ASR or ESP are usually supplied to automotive companies as stand-alone subsystems. If a vehicle using one of the these active safety systems is also designed to have a hybrid powertrain, the braking and friction capabilities provided by the electric machines are disabled during activation of the active safety features.

With this background in place, it should be clear that including the axle electric motors (specifically for the hybrid SUV considered in this study) within the proposed VSC scheme may improve the performance of the vehicle stability control system. The potential benefit of electric motors is that they are capable of providing rapid braking/tractive torque actuation, unlike an internal combustion engine, in addition to the friction brakes.

Introduction of the braking capability of electric motors in addition to individual wheel brakes provides an additional degree of actuation freedom leading to another motivational point in design of a new VSC scheme: How should the corrective yaw moment and tractive/braking force be distributed to individual wheel brakes and axle motors? This is a problem that has not been heretofore addressed in the literature. For instance fuzzy brake based control, which is a very common approach in industry, has not been compared with methods that apply formal optimization techniques, i.e. control allocation techniques, to distribute the corrective moment/force to different actuators. In addition to performance consideration, it may also be interesting to understand the energy consumption side, to determine whether the use of electric motors and batteries brings any benefit.

Regarding the proposed VSC strategy in this study, another focus of interest is the analysis of the response of the powertrain, mainly the battery, brake system, differential and halfshafts, to blending axle motor braking/traction with individual friction braking. In order to capture this response and evaluate the performance of the proposed controller, an original dynamic vehicle simulator is developed in this dissertation with the objective of reducing controller calibration effort as well. The simulator is designed such that it can accurately represent the vehicle behavior without imposing excessive complexity. Therefore, in addition to the previously discussed objective, this research also introduces the development of an HEV model that predicts the dynamic behavior of the vehicle.

1.2. Contribution of the Dissertation

The primary objective of this research is the conception, development and evaluation of a differential braking/driving VSC strategy for a hybrid-electric SUV equipped with axle motors. In accordance with this objective, the first contribution of this research is the formulation of a powertrain and vehicle dynamics model that captures the dynamic behavior of the hybrid powertrain and of the vehicle to permit a realistic evaluation of vehicle stability.

A second contribution is made in the area of VSC design for a hybrid electric vehicle. The VSC scheme proposed in this dissertation represents a first in the open literature in two aspects.

1) The proposed solution introduces a systematic VSC strategy based on distributing the corrective longitudinal force/yaw moment control action to individual wheel slip ratios by blending regenerative axle motor braking/traction with individual wheel braking in order to track the desired yaw rate and vehicle speed without causing excessive vehicle sideslip angles. In particular, "blending regenerative axle motor braking/traction with individual wheel braking" is emphasized in this study, in contrast with other studies that focus on vehicle stability control based on hub motor architectures with the ability to control traction and braking independently at each wheel. Today, production hybrid vehicle architectures do not include four wheel independent hub motors, and the common practice in production HEVs is to simply turn off motor braking/traction during an event of instability and avoid blending motor traction/braking with their already built-in (brake actuated) vehicle stability control programs.

2) The proposed control design focuses on a common problem of all brake actuated vehicle stability control strategies, which is the fact that in extreme steering maneuvers, brake actuated VSC strategies usually decelerate the vehicle in order to ensure its stability. The proposed strategy offers reference yaw tracking and vehicle stabilization without interfering in the driver's longitudinal speed demand. This is accomplished by utilizing the rapid realization of tractive torque that the electric motors provide. While this is a secondary benefit that would be most relevant to high performance or race vehicles, it does give a measure of the significant improvement brought by the proposed method.

1.3. Organization of the Dissertation

This dissertation is organized as follows: Chapter 2 provides an overview of the published research related to the problem of VSC for conventional vehicles, as well as some fundamental concepts in the research area of VSC. The literature survey conducted in the next chapter clarifies motivation for the proposed VSC strategy. Chapter 3 describes the vehicle platform for which the vehicle simulator and the proposed VSC are developed in the context of the HEV student competition EcoCAR. Furthermore the simulator developed to represent this SUV is explained in detail. Chapter 4 focuses on VSC design methodologies specifically for HEVs equipped with axle motors in order to emphasize potential benefits and importance of how to involve electric motors within a VSC scheme. Chapter 5 presents the proposed VSC strategy, and evaluation of this strategy with software-in-the loop (SIL) and model-in-the loop (MIL) simulations in real time for different extreme steering/braking maneuvers. In Chapter 6, some concluding remarks are made and future research directions are proposed.

2. Background

This chapter is composed of five sections. In Sections 2.1 and 2.2, basics concepts and objectives of VSC such as target yaw rate and the sideslip angle considerations are summarized. In Section 2.3 the differential-brake-based fuzzy control approach is investigated; this is one of the most common VSC approaches used in production vehicles. Section 2.4 describes results obtained using computer simulations that explore various emergency driving conditions. The results of Chapter 2 provide clear motivation for the developments that follow.

2.1. Concept of VSC

Human error is the cause for a large portion of road accidents. Due to extreme circumstances, such as an obstacle suddenly appearing on the road or driving at inappropriately high speeds, a vehicle can reach its critical limits and become uncontrollable. Because drivers only rarely experience this kind of critical situation, they usually fail to recognize how close a steering or a braking maneuver has brought them to the vehicle's physical limits. They do not grasp how much of the potential adhesion between the tires and the road surface has already been utilized, and fail to perceive that the vehicle may be at its maneuverability limit or about to skid off the road. Due to lack of experience in these borderline situations, the driver is frequently unable to regain active control of the vehicle, and often panics or overreacts. Evasive action is an example. After applying excessive steering input in the moment of initial panic, the driver then counter steers with even greater zeal in an attempt to compensate for the initial error. Extended sequences of steering and counter steering with progressively greater input angles then lead to a loss of control of the vehicle.

A study of approximately 17000 car accidents in Germany has shown that 25% of these accidents were the results of spinning cars [5]. In approximately 60% of the accidents with spinning cars, only a single car was involved. This shows the requirement of an active yaw control system that would take the role of keeping the vehicle on track by leaving the driver fully or partially out of the loop. As a solution, VSC enhances driving safety by providing the following assets:

- Enhanced vehicle stability; the system keeps the vehicle on track and improves directional stability under all operating conditions, including emergency stops, standard braking maneuvers, coasting, acceleration and load shift.
- Increased vehicle stability at the limits of traction, such as during sharp steering maneuvers (panic response), to reduce the danger of skidding.

Numerous studies have confirmed that VSC systems are highly effective in helping the driver maintain control of the car, thereby saving lives and reducing the severity of crashes [6]. In the fall of 2004 in USA, the U.S. National Highway and Traffic Safety Administration (NHTSA) confirmed other studies, releasing results of a field study carried out in the USA. The NHTSA in United States concluded that VSC reduces crashes by 35%. Additionally, SUVs with stability control are involved in 67% fewer accidents than SUVs without the system. The United States Insurance Institute for Highway Safety (IIHS) issued its own study in June 2006 showing that up to 10,000 fatal crashes could be avoided annually if all vehicles were equipped with VSC [7]. The IIHS study concluded that VSC reduces the likelihood of all fatal crashes by 43%, fatal single-vehicle crashes by 56%, and fatal single-vehicle rollovers by 77-80%. As a result of this statistical data, NHTSA has regulated the introduction of VSC for vehicles manufactured for the USA market that are under 10,000 pounds (4536 kg), starting with 55% of 2009 models, 75% of 2010 models, 95% of 2011 models, and all 2012 models [8].

2.2. VSC Objective

There are various cases in which a vehicle may go unstable considering the yaw motion. One of them is the steady state cornering. Here, the vehicle may not track the desired trajectory by getting out of the track, displaying the so called understeering or oversteering behavior. Understeering occurs when the vehicle does not yaw enough to

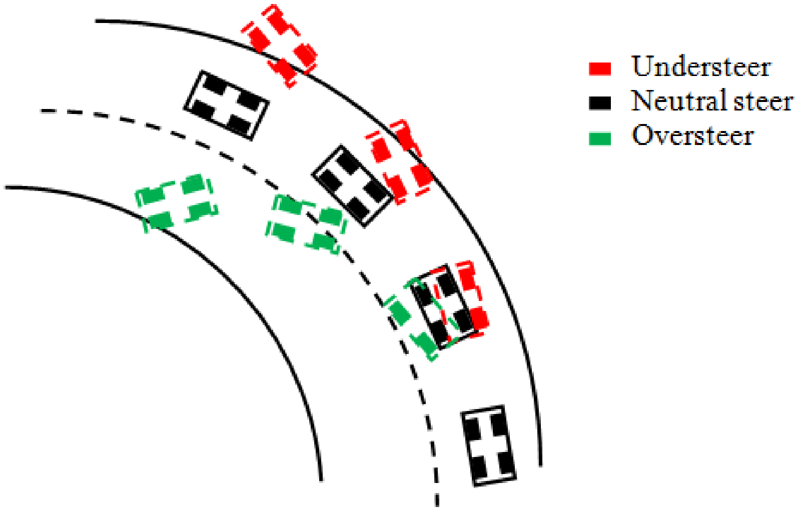

Figure 1 Vehicle behavior in steady-state cornering

follow the intended trajectory around a corner so that the vehicle turns along a larger diameter curve than intended. In the oversteering case the vehicle turns along a smaller diameter curve and eventually spins. Figure 1 illustrates these vehicle behaviors. As observed, the understeering vehicle tends to follow a straighter path and leaves the track. On the other hand, during oversteering, the vehicle tends to turn excessively and the driver loses longitudinal control.

Another important case for yaw control systems is the lane changing maneuver (Figure 2). This maneuver generally follows the appearance of a sudden obstacle on the road (such as a wild animals, a dropped box from another vehicle etc.) when the driver is too late to avoid it. In such a case, changing the lane without colliding with the obstacle is possible through a combination of braking and evasive steering. Without active yaw control, the initial steering input may cause the yaw rate and the sideslip angle increase to

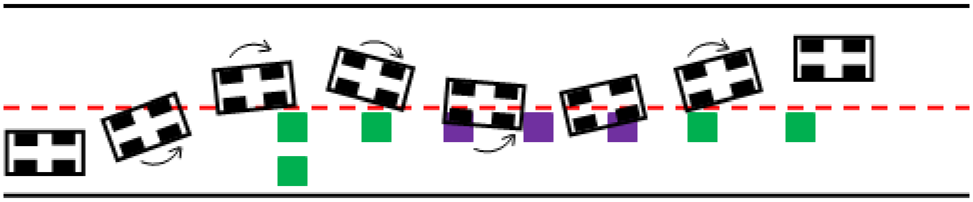

(a) An instability example for lane change maneuver without VSC

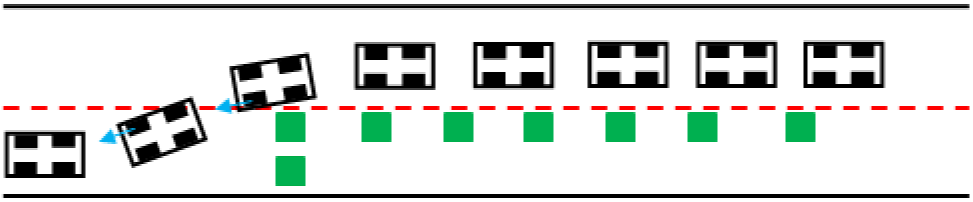

(b) Stabilized vehicle for lane change maneuver with VSC

Figure 2 Vehicle Behavior in Lane Change maneuver the point where driver intervention, in the form of countersteer, becomes imperative (Figure 2a). This countersteering then generates an excessive sideslip angle in the opposite direction, negating the driver's aim to avoid the foreign object, and the collision eventually occurs despite the driver's countersteering for the second time. With active yaw control, however, the vehicle can be steered accordingly so that the oscillation is 'damped' by applying pro- and contra yaw moments to the vehicle, by differentially applying brakes. This results in a more stable and more responsive vehicle capable of avoiding the collision, as shown in Figure 2b.

In the context of this introduction, the main aim of the VSC is to interpret and track the driver's intention provided it is within stability limits. A generic VSC scheme is shown in Figure 3.

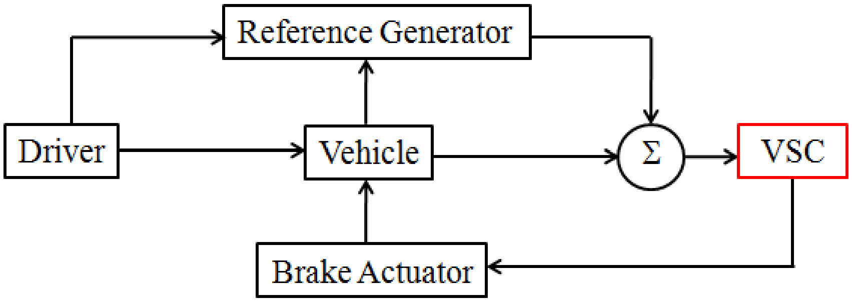

Figure 3 Overview of generic conventional VSC scheme

Here, the driver demand (throttle/brake and steer inputs) are fed both to the plant, namely the vehicle, and to the reference generator. The desired behavior is estimated by the reference generator and compared with the actual vehicle motion.

There exist several ways to interpret the driver's objective. These ways may vary from a single equation for the reference yaw rate derivation, which has an arbitrary constant for manipulating the reference vehicle behavior; to nonlinear equations, including all controlled/affected degrees of freedom [9-11]. The general idea here is that, there should be an assigned vehicle behavior tendency which may be referred as understeering/oversteering. This tendency should be presented by the reference equations, so that the drivers' manipulation is predicted as intended. For this purpose, building a simple vehicle model which is capable of presenting the main behavior of the vehicle deducted by the input signals coming from the driver is utilized. The input signals may include acceleration/brake demand and steering input.

For this purpose, a simplified vehicle model called the single-track model or the bicycle model is mostly used in the literature. This model is obtained by lumping two wheels on the same axle to a single virtual wheel, which is aligned to the centerline of the vehicle, as shown in Figure 4. It is generally capable of demonstrating essential handling behavior of a vehicle for low lateral acceleration range.

Equation 1 (derivation is provided in *Appendix A*) represent the linear state equations for yaw velocity r and vehicle sideslip angle β as the two states and the front wheel steering angle δ as the input of the bicycle model.

$$\begin{Bmatrix} \dot{\beta} \\ \dot{r} \end{Bmatrix} = \begin{bmatrix} \dfrac{2(C_f + C_r)}{MV_x} & -1 + \dfrac{2(aC_f - bC_r)}{MV_x^2} \\ \dfrac{2(aC_f - bC_r)}{I_z} & \dfrac{2(a^2C_f + b^2C_r)}{I_zV_x} \end{bmatrix} \begin{Bmatrix} \beta \\ r \end{Bmatrix} + \begin{bmatrix} \dfrac{-2C_f}{MV_x} \\ \dfrac{-2aC_f}{I_z} \end{bmatrix} \delta \qquad (1)$$

where, V_x is the longitudinal speed of the vehicle, M is the total mass of the vehicle, I_z is the yaw moment of inertia, C_f and C_r are front and rear tire cornering stiffness values, a

and b are distances form front and rear axles to the center of mass, respectively, as illustrated in Figure 4.

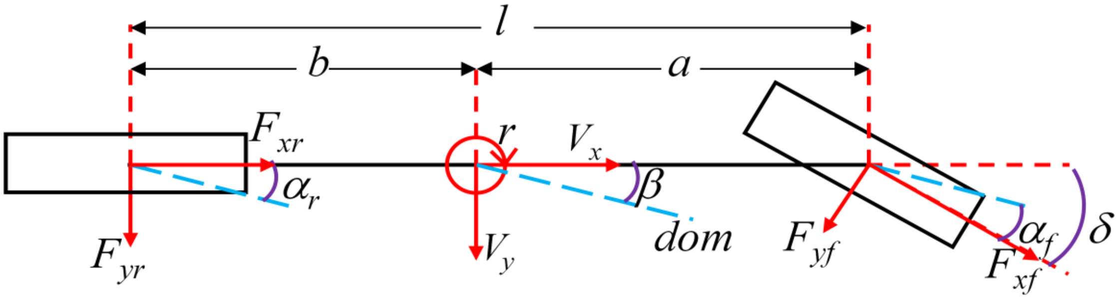

Figure 4 Single-track (bicycle) Vehicle Model

From this equation, the transfer function between the yaw velocity and steering input can be derived as:

$$r(s)=\frac{\dfrac{-aV_x^2M}{2lC_r}s+V_x}{\dfrac{MI_zV_x^2}{4lC_fC_r}s^2-\dfrac{\left(C_f+C_r\right)I_zV_x+MV_x\left(a^2C_f+b^2C_r\right)}{2lC_fC_r}s+\dfrac{MV_x^2}{2lC_fC_r}\left(aC_f-bC_r\right)+l}\delta(s)\quad(2)$$

The condition of stability, i.e. the condition of having negative eigenvalues, depends on the third term of the characteristic polynomial since the first two terms are positive:

$$\frac{MV_x^2}{2lC_fC_r}\left(aC_f-bC_r\right)+l>0 \qquad (3)$$

and if:

1) $aC_f>bC_r$ or $|aC_f|<|bC_r|$ then the vehicle is said to be understeer, and it is unconditionally stable.

2) $aC_f = bC_r$ then the vehicle is said to be neutral steer, and it is again unconditionally stable.

3) $aC_f < bC_r$ or $|aC_f|>|bC_r|$ then the vehicle is said to be oversteer, and it is unstable above a certain critical speed.

Since the goal of VSC is to stabilize the vehicle, the condition $|aC_f|\leq|bC_r|$ results in the desired yaw rate:

$$r_d(s)=\frac{\dfrac{-aV_x^2M}{2lC_r}s+V_x}{\dfrac{MI_zV_x^2}{4lC_fC_r}s^2-\dfrac{\left(C_f+C_r\right)I_zV_x+MV_x\left(a^2C_f+b^2C_r\right)}{2lC_fC_r}s+k_{us}V_x^2+l}\delta(s) \tag{4}$$

where k_{us} is called the understeer coefficient, and is usually selected to be $0<k_{us}<<1$ to have a control that will yield a slightly understeer stable vehicle.

On the other hand, the steady state lateral acceleration of the vehicle can be written as:

$$a_{yss}=\frac{V_x^2}{R}=\frac{V_x}{R}V_x=rV_x \tag{5}$$

where R is the radius of curvature of the trajectory. Since the maximum lateral force can not exceed the total force, i.e. $M|a_y| \leq Mg\mu$, where a_y is the lateral acceleration and μ is the coefficient of friction, then $|a_y|\leq g\mu$ and by substituting Equation 5, $|r|\leq g\mu/V_x$. Therefore the desired yaw rate given by Equation 4 is saturated by $g\mu/V_x$.

However, tracking this desired yaw rate should not be realized at all costs since the second objective of VSC is to limit the vehicle sideslip angle in order to prevent vehicle spin. Vehicle sideslip angle is another measure of vehicle stability. During normal driving average drivers will not exceed sideslip angles of ±2° [12]. The average driver usually loses control of the vehicle for high values of sideslip angle. It is explained in [13] why the handling of cars at high sideslip angles is so difficult. If the steering wheel is turned, then a yaw moment on the car is generated by the lateral forces on the tires. The yaw moment leads to a change in the yaw velocity of the car. However, the yaw moment also depends on the sideslip angle of the car. With increasing sideslip angles, the yaw moment gain decreases, as illustrated in Figure 5. At large sideslip angles the yaw moment can hardly be influenced by changing the steering angle. Typically, at the physical limit the steerability of the car is almost lost. In general, on dry asphalt roads the physical limit is reached at a sideslip angle of approximately ±12°, while on ice this value is approximately ±2° [12].

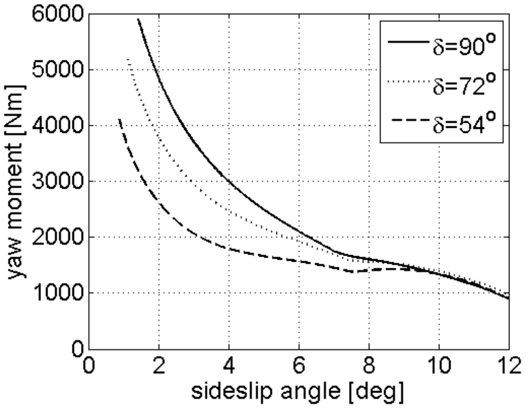

Figure 5 Yaw moment vs sideslip angle for different steering angles (steering ratio is 1:18)

The phase plane method is used in some studies [14-17] to evaluate vehicle stability. If the steering angle is zero, the origin of the phase plane constitutes a stable convergence point. Within a certain area around the origin, i.e. the stability area phase plane points converge to the origin, as shown in Figure 6a by the shaded region. Outside the stability area phase plane points diverge from the origin and the vehicle behavior is unstable.

During cornering, when the steering angle is not zero, the sideslip angle stability margin becomes asymmetric and reduced in the direction of steering as shown in Figure 6b. For the driver it becomes more difficult to keep the car under control. For large steering angles, the stability margin usually disappears, there is no stable combination of and there is no stable solution of the vehicle motion as seen in Figure 6c. This situation then results in a spinning car.

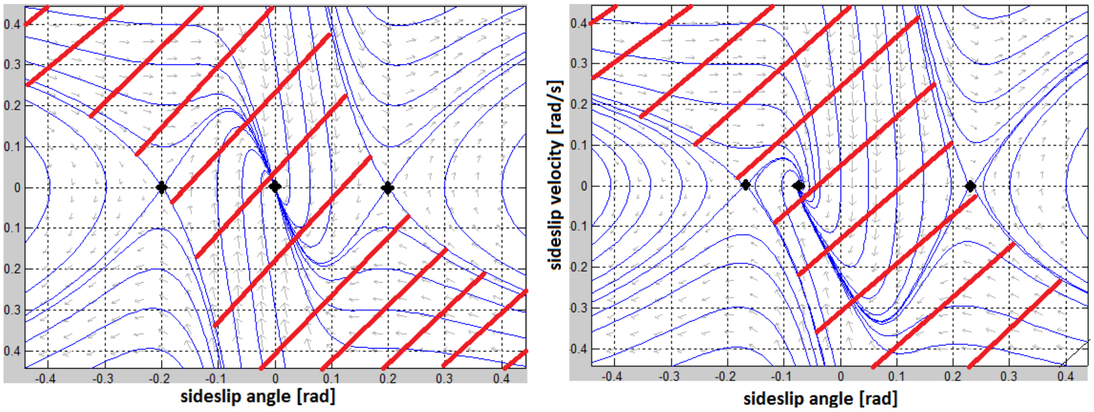

(a) δ=0 *(b) δ=45^o*

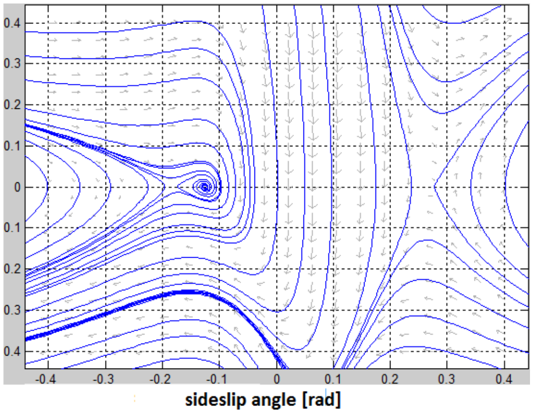

(c) δ=90^o

Figure 6 Sideslip angle velocity vs sideslip angle assuming a constant velocity 90 kph on asphalt road surface, for different steering inputs (steering ratio is 1:18).

In light of the explanation above, the "optimal" sideslip angle is a subjective issue. From a pure theoretical stability standpoint, considering the planar equations of motion, it has been shown [16, 17] that even at very high sideslip angles the vehicle system can be stabilized theoretically by applying extremely large counter steering angles. However, from a practical standpoint, excessive sideslip angle means a great loss in steerability of the vehicle, i.e. the controllability of the vehicle for an average driver. In fact the ideal case for an average driver is zero sideslip angle. In the VSC literature, there are basically two different desired sideslip angle values set as a VSC control objective. The first one is having the ideal case, namely zero sideslip, as the control objective [10, 18, 19]. The second approach [20-23] is a desired sideslip angle given by the following expression:

$$\beta_d(s) = \frac{\dfrac{-I_z V_x}{2lC_r}s + \dfrac{aMV_x^2}{2lC_r} + b}{\dfrac{MI_z V_x^2}{4lC_f C_r}s^2 - \dfrac{\left(C_f + C_r\right)I_z V_x + MV_x\left(a^2 C_f + b^2 C_r\right)}{2lC_f C_r}s + k_{us}V_x^2}\delta(s) \qquad (6)$$

This expression is derived from the bicycle model (Equation set 1), just like the desired yaw rate expression of Equation 4.

However, the referenced work that propose setting a desired vehicle sideslip angle consider not only differential braking, but also active steering, that is, having the benefit of an additional degree of actuation freedom for achieving a certain desired sideslip angle. If one only considers differential braking/driving, such as in this dissertation study, there is another widely used conservative approach in literature [24, 25], namely the condition in [26], which sets a practical limit to the target sideslip:

$$\beta_{\max} = \mu\left(10^\circ - 7^\circ\left(\frac{V}{40m/s}\right)^2\right) \tag{7}$$

This limit comes directly from road tests performed for various vehicles, and is the criterion for sideslip angle used in this dissertation when evaluating different VSC approaches.

2.3. Fuzzy Control approach to VSC

Fuzzy control is one of the most common methods for implementing VSC strategies [18, 20, 21, 24, 27-30]. The advantage of this approach lies in the benefit of not requiring an explicit mathematical model of the vehicle, while still being robust [31]. Furthermore, the rule based linguistic terms of fuzzy control are well matched to a subjective interpretation of vehicle handling. Given the limited number of feedback signals that can be used in the control design, due to limited sensor availability in production vehicles, fuzzy control is used very commonly in industry [4, 28, 29].

Two brake-based fuzzy control approaches may be found in the VSC in literature. The first is the Fuzzy PI control scheme [27, 28, 30]. In this scheme, the controller uses the yaw rate and acceleration errors as control inputs, and computes the brake torque as the output for counter yaw moment action. A Fuzzy PI scheme is shown in Figure 7.

In this scheme, α, β and δ are the driver commands, namely accelerator pedal, brake pedal and steering wheel angle, respectively. The bicycle model generates the reference value for yaw rate and yaw acceleration, and comparing desired and measured values, the error is fed into the fuzzy controller.

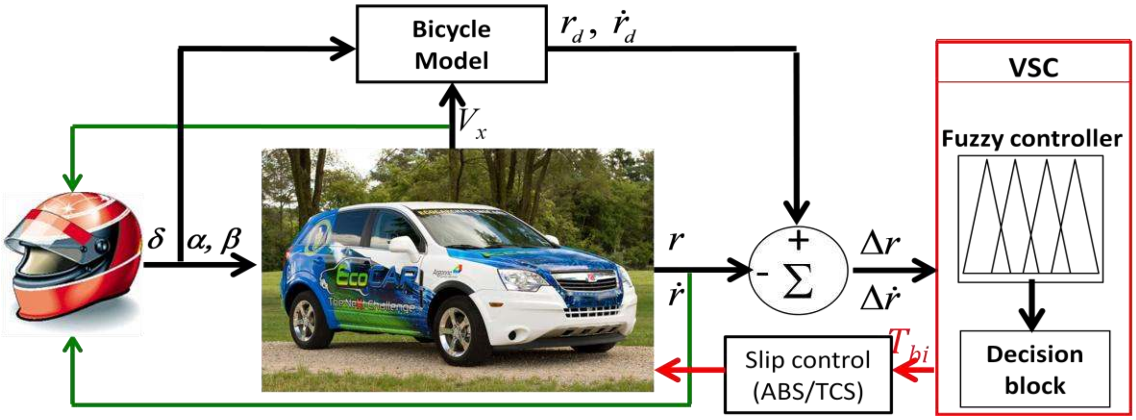

Figure 7 Overall structure of Fuzzy pi scheme

The design of the fuzzy controller is essentially based on a trial and error procedure. The rule base covers the whole input domain while the output signal is unique for every input pair. The fuzzy controller mainly consists of three subsystems, namely, fuzzification, rule base, and inference mechanism and defuzzification [31]. The main scheme is shown in Figure 8.

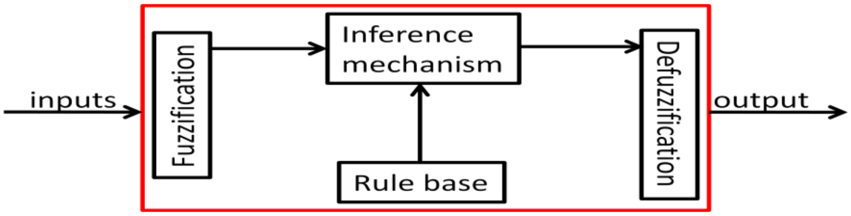

Figure 8 Basic scheme of the fuzzy controller

The fuzzification process is responsible for converting the control inputs into parameters which can be understood by the inference mechanism, whereas the inference mechanism is responsible for emulating the expert's decision making process, by using rule based “if-then” statements. The rule base is predefined for the plant in order to guide the controller as to the control action to be taken in specific conditions. After this information is evaluated by an inference mechanism (or inference engine), the defuzzification process is responsible for generating a quantitative output.

In this chapter, a typical fuzzy controller is simulated to illustrate its operation. The MATLAB Fuzzy Toolbox is used, and in particular the Mamdani inference method is used for implementing the inference mechanism, and the centroid algorithm [31] is used for the defuzzification process. Nine different levels are defined for both the yaw rate and the yaw acceleration error membership functions. Tuning the control rules is a cumbersome procedure. Here, as a basis in setting the rules, rules similar to the one in [27] are taken as a starting point. The 81 rules for the Fuzzy PI Controller and the control surface generated by these rules are shown in Figure 9.

Once the brake torque is computed, the final stage of the controller, namely the decision block selects the “appropriate” wheel(s) to brake, as shown in Figure 7. Selection of the appropriate wheels for braking has been a discussion topic in the literature, especially among studies that applies brake actuated control for VSC. There is not a clear consensus in the literature on this the selection of which wheels should be braked. From an intuitive standpoint it is obvious that inner wheels should be braked in taking a turn to prevent understeering, and that outer wheels should be braked to prevent oversteering of the vehicle, such as shown in Figure 10.

However, there are different approaches about front versus rear selection. For instance it is claimed in [18] that yaw moment control can be achieved by modifying the

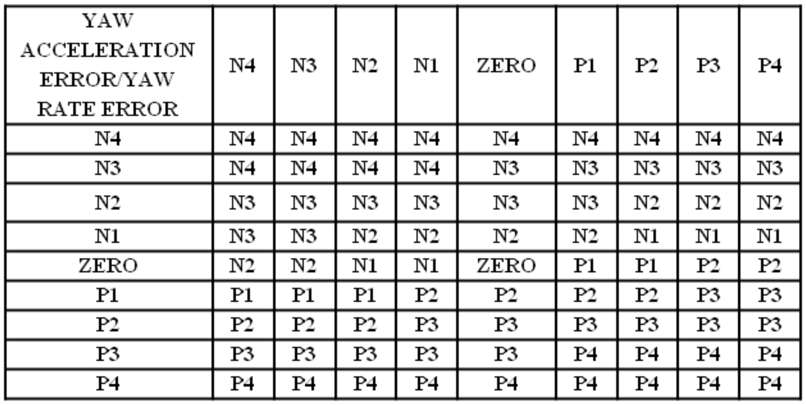

YAW ACCELERATION ERROR/YAW RATE ERROR	N4	N3	N2	N1	ZERO	P1	P2	P3	P4
N4	N4	N4	N4	N4	N4	N4	N4	N4	N4
N3	N4	N4	N4	N4	N3	N3	N3	N3	N3
N2	N3	N3	N3	N3	N3	N3	N2	N2	N2
N1	N3	N3	N2	N2	N2	N2	N1	N1	N1
ZERO	N2	N2	N1	N1	ZERO	P1	P1	P2	P2
P1	P1	P1	P1	P2	P2	P2	P2	P3	P3
P2	P2	P2	P2	P3	P3	P3	P3	P3	P3
P3	P3	P3	P3	P3	P3	P4	P4	P4	P4
P4	P4	P4	P4	P4	P4	P4	P4	P4	P4

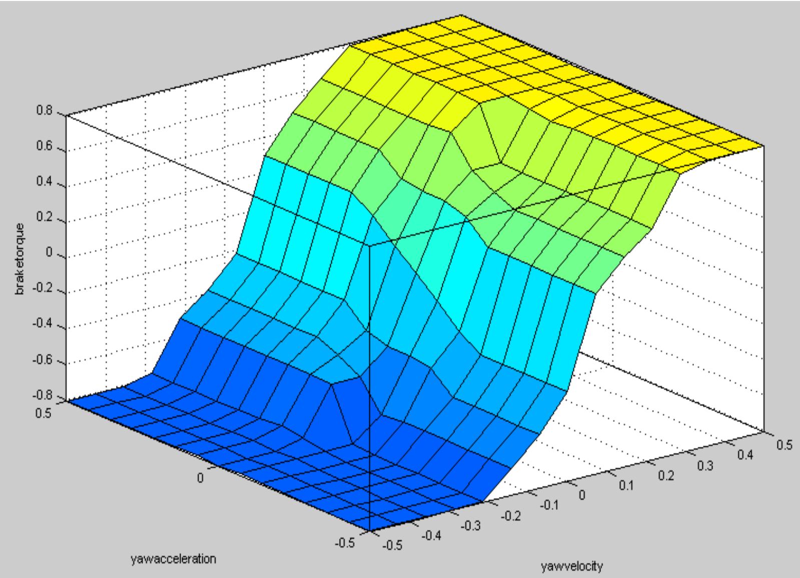

Figure 9 Fuzzy rules and the control surface generated for Fuzzy PI

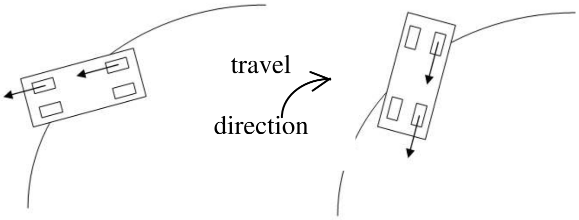

Figure 10 Oversteering (left) and understeering (right) vehicles in a turn, and the preventive braking action

brake forces applied only to the front wheels (inner front during understeering, and outer front during oversteering), which reduces the complexity of control. On the other hand, the relation of the braking force of each wheel with the counter/pro direct yaw moment it will induce on the vehicle is mentioned in [20], and it is concluded that the optimal selection is inner rear during understeering, and outer front during oversteering, on the basis of geometric relations. The best explanation can be found in [32] where the selection decision is supported with tire characteristics, as illustrated in Table 1.

Table 1 Corrective yaw moment table

Tire	**Inner front**	**Outer front**	**Inner rear**	**Outer rear**
Increase F_x	Pro-cornering	Contra-cornering	Pro-cornering	Contra-cornering
Decrease F_y	Contra-cornering	Contra-cornering	Pro-cornering	Pro-cornering

From Table 1, inner rear is concluded to be the most suitable wheel for generating a corrective yaw moment in the same direction, i.e. during understeering, and outer front to generate a corrective yaw moment in the opposite direction, i.e. during oversteering.

In addition to utilizing the same selection in references [28, 29], a fuzzy control is applied by the authors such that the inner front wheel assists the inner rear one during understeering whereas the outer rear wheel assists the outer front one during oversteering, to obtain better performance.

In this section of this dissertation, the most common approach, namely braking inner rear wheel during understeering, and outer front wheel during oversteering is utilized, for the fuzzy controllers, in order to compare their performance with the proposed VSC in Chapter 5. Note that this selection also fits the convention of Bosch ESP© [4, 15]. This heuristic explanation provided underscore the need for a more systematic approach. The essence of the problem is that the system is overactuated, and it may therefore be appropriate to develop optimization methods rather than a heuristic reasoning in order to split the corrective yaw moment action to individual wheels.

The second most common brake-actuated fuzzy controller considers the same scheme as the yaw controlled Fuzzy PI, with the only difference being the sideslip angle instead of the yaw acceleration error that is fed into the yaw controller [24, 27, 29]. This controller takes the sideslip angle into account too, in addition to the yaw rate, in order to limit it by the value given in Equation 7. The rules are tuned with a trial error process again, this time giving the priority to vehicle sideslip angle. The 81 rules for the Fuzzy Sideslip Corrected Controller and the control surface generated with these rules are shown in Figure 11.

2.4. Simulations of The Fuzzy Controllers

This section presents the results of simulations performed in MATLAB/Simulink environment in order to illustrate the behavior of the fuzzy controllers explained in the preceding section. The vehicle and powertrain is represented by the dynamic vehicle simulator built for the hybrid SUV that will be explained in detail in Chapter 3. The hybrid powertrain, i.e. the electric motors are ignored for the this case and the engine of the stock vehicle[1], the 3.6l V6 engine (FWD) is considered as the sole tractive power source as the goal is to represent the performance of the standard VSC system, which

---

[1] The vehicle platform that will be introduced in the next section as well, is a 2008 GM Saturn Vue.

YAW RATEERROR SIDESLIP ANGLE	N4	N3	N2	N1	ZERO	P1	P2	P3	P4
N4	N4	N4	N4	N3	N2	N3	N4	N4	N4
N3	N4	N4	N3	N3	N2	N3	N3	N4	N4
N2	N4	N3	N3	N3	N2	N3	N3	N3	N4
N1	N4	N3	N3	N2	N1	N2	N3	N3	N4
ZERO	N4	N4	N3	N1	ZERO	N1	N3	N4	N4
P1	N3	N3	N2	P1	P1	P1	N2	N3	N3
P2	N2	N1	ZERO	P1	P2	P1	ZERO	N1	N2
P3	P4	P3	P3	P2	P2	P2	P3	P3	P4
P4	P4	P4	P3	P3	P2	P3	P3	P4	P4

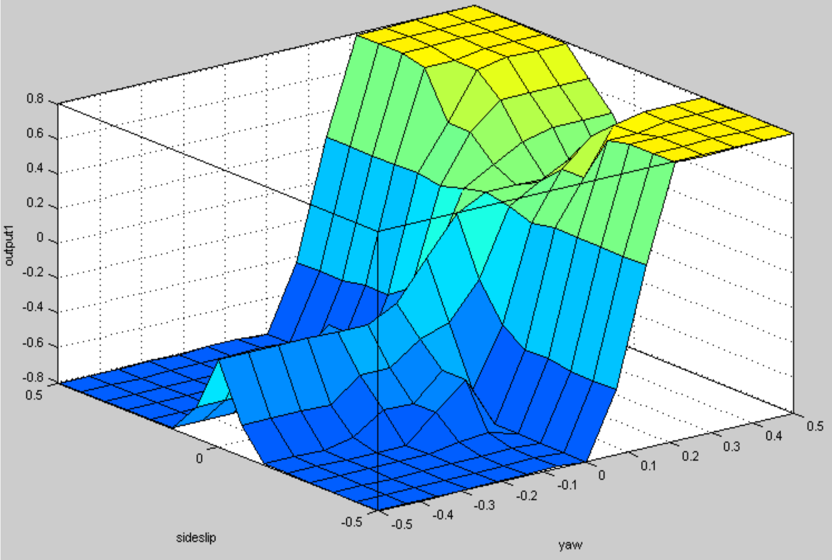

Figure 11 Fuzzy rules and the control surface generated for Fuzzy controller with sideslip angle limitation

makes use of a conventional powertrain, namely the brakes and engine intervention, in order to have a better understanding of this control approach, and try to outline its limitations.

The simulated steering maneuvers are standard maneuvers that represent emergency driving situations. The first is the lane change maneuver, which describes the vehicle handling performance in the case of a series rapid steering and counter steering actions while traveling at highway speeds, as depicted in Figure 12a. This maneuver could for example represent a sudden obstacle that has appeared on the road. The second maneuver is the J-turn maneuver, during which the driver simultaneously brakes and generates a step steering input as depicted in Figure 12b, to maintain a constant turning radius during a sharp turn. The vehicle without VSC is also simulated for these maneuvers in order to evaluate the effectiveness of the fuzzy controllers.

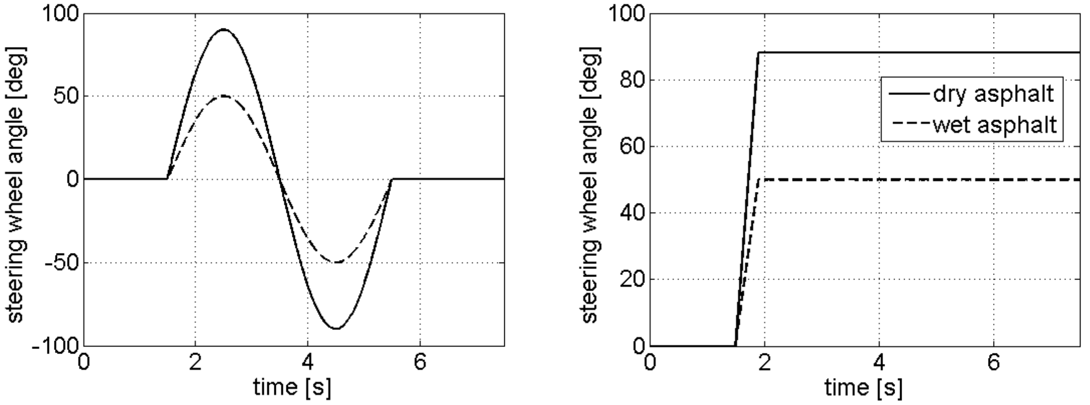

(a) Lane change (b) J-turn

Figure 12 Types of steering inputs

Lane change maneuver, V_{x0}=90kph, μ=1/0.5: Initial vehicle velocity is taken as 90 kph and two road conditions, dry (μ=1) and wet asphalt (μ=0.5) road are considered. The maximum level of the steering (handwheel) angle input is taken as 90 degrees (the steering ratio is 1:18) for the dry asphalt, and 50 degrees for the wet asphalt, respectively, as shown in Figure 12a. Figure 13 shows the longitudinal speed, sideslip angle, yaw velocity, and the desired vehicle trajectory at the top, for the fuzzy PI controlled (Fuzzy1), and sideslip corrected schemes (Fuzzy2) together with the desired values for speed and yaw rate. For the sideslip angle, the limit that is specified by Equation 7 is imposed on the plot. At the bottom, the brake and engine torque profiles for the vehicles controlled with the two fuzzy controllers during the maneuver are shown. Tables showing maximum and root mean square (RMS) of the deviation of yaw rate and speed from the desired values, maximum sideslip angle and deviation from the allowed sideslip angle limit (in case the limit is exceeded) and the energy consumption while VSC is active are also given for each maneuver in order to compare the two fuzzy controllers. The energy consumed is calculated as $E_{net}=E_{traction}+E_{brake}$ where:

$$E_{traction} = \int_{\substack{VSC \\ on}} \frac{\omega_{ice} T_{ice}}{\eta_{ice}(\omega_{ice}, T_{ice})} dt \tag{8}$$

$$E_{brake} = \sum_{i=1}^{4} \int_{\substack{VSC \\ on}} \omega_i T_{EHBi} dt \tag{9}$$

where ω_{ice}, T_{ice} and η_{ice} are engine speed, torque and efficiency as a function of speed and torque, respectively. ω_i and T_{EHBi} are the ith wheel speed and brake torque, respectively.

It is observed from Figure 13 that control of the vehicle without VSC is likely lost on both road surfaces since the sideslip angle exceeds the limit given by Equation 7, which also results in a significant deviation from the desired trajectory.

On the other hand, Fuzzy1 tracks the desired yaw rate better than Fuzzy2 does, at the expense of having a higher sideslip angle than the one of Fuzzy2 for both maneuvers. For the maneuver on dry asphalt, this is acceptable as the sideslip angle is below the threshold, as seen in Figure 13a middle left figure. As a result the vehicle controlled with Fuzzy1 tracks the desired trajectory better for this maneuver in comparison to the vehicle

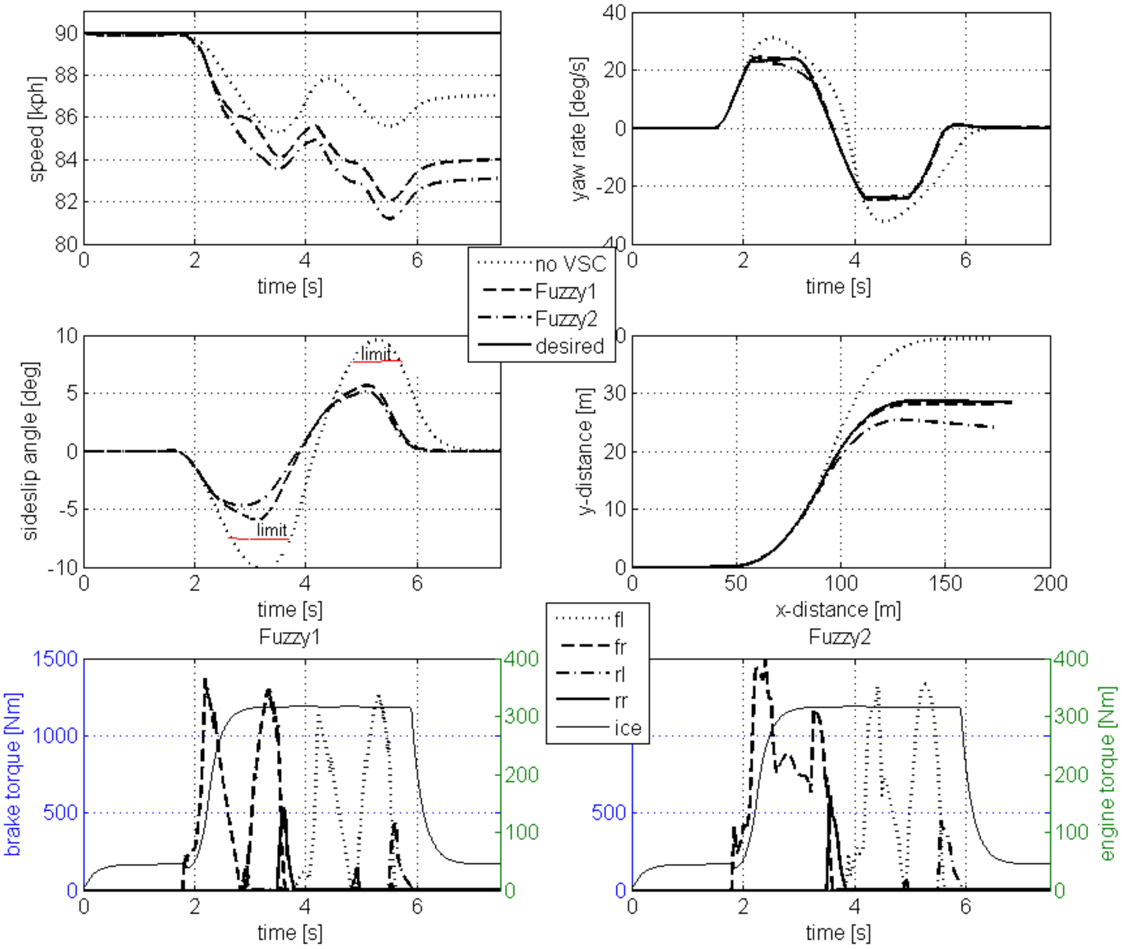

Lane change dry asphalt	$(V_{x\_error})_{max}$ *[kph]*	$(V_{x\_error})_{rms}$ *[kph]*	$(r_{error})_{max}$ *[deg/s]*	$(r_{error})_{rms}$ *[deg/s]*	β_{max} *[deg]*	$(\beta_{deviation})_{max}$ *[deg]*	Consumed energy *[kJ]* *(Tractive+Brake=Total)*
Fuzzy1	7.92	5.14	1.30	0.71	5.91	-	724.8+165.4=890.2
Fuzzy2	8.81	6.01	4.25	1.28	5.14	-	724.8+197.4=922.2

(a) Dry asphalt

continued

Figure 13 Lane change maneuver simulation results, sideslip angle, yaw rate, and longitudinal speed responses and vehicle trajectory at the top, brake/engine torque profiles for the two fuzzy schemes at the bottom

Figure 13 continued

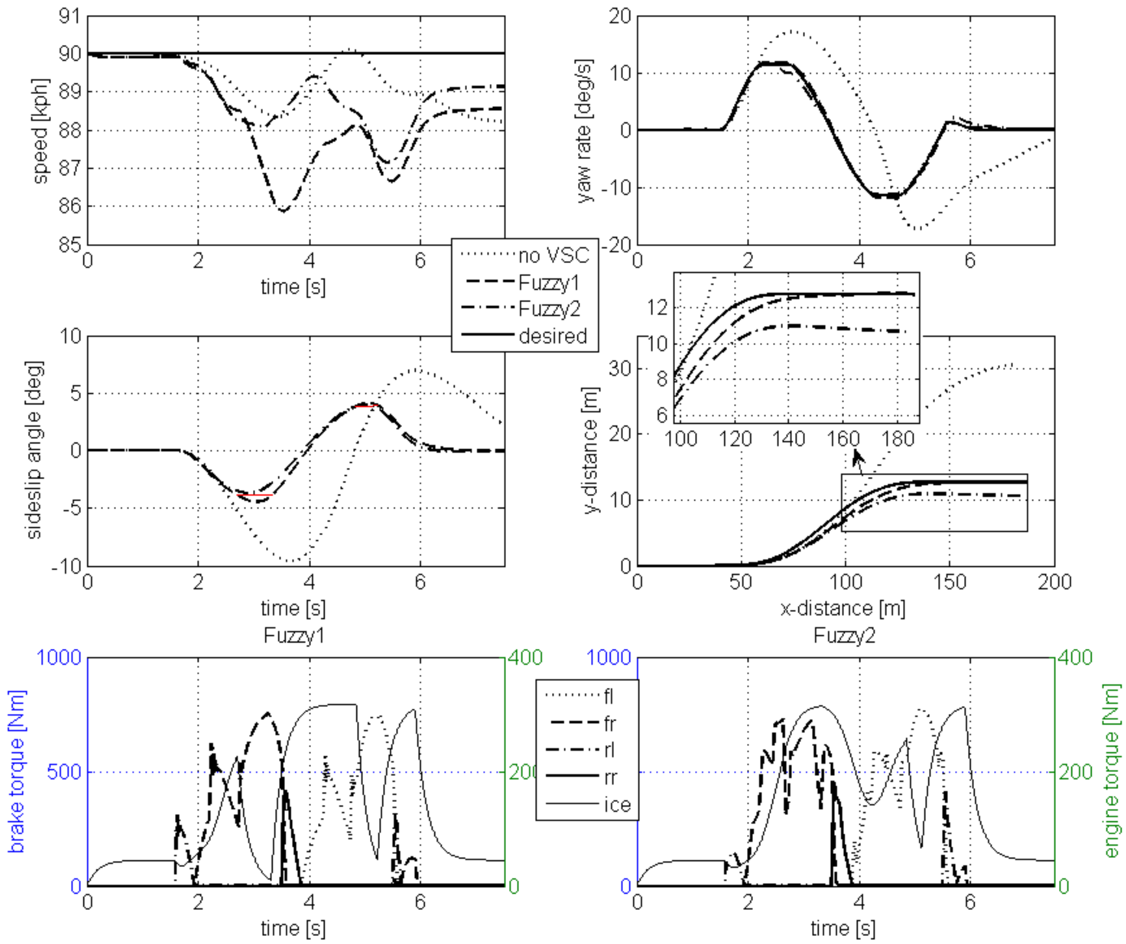

Lane change wet asphalt	$(V_{x\_error})_{max}$ *[kph]*	$(V_{x\_error})_{rms}$ *[kph]*	$(r_{error})_{max}$ *[deg/s]*	$(r_{error})_{rms}$ *[deg/s]*	β_{max} *[deg]*	$(\beta_{deviation})_{max}$ *[deg]*	Consumed energy *[kJ]* *(Tractive+Brake=Total)*
Fuzzy1	4.13	2.48	0.65	0.39	4.44	0.56	458.2+122.0=580.2
Fuzzy2	2.86	1.61	1.51	0.63	3.99	-	570.6+135.7=706.2

(b) Wet asphalt

controlled with Fuzzy2. The driver of the vehicle equipped with Fuzzy2 would have to steer further in order to maintain the desired trajectory.

However, the cost of having a higher sideslip angle for improved tracking of the desired yaw rate results in exceeding the maximum sideslip angle threshold (slightly by 0.56 degrees as tabulated) for the wet asphalt maneuver for Fuzzy1. These results show that Fuzzy1 vehicle tracks the desired yaw rate better at the expense of having a higher sideslip angle in comparison to the vehicle controlled with the Fuzzy2 scheme, whereas Fuzzy2 achieves a lower sideslip angle at the expense of worse desired yaw tracking, as seen in simulation results for both maneuvers.

Another important observation is that in the lane change maneuver, the differential braking action (mostly braking the front wheels to prevent oversteering) as observed from the brake torque profiles in order to track the desired yaw rate causes a decrease in vehicle speed for both Fuzzy schemes, especially for the dry asphalt case. The driver desires to go back to the initial speed at the beginning of the maneuver and floors the accelerator pedal, as it is observed that the engine torque is at its maximum. VSC tracks this torque request as long as the sideslip angle is below the threshold, as seen in the dry asphalt case. For the wet asphalt case, VSC cuts the engine torque between 3.5 and 5th seconds because the maximum sideslip angle threshold is exceeded momentarily for Fuzzy1. This observation matches some of the previous comments in the literature: Brake based systems interfere with the driver's longitudinal speed demand causing deceleration and therefore performance degradation [24, 29, 33]. In fact, considering the longitudinal speed's direct effect on vehicle sideslip angle (Equation A10), it is possible that a decrease in vehicle speed may not only cause performance degradation with respect to longitudinal speed, but also vehicle stability. The ability of an electric motor to deliver or absorb torque very rapidly may provide an opportunity to improve on the dynamic response of a VSC system.

For completeness, the table also provides a comparison of energy consumption during the maneuvers just described. Tractive energy consumption due to the engine is significantly higher in comparison to brake energy consumption for both schemes due to the engine's low energy efficiency of around 27% on average. On the other hand, Fuzzy2 scheme applies the brakes more to achieve its objective that causes slightly higher braking energy consumption than the one of Fuzzy1.

J-turn Maneuver, V_{x0}=90kph, μ=1/0.5: The initial vehicle velocity is 90 kph and two road conditions, dry (μ=1) and wet asphalt (μ=0.5), are considered. The maximum level of the steering (handwheel) angle input is taken as 90 degrees (the steering ratio is 1:18) for the dry asphalt, and 50 degrees for the wet asphalt, respectively, as shown in Figure 12b. Figure 14 shows the longitudinal speed, sideslip angle, yaw velocity, and the vehicle trajectory at the top, for the fuzzy PI controlled (Fuzzy1), and sideslip corrected schemes (Fuzzy2) together with the desired values for speed and yaw rate. For the sideslip angle, the limit that is specified by Equation 7 is imposed on the plot. The bottom part of the figure shows the brake and engine torque profiles for the vehicles controlled with the two fuzzy controllers during the maneuver. Tables showing RMS of the deviation of yaw rate and speed from the desired values, maximum sideslip angle and deviation from the allowed sideslip angle limit, and the energy consumption while VSC is active are also given for each maneuver in order to compare the two fuzzy controllers.

It is again observed that the controllability, i.e. steerability of the vehicle, without VSC is lost for both maneuvers. It is also observed again that vehicle controlled by Fuzzy1 tracks the desired yaw rate better than the one controlled with Fuzzy2, with RMS of the yaw rate error being 0.63 and 0.50 degree/s for dry and wet asphalts respectively, at the expense of having a higher sideslip angle in comparison to the vehicle controlled with Fuzzy2. Again this cost of increase in sideslip angle is acceptable for the dry asphalt result as the sideslip angle keeps barely lower than the threshold value. However, for the wet asphalt case, the vehicle controlled by Fuzzy1 exceeds the sideslip angle threshold by around 4 degrees, which would result in loss of control for an average driver. On the other hand, although the vehicle controlled with Fuzzy 2 does not track the desired yaw rate as good as Fuzzy1, it achieves a sideslip angle within limits of controllability for both road surfaces. Actually this behavior, observed also for the lane-change maneuver, points to an important tradeoff between yaw rate and sideslip angle responses, as also noted by authors [4, 15, 27-29]. That is to say, perfect tracking of the desired yaw rate usually brings with it the cost of excessive sideslip angle whereas reducing sideslip angle this time brings with it the cost of limiting yaw rate causing insufficient desired yaw tracking.

On the other hand, the energy consumed for this maneuver show that this time the brake energy is comparable to the energy consumed by the engine since the driver not only steers but also brakes. The corrective differential braking is added to the top of the

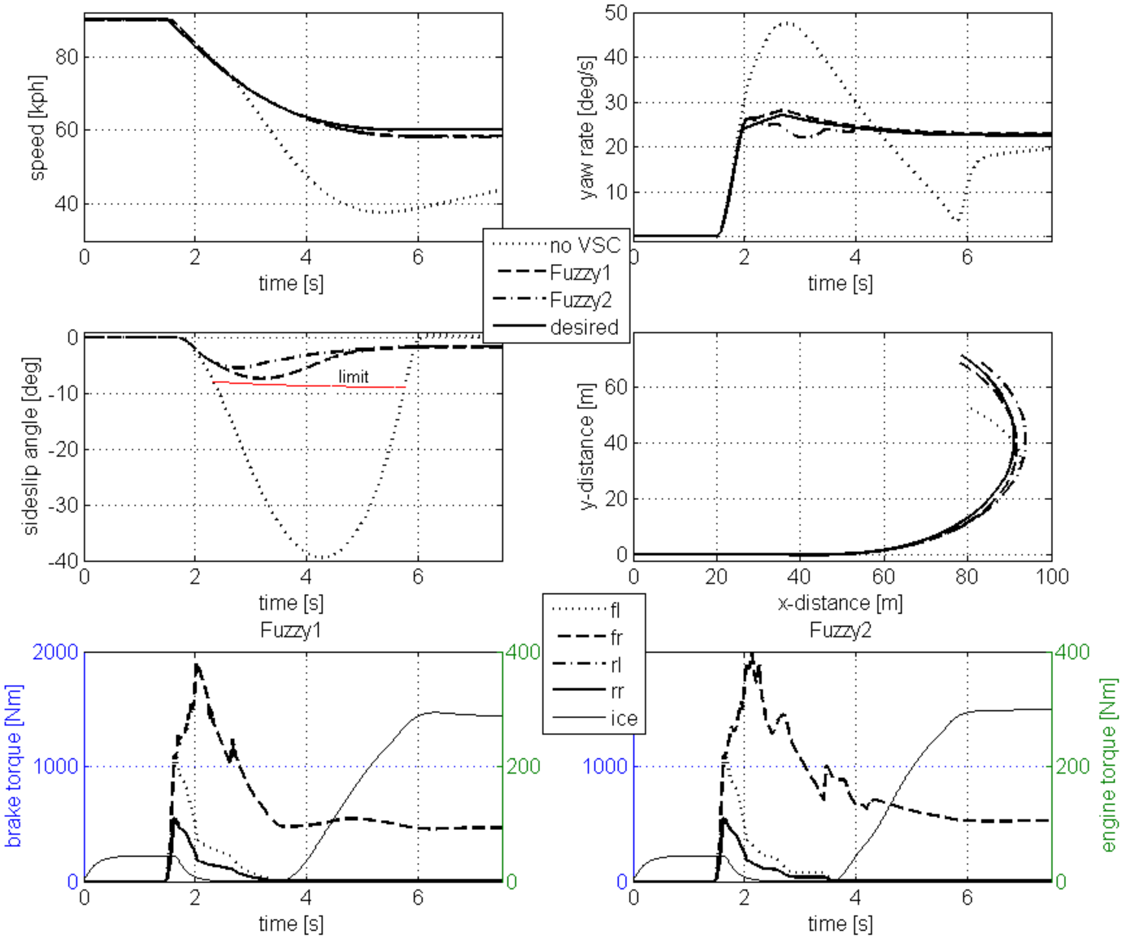

J-turn dry asphalt	$(V_{x\_error})_{max}$ *[kph]*	$(V_{x\_error})_{rms}$ *[kph]*	$(r_{error})_{max}$ *[deg/s]*	$(r_{error})_{rms}$ *[deg/s]*	β_{max} *[deg]*	$(\beta_{deviation})_{max}$ *[deg]*	Consumed energy *[kJ]* *(Tractive+Brake=Total)*
Fuzzy1	1.76	1.19	1.78	0.63	7.39	-	353.6+294.5=648.0
Fuzzy2	1.97	1.30	4.03	1.36	5.50	-	366.0+335.2=701.1

(a) Dry asphalt

continued

Figure 14 J-turn maneuver simulation results, sideslip angle, yaw rate, and longitudinal speed responses and vehicle trajectory at the top, brake/engine torque profiles for the two fuzzy schemes at the bottom

Figure 14 continued

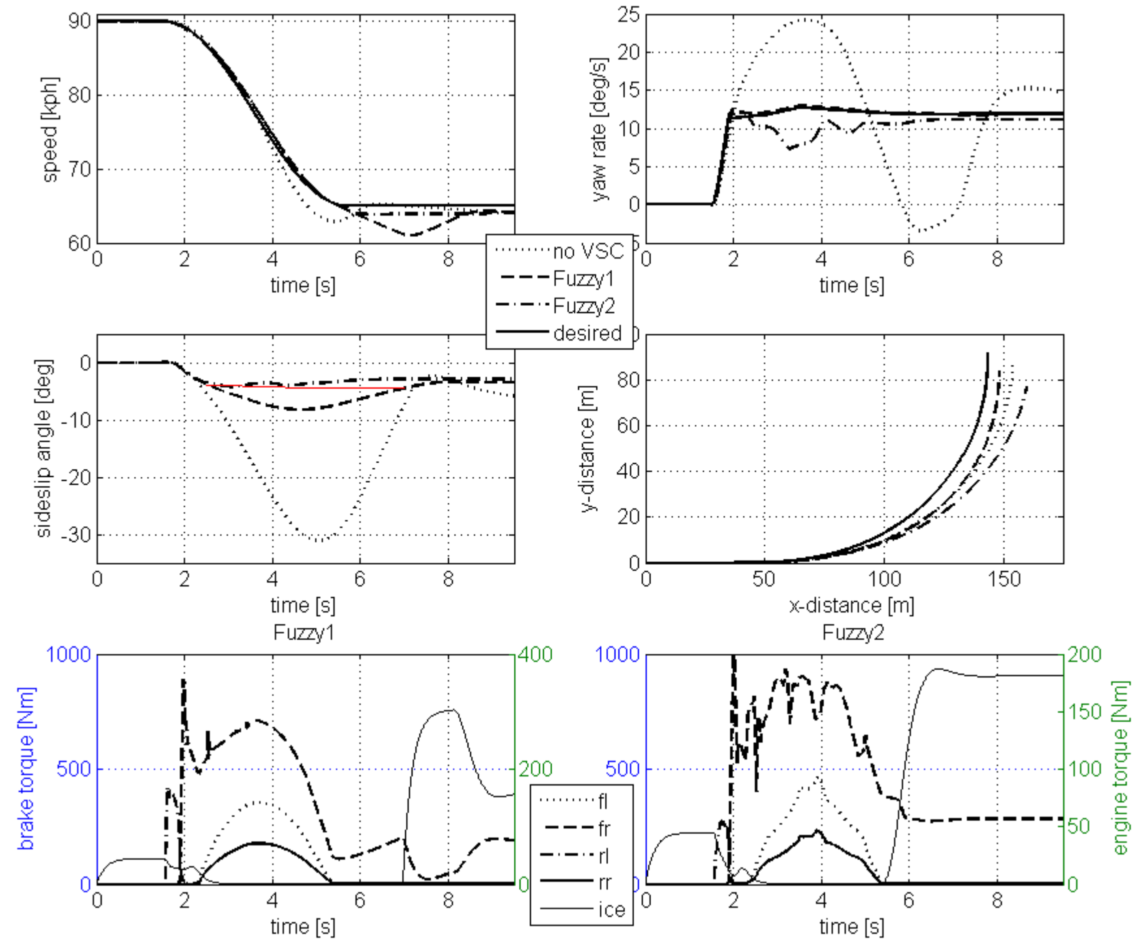

J-turn wet asphalt	$(V_{x\_error})_{max}$ *[kph]*	$(V_{x\_error})_{rms}$ *[kph]*	$(r_{error})_{max}$ *[deg/s]*	$(r_{error})_{rms}$ *[deg/s]*	β_{max} *[deg]*	$(\beta_{deviation})_{max}$ *[deg]*	Consumed energy *[kJ]* *(Tractive+Brake=Total)*
Fuzzy1	4.02	0.27	1.07	0.50	8.21	3.82	286.1+248.0=534.1
Fuzzy2	1.15	0.83	5.20	1.94	4.23	-	325.3+320.7=646.0

(b) Wet asphalt

braking to slow down the vehicle, as is evident from the brake torque profiles. Again, in an EV or HEV it may be possible to recover some of this energy.

2.5. Summary of this Chapter

This chapter has explored fuzzy differential braking control strategies using computer simulations. The results reveal the following research needs that have lead to the results presented in the remainder of this dissertation:

1) Tracking the desired yaw rate under all circumstances may cause excessive sideslip angles, especially close to vehicle's physical limits. These limitations are reached more easily on slippery surfaces such as wet asphalt. Therefore tracking the desired yaw rate should not be the aim of VSC in all road conditions and maneuvers.

2) Brake-based systems offer a good solution for safety and stability, i.e. yaw rate or sideslip, but interfere in the driver's longitudinal speed demand, which is related not only to performance, but may also affect stability. This limitation may be overcome with the utilization of electric motors within the VSC strategy as electric motors are capable of rapid braking/tractive torque actuation.

3) Due to the capability of (H)EVs to use regenerative braking in comparison to a conventional vehicle, the energy consumption during VSC activation is presumed to be lower for a VSC scheme making use of the electric motors, than the one of a conventional vehicle.

In this context, a further objective of this research is development of a novel and systematic VSC methodology for allocating the corrective longitudinal force/yaw moment action to individual wheel slips by blending regenerative axle motor braking/traction with individual wheel braking. The methodology is demonstrated using a hybrid-electric SUV as a case study.

3. EcoCAR Vehicle Architecture and Simulation Tool EcoDYN

This chapter is composed of two sections. In the first section, a vehicle platform is described for which the vehicle simulator and the proposed VSC are developed in the context of the HEV student competition EcoCAR. In the second section, the simulator developed to represent this SUV is explained in detail.

3.1. EcoCAR Vehicle Architecture

Ohio State is one of sixteen North American universities participating in EcoCAR: The Next Challenge, a vehicle development competition headline sponsored by the United States Department of Energy (DOE) and General Motors (GM) [34]. This three-year long competition challenges student teams to re-engineer a GM Donated Vehicle crossover sport-utility vehicle for increased fuel economy and decreased emissions while maintaining vehicle performance and consumer acceptability. Each team’s task is to design and build a new powertrain for their vehicle, resulting in a fully-functioning prototype vehicle.

The EcoCAR Challenge team at The Ohio State University has designed an extended-range electric vehicle capable of 40 miles all-electric range via a 22 kWh lithium-ion battery pack, with range extension and limited parallel operation supplied by a 1.8 L dedicated E85 engine. The schematic and component locations of the vehicle architecture are shown in Figure 15.

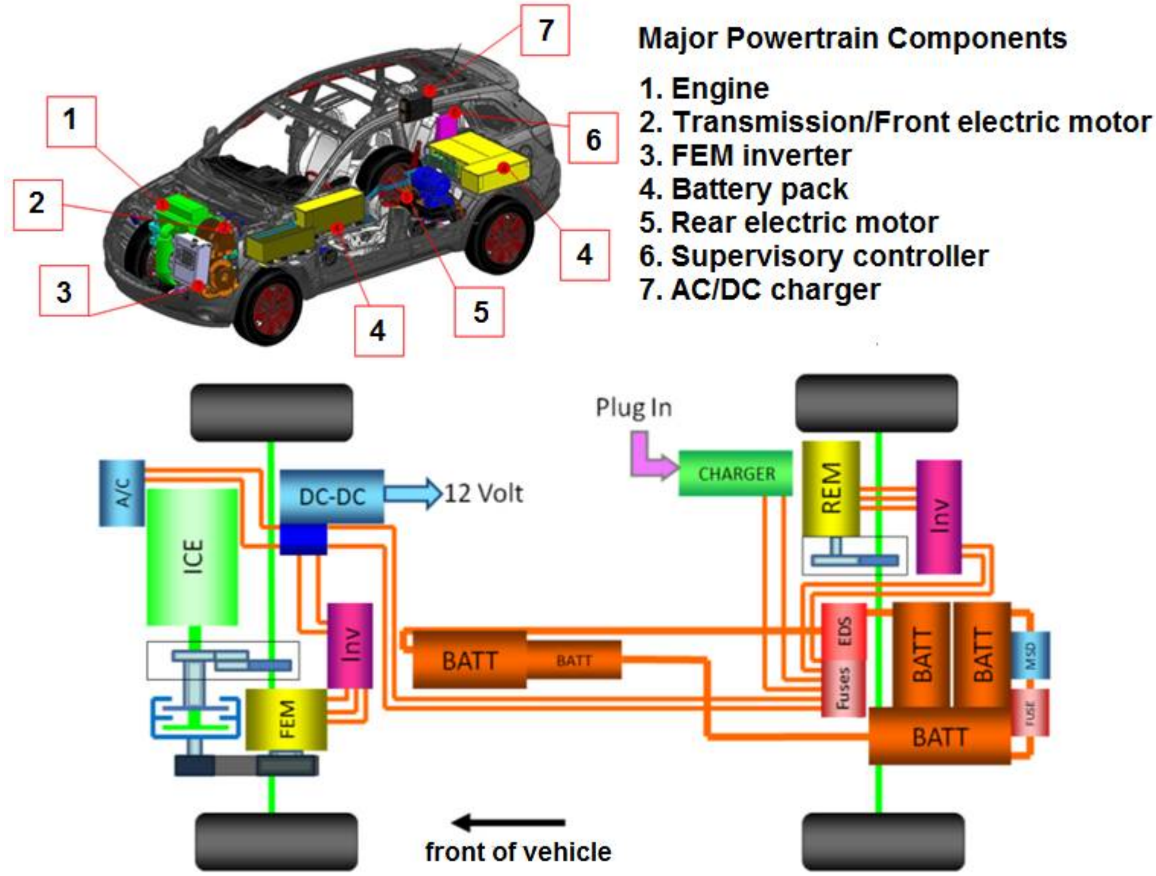

Figure 15 The OSU EcoCAR vehicle architecture with major components

The engine is coupled to an 82 kW front electric machine (FEM) via a twin-clutch transmission designed to enable greater operating efficiency through limited parallel operation. This transmission design allows the vehicle to operate in a series or parallel hybrid mode and allows front axle regenerative braking with the engine disengaged from the road. The exhaust aftertreatment system features a close-coupled three-way catalyst with an integrated electrically-heated catalyst for improved cold start and hot restart emissions. A 22 kWh lithium ion battery pack is used for onboard energy storage, packaged as a split pack with two modules in the front console area and three modules in the rear of the vehicle. A 103 kW rear electric motor (REM) provides pure electric vehicle capability, and allows rear axle regenerative braking. In addition, a DC/DC converter and an AC/DC charger are packaged in the rear, allowing the team to charge the vehicle in any location that has a 110V or 208V outlet.

A list of vehicle technical specifications is tabulated in Table 2. Further detailed information on design, energy management and drivability concerns of this vehicle can be found in [35, 36].

3.2. Simulation Tool: EcoDYN

EcoDYN vehicle simulator is a dynamic model of this experimental HEV built in Matlab/Simulink environment that is developed to represent vehicle and powertrain dynamic behavior and facilitate the evaluation of control strategies in terms of vehicle dynamics, drivability, fuel economy and performance. The overall structure of the simulator is shown in Figure 16. The main inputs and outputs of different components of the simulator are also imposed on the figure. Driver outputs are accelerator and brake pedal positions and steering wheel angle (α, β and δ). Supervisory controller commands include clutch state requests, torque command for electric motors and engine and brake torque for each wheel. Main outputs of the powertrain model are longitudinal and lateral forces that are fed into the vehicle dynamics model. Vehicle speed is sent to the driver model from the vehicle dynamics model and the loop is closed.

Table 2 Vehicle Technical Specifications

Specification	**Donated Vehicle Platform**	**EcoCAR Competition**	**Predicted OSU E-REV**	**Actual OSU E-REV**	**Validation Location**
ECOCAR COMPETITION REQUIREMENTS					
Acceleration 0-60 (s)	10.6 s	≤ 14 s	9.9 s	10 s	TRC
Acceleration 50-70 (s)	7.2 s	≤ 10 s	5.0 s	5.8 s	TRC
Towing Capacity (kg, (lb))	680 kg (1,500 lb)	≥ 680 kg @ 3.5%, 20 min @ 72 kph (45 mph)	1,130 kg @ 3.5%, 20 min @ 72 kph (45 mph)	≥ 680 kg @ 3.5%, 20 min @ 72 kph (45 mph)*	DPG-Y
Cargo Capacity (mm, (in))	0.83 m^3	Height: 457 mm (18”) Depth: 686 mm (27”) Width: 762 mm (30”)	Height: 730 mm (28.7”) Depth: 800 mm (31.5”) Width: 900 mm (35.4”)	Height: 730 mm (28.7”) Depth: 800 mm (31.5”) Width: 900 mm (35.4”)	DPG-Y
Passenger Capacity	5	≥ 4	5	5	DPG-Y
Braking 60-0 (m, (ft))	38-43m (123-140 ft)	< 51.8 m (170 ft)	42 m (138 ft)	37 m (121.5 ft)	TRC
Mass (kg, (lb))	1,758 kg (3,875 lb)	≤ 2,268 kg (5,000 lb)	2,109 kg (4,650 lb)	2,200 kg (4850 lb)	EPA
Starting Time (s)	≤ 2 s	≤ 15 s	< 5 s	4 s	EPA
Ground Clearance (mm, (in))	198 mm (7.8 in)	≥ 178 mm (7 in)	168 mm (6.6 in)	165 mm (6.5 in)	EPA
Range (km, (mi))	> 580 m (360 mi)	≥ 320 km (200 mi)	418 km (260 mi)	399 km (248 mi)	CAR
ECOCAR COMPETITION TARGETS					
Fuel Consumption, CAFÉ Unadjusted, Combined, Team: UF Weighted (l/100km)	8.3 l/100km (28.3 mpgge)	7.4 l/100km (32 mpgge)	4.3 l/100km (54 mpgge)	3.2 l/100km (74 mpgge)	EPA
Charge Depleting Fuel Consumption (l/100km)	N/A	N/A	0 l/100km (ge)	0 l/100km (ge)	EPA
Charge Sustaining Fuel Consumption (l/100km)	N/A	N/A	8.8 l/100km(ge)	8.5 l/100km (ge)	EPA
Charge Depleting Range (km, (mi))	N/A	N/A	64.4 km (40 mi)	64 km (40 mi)	EPA
Petroleum Usage (kWh/km)	0.85 kWh/km	0.77 kWh/km	0.10 kWh/km**	0.08 kWh/km	EPA
Emissions	Tier II Bin 5	Tier II Bin 5	< Tier II Bin 5	Tier II Bin 6	EPA
WTW GHG Emissions (g/km)	250 g/km	224 g/km	210 g/km	190 g/km	EPA

TRC = Transportation Research Center (East Liberty, OH), **DPG-Y** = GM Desert Proving Grounds (Yuma, AZ), **CAR** = OSU Center for Automotive Research (Columbus, OH),**EPA** = Environmental Protection Agency (Ann Arbor, MI)

* Higher towing capacities have not been tested.
** Original VTS prediction for Petroleum Usage was based on gasoline instead of E85. Predicted value was updated to reflect this change.

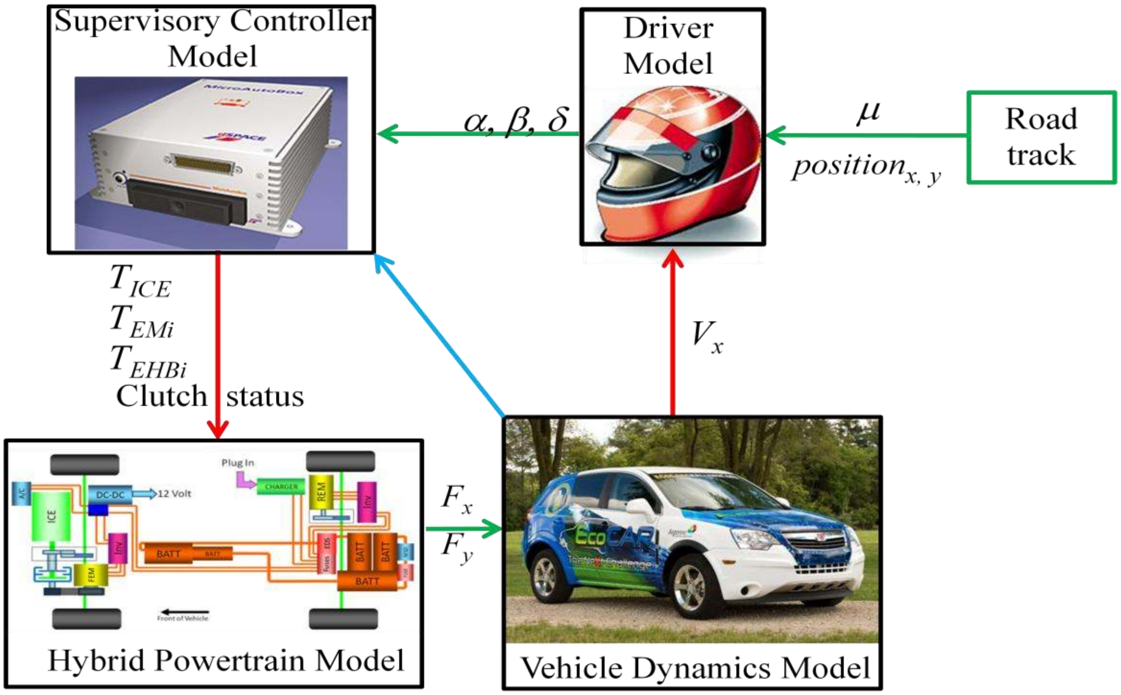

Figure 16 Top layer of EcoDYN, along with main inputs and outputs of the components

Different components of the simulators are explained next.

3.2.1. Driver Model

The hybrid SUV has a single speed gearbox and the engagement of the two clutches is commanded by the supervisory controller, depending on the energy management mode. Therefore the only driver inputs modeled in EcoDYN are accelerator and brake pedal positions and the steering wheel input. On a straight line motion where the steering wheel input is zero such as the case for the driving cycle simulations, the driver model for accelerator and brake pedal positions are computed by a PID controller representing the driver, expressed as:

$$\alpha \text{ or } \beta = k_p\left(V_{des} - V\right) + k_i \int \left(V_{des} - V\right) dt + k_d \frac{d}{dt}\left(V_{des} - V\right) \tag{10}$$

where α and β represent the accelerator and brake pedal positions depending on the sign of the PID output, and V_{des} is the desired speed.

The steering driver model manipulates the steering angle to compensate the error between the estimated position and the desired position on the road track. The estimated position x^* and y^* can be calculated from the following equations [37]:

$$x^* = x + \left(V_x \cos(\psi) - V_y \sin(\psi)\right) \frac{L_{look}}{\sqrt{V_x^2 + V_y^2}} \tag{11}$$

$$y^* = y + \left(V_x \sin(\psi) - V_y \cos(\psi)\right) \frac{L_{look}}{\sqrt{V_x^2 + V_y^2}} \tag{12}$$

where x^* is the estimated longitudinal displacement, y^* is the estimated lateral displacement, ψ is the vehicle heading angle, and L_{look} is the look ahead distance. The driver's response, which manipulates the steering angle δ that corresponds to the position error, is

$$\delta = PID(s)\sqrt{\left(x_d - x^*\right)^2 + \left(y_d - y^*\right)^2} e^{-\tau s} \tag{13}$$

where x_d is the desired longitudinal displacement, y_d is the desired lateral displacement, PID(s) is the PID control gain, and τ is the human-response-time constant for steering.

3.2.2. Powertrain Model

Modeling the hybrid powertrain is crucial since the proposed control strategy in this study considers blending regenerative motor braking with wheel friction braking.

3.2.2.1. Hybrid Powertrain: Battery and the Electric Motors Models

In this subsection, the defining equations for the battery and the motor models are given. The battery of the OSU EcoCAR vehicle is a 22 kWh lithium ion battery pack, composed of three modules in parallel, with each module consisting of 110 cells in series, as modeled in Figure 17.

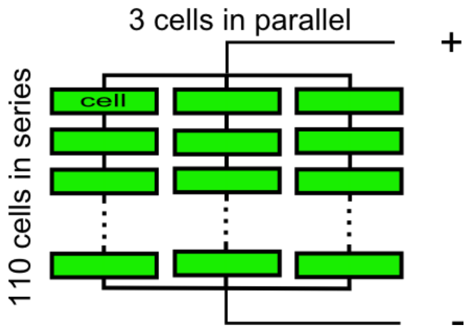

Figure 17 Battery architecture of the OSU EcoCAR vehicle.

The battery model used in EcoDYN is a zero-th order battery model used to estimate the battery state of charge (SOC). The equivalent circuit that represents the battery is shown in Figure 18. The voltage at the battery terminals V_{batt} is given by

$$V_{batt} = V_{oc} + R_{batt} I_{batt} \tag{14}$$

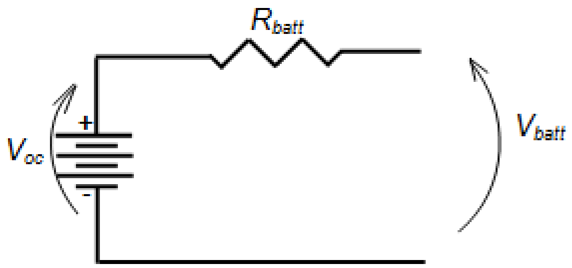

Figure 18 Equivalent circuit representing the battery.

where I_{batt} is the battery current, V_{batt} is the load voltage at battery terminals, R_{batt} and V_{oc} are the equivalent battery resistance and open circuit voltage which can be represented as functions of SOC of the battery respectively. Measured data for open circuit voltage as a function of the state of charge at room temperature for a single cell is shown in Figure 19.

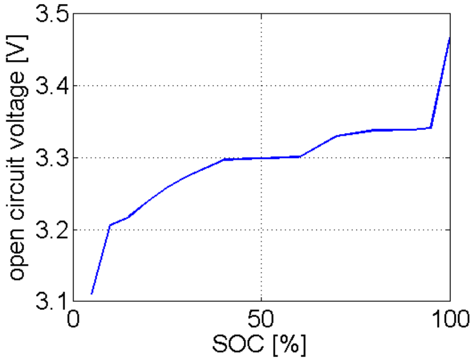

Figure 19 Open circuit voltage as a function of state of charge.

Battery power can be obtained by multiplying both sides of Equation 14 by battery current I_{batt}, and battery current can then be derived in terms of the battery power, open circuit voltage and the equivalent resistance as:

$$I_{batt} = \frac{\sqrt{V_{oc}^2 - 4R_{batt}P_{batt}} - V_{oc}}{2R_{batt}} \tag{15}$$

Using Equation 15, battery efficiency during charging can be derived as:

$$\eta_{batt} = \frac{V_{oc}I_{batt}}{P_{batt}} = \frac{V_{oc}\sqrt{V_{oc}^2 - 4R_{batt}P_{batt}} - V_{oc}^2}{2R_{batt}P_{batt}} \tag{16}$$

Note that the battery efficiency is the reciprocal of the expression given in Equation 16 during discharging as it is defined as $P_{batt}/V_{oc}I_{batt}$ for discharging.

The battery power on the other hand is composed of the motor power requests and the auxiliary load that can be expressed by:

$$P_{batt} = P_{acc} + \sum_i T_i \omega_i \cdot \left\{ \begin{array}{ll} \dfrac{1}{\eta_i(\omega_i, T_i)} & T_i \geq 0 \\ \eta_i(\omega_i, T_i) & T_i < 0 \end{array} \right\} \tag{17}$$

where P_{acc} is the electrical load of the accessories, T_i and ω_i are the motor speed and torque and η_i is the combined energy conversion efficiency of the ith electric machine and its power inverter. The efficiency map for the front electric motor is shown in Figure 20.

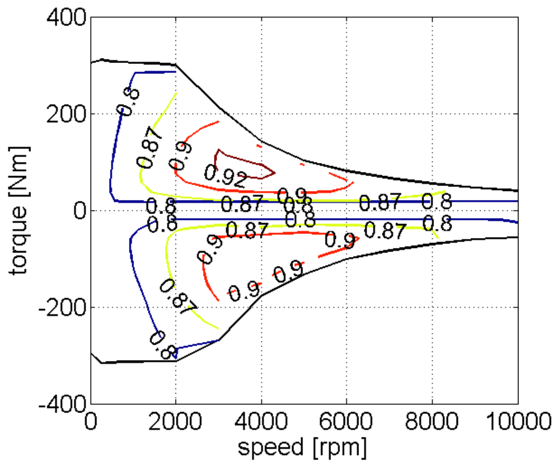

Figure 20 The efficiency contours as a function of speed and torque for the front electric motor

The dynamic response characteristics of the permanent magnet electric motors are represented by a first order system since the electric machines exhibit a short time lag between the torque request and the actual torque. The equation representing this relation can be expressed by:

$$\tau \frac{dT_{act}}{dt} + T_{act} = T_{req} \tag{18}$$

where T_{req} and T_{act} are the requested and realized torque respectively

3.2.2.2. Differential Model

The output shaft of the electric motor is connected to the differential, as shown in Figure 21a.

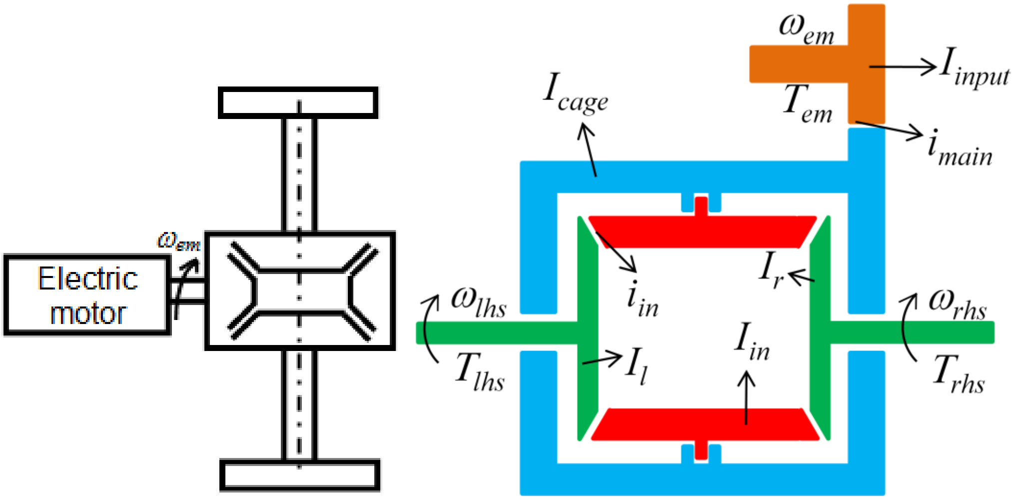

(a) An illustration of the rear powertrain (b) Open differential showing the inertia, speed and torque variables

Figure 21 The electric motor and the differential

The vehicle is equipped with open differentials. The differential mechanism is shown in Figure 21b, which has two degrees of freedom, namely the left and right half-shaft speeds. The input shaft speed can be calculated by:

$$\omega_{em} = 0.5 i_{main} \left(\omega_{lhs} + \omega_{rhs} \right) \tag{19}$$

where ω_{lhs}, ω_{rhs} are the left and right half shaft speeds respectively, and i_{main} is the transmission ratio of the differential main reduction gear.

The differential equations of motion are as follows:

$$\begin{bmatrix} I_{11} & I_{12} \\ I_{12} & I_{11} \end{bmatrix} \begin{Bmatrix} \dot{\omega}_{lhs} \\ \dot{\omega}_{rhs} \end{Bmatrix} = \begin{Bmatrix} 0.5 i_{main} T_{em} - T_{lhs} \\ 0.5 i_{main} T_{em} - T_{rhs} \end{Bmatrix} \tag{20}$$

and the elements in the differential inertia matrix can be derived as [38]

$$\begin{aligned} I_{11} &= \left(\left(I_{em} + I_{input} \right) i_{main}^2 + I_{cage} + I_{in} i_{in}^2 \right) 0.5^2 + I_{r/l} \\ I_{12} &= \left(\left(I_{em} + I_{input} \right) i_{main}^2 + I_{cage} - I_{in} i_{in}^2 \right) (0.5 - 0.5^2) \end{aligned} \tag{21}$$

3.2.2.3. Half-shaft Model

The half shafts are modeled as elastic rods with a damping coefficient. The transferred torque is proportional to the speed difference and twist angle between its terminals, i.e.

$$T_{ihs} = k_{hs} \int \left(\omega_{ihs} - \omega_i \right) dt + c_{hs} \left(\omega_{ihs} - \omega_i \right) \tag{22}$$

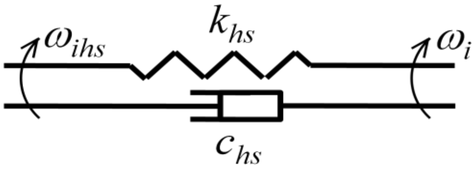

Figure 22 Half shaft model

where k_{hs} and c_{hs} are the torsional stiffness and damping coefficient of the half shafts respectively, and ω_{ihs} is the speed of the corresponding half shaft.

The final component that is considered before the wheels is the brake system.

3.2.2.4. Electro-hydraulic Brake (EHB) Model

The hybrid SUV considered in this study is equipped with EHB system that needs to be modeled as well. The hydraulic modulator of the EHB system along with its main components is shown in Figure 23.

Figure 23 Continental Teves© MK60 Brake Module. 1) Hydraulic block 2) Solenoid valves 3) Pump 4) DC motor for running the pump 5) Electronic control unit 6) Coils/solenoid group

The isolated brake circuit is composed of a pump, high pressure reservoir, inlet/outlet valve and wheel brake cylinder for each wheel, as well as a low pressure reservoir. The model of the isolated brake circuit and the dynamic variables for the portion of the circuit for a single wheel are shown in Figure 24 and Figure 25 respectively:

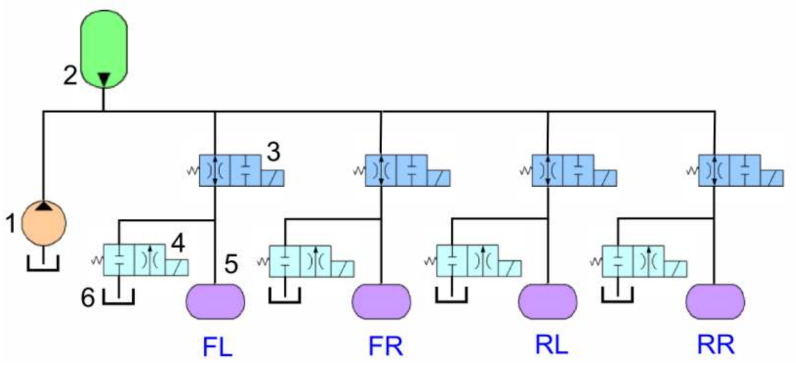

Figure 24 The electro-hydraulic brake circuit (1) pump, (2) high pressure reservoir, (3) inlet valve, (4) outlet valve, (5) wheel brake cylinder, (6) reservoir at ambient pressure

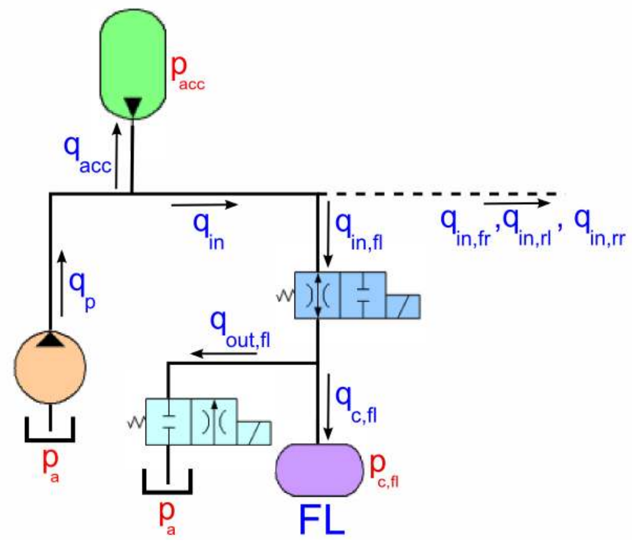

Figure 25 An illustration of the variables involved in the model

The pump works in order to maintain a specific pressure in the reservoir. The delivered flow rate is calculated from a look-up table with the pressure difference as the input [39].

$$q_p = f(p_{acc} - p_a) \tag{23}$$

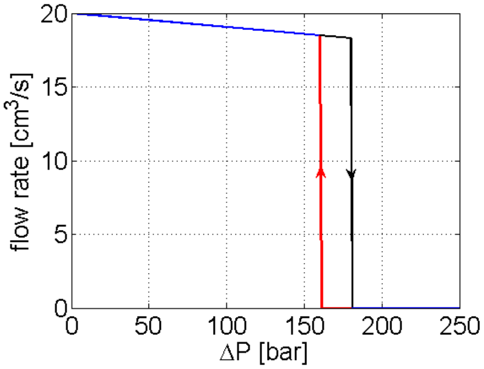

Figure 26 The pump characteristic for the flow rate vs. the input-output pressure difference.

The high-pressure reservoir is simulated as a hydro-pneumatic accumulator, which contains a bubble with gas that has greater compressibility than the hydraulic fluid. The accumulator is therefore able to absorb and deliver a relatively high quantity of hydraulic fluid. Based on the Poisson equation, the non-linear differential equation for the accumulator pressure can be written as [40]

$$\dot{p}_{acc} = \frac{q_{acc}\kappa p_{acc}}{V_o}\left(\frac{p_{acc}}{p_o}\right)^{1/\kappa} \tag{24}$$

where κ is the polytropic gas index and V_o is the initial volume of the fluid in the accumulator.

The valves are modeled as an orifice with a continuously controllable cross-section. The Bernoulli equation to calculate the valve flow can be written as [41]

$$q_{I/Oi} = Au_{I/Oi}\alpha\sqrt{\frac{2}{\rho}(p_{in} - p_{out})} \tag{25}$$

where $q_{I/Oi}$ is the fuel flow rate across the ith inlet/outlet valve, A is the orifice cross-section, α is the flow coefficient, ρ is the fluid density, and $u_{I/Oi}$ is the controlled input for pressure modulation.

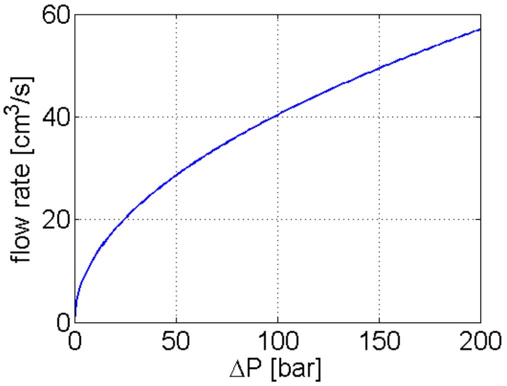

Figure 27 The inlet valve characteristics at wide open condition.

The wheel brake cylinder consists of a cylinder with a piston. The hydraulic fluid flows into the cylinder and pushes the piston with the friction pads onto the brake disc. The system is based on a lookup table that calculates the cylinder pressure from the cylinder volume [42].

$$V_c = \int q_c dt \tag{26}$$

$$p_c = g(V_c) \tag{27}$$

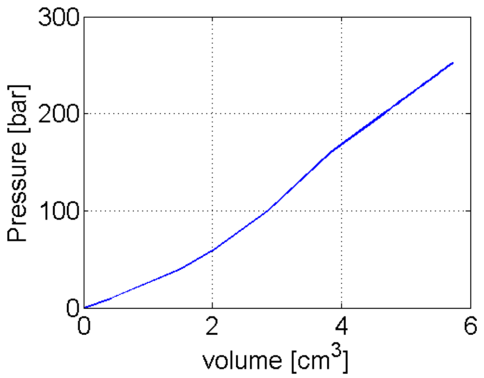

Figure 28 The wheel brake pressure as a function of the fluid volume in the cylinder.

The last component of the brake system is the brake discs. The brake torque is calculated as:

$$T_b=2\mu_B r_B A_B (p_c-p_a) \tag{28}$$

where μ_B is the brake disc friction coefficient (assumed to be constant), r_B is the radius between the contact point and center of the wheel, and A_B is the brake disc friction area.

EHB pressure control adopted: The control adopted is a closed loop control on the brake caliper pressures. The inputs and outputs are the desired braking torques T_{fbref} and the actual braking torques T_{fb} at each wheel respectively, as illustrated in Figure 29.

The first block on the left is used to convert the desired torque to desired pressure values. The difference between the desired pressure and the pressure measured for each calipers is amplified by the gain k which has a marginal importance, since it is preferable not to operate in a condition where the valve is partially open in order to avoid a slow system response. Saturation with a range of 0 to 1 is used after the gains because of limits of the cross sectional areas of the valves (refer to Equation 25). For the outlet valve there

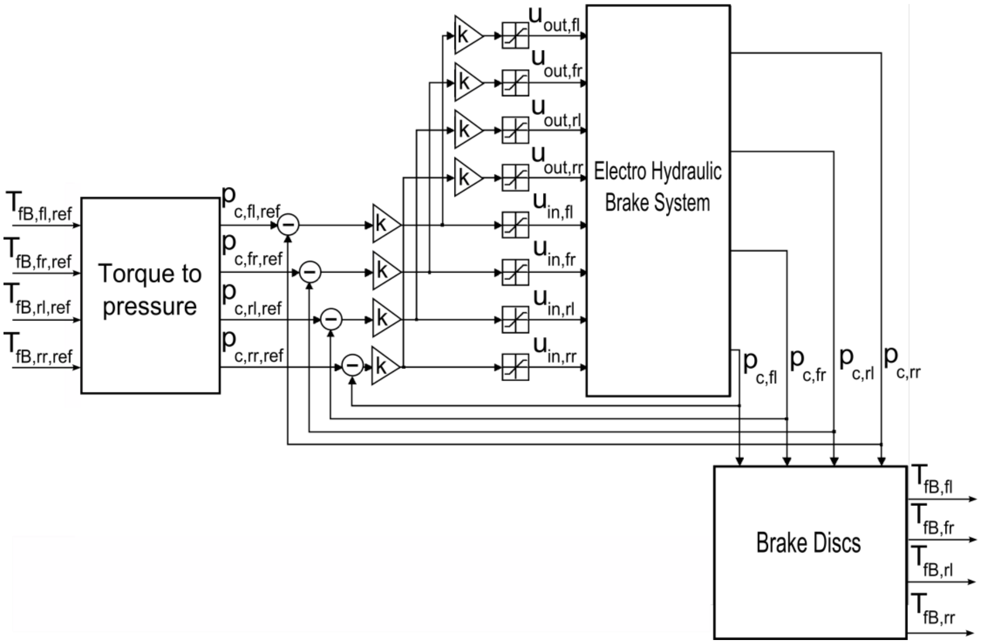

Figure 29 Block scheme of the EHB pressure control

is a negative unity gain of -1 before the saturation. Therefore if the objective is to increase the pressure in the caliper the corresponding inlet valve is opened and the outlet valve is closed, and vice versa if the target is to decrease the pressure in the caliper.

The response of the EHB system is depicted in Figure 30 when the input is a step of 180 bar followed by a complete pressure release.

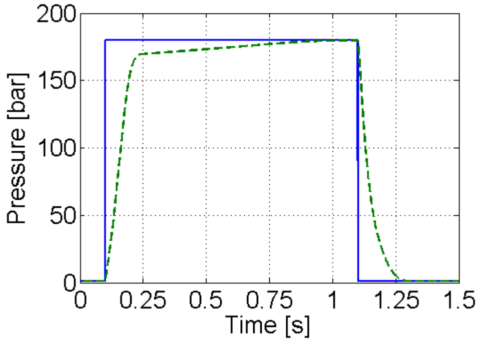

Figure 30 EHB time response characteristic for a step input of 180 bars of desired pressure

The time response characteristics of the system shows that 80 bar of effective pressure is reached inside the calipers in approximately 50 milliseconds. This value is well below the reference limit of 120 ms as imposed in [43].

3.2.2.5. Wheel and Tire Model

Wheel dynamics can be modeled as:

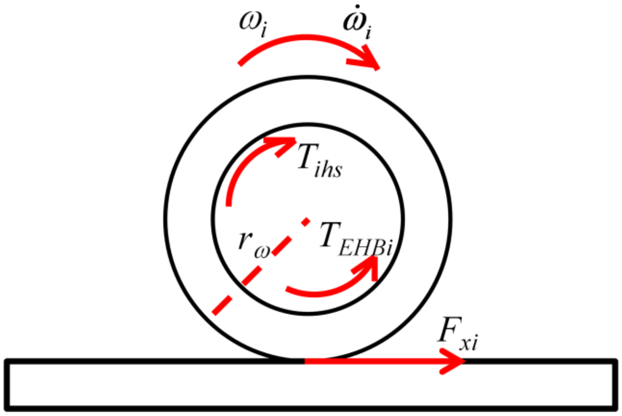

Figure 31 Wheel dynamics

$$\dot{\omega}_i = \frac{T_{ihs} - T_{EHBi} - r_\omega F_{xi}}{I_\omega} \tag{29}$$

where ω_i, F_{xi}, T_{ihs} and T_{EHBi} correspond to the rotational velocity, longitudinal force, half shaft torque and the brake torque on the corresponding wheel, or half shaft specified by the subscript *i* being either front left (*fl*), front right (*fr*), rear left (*rl*), or rear right (*rr*), and I_w is the wheel moment of inertia.

The Pacejka tire model for combined slip [44] is used to represent nonlinear tire behavior.

$$F_{xi} = \mu F_{zi} \sin(C_{xi} \arctan(B_{xi} s_i - E_{xi}(B_{xi} s_i - \arctan(B_{xi} s_i)))) \cos(\arctan(r_{Bx1} \cos(\arctan(r_{Bx2} s_i))\alpha_i)) \tag{30}$$

$$F_{yi} = \mu F_{zi} \sin(C_{yi} \arctan(B_{yi} \alpha_i - E_{yi}(B_{yi} \alpha_i - \arctan(B_{yi} \alpha_i)))) \cos(\arctan(r_{By1} \cos(\arctan(r_{By2} \alpha_i)) s_i)) \tag{31}$$

where μ is the adhesion coefficient, s_i and α_i are the longitudinal slip and slip angle of the corresponding tire, specified again by the subscript *i*. The model coefficients $C_{x/yi}$,$B_{x/yi}$ and $E_{x/yi}$ obtained from the tire manufacturer are given in *Appendix B*. Force surfaces representing the tire characteristics for longitudinal and lateral forces are shown in Figure 32.

The expressions for slip angle and transient slip are written as:

$$\alpha_{fl} = \delta - \arctan\left(\frac{V_y + ar}{V_x + \frac{t}{2} r} \right) \tag{32}$$

$$\alpha_{fr} = \delta - \arctan\left(\frac{V_y + ar}{V_x - \frac{t}{2} r} \right) \tag{33}$$

$$\alpha_{rl} = -\arctan\left(\frac{V_y - br}{V_x + \frac{t}{2} r} \right) \tag{34}$$

$$\alpha_{rr} = -\arctan\left(\frac{V_y - br}{V_x - \frac{t}{2} r} \right) \tag{35}$$

$$r_\omega \omega_i - V_i = V_i s_i + \sigma \dot{s}_i \tag{36}$$

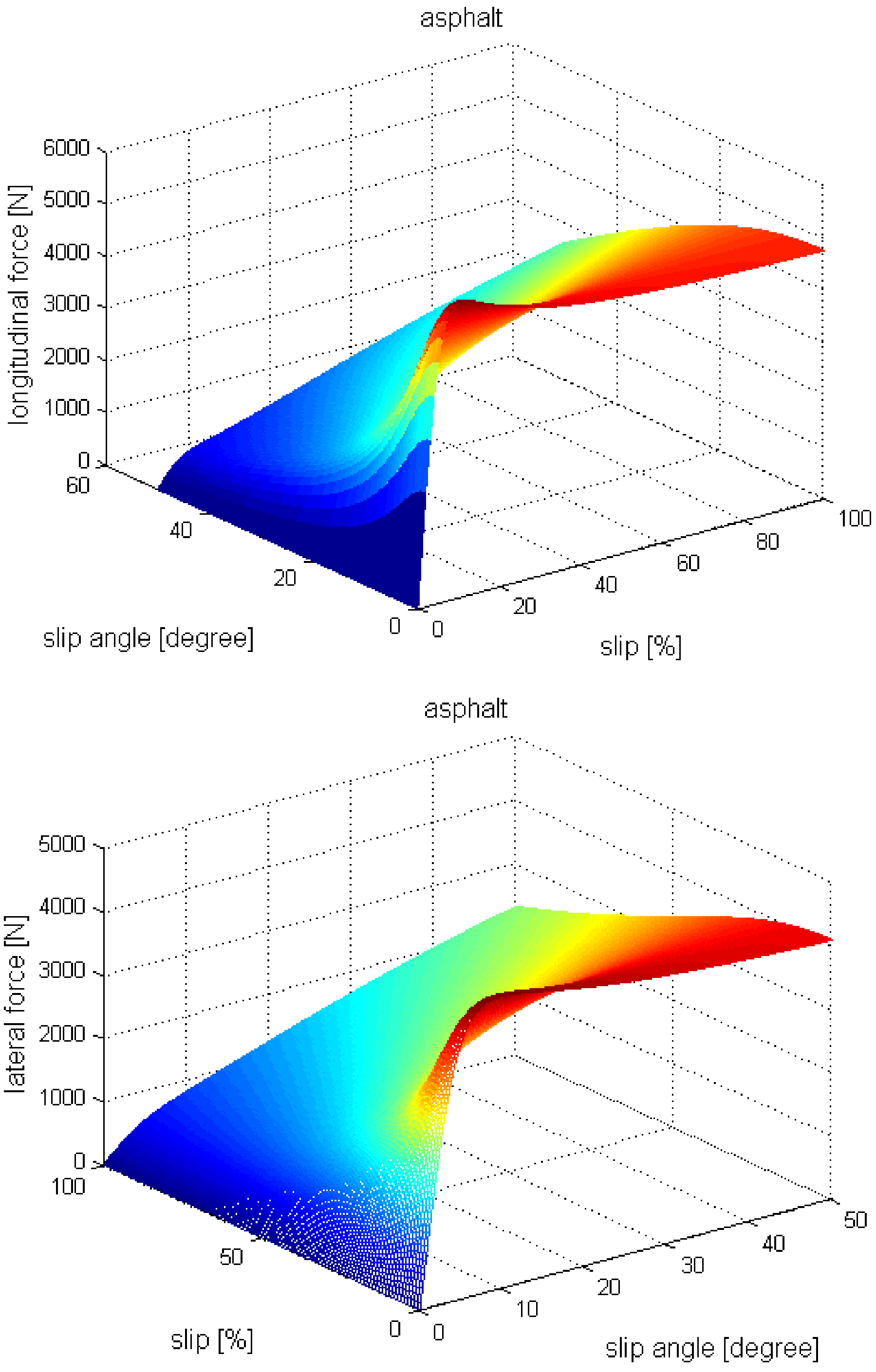

Figure 32 Longitudinal and lateral forces wrt. slip and slip angle on asphalt road surface

where V_x, V_y and r are longitudinal, lateral and yaw velocities respectively, δ is the steering angle, σ is the tire relaxation length and V_i represents the velocity component in wheel plane, and V_i is different for each wheel, expressed as:

$$V_{fl} = (V_x + \frac{t}{2} r)\cos(\delta) + (V_y + ar)\sin(\delta) \tag{37}$$

$$V_{fr} = (V_x - \frac{t}{2} r)\cos(\delta) + (V_y + ar)\sin(\delta) \tag{38}$$

$$V_{rl} = V_x + \frac{t}{2} r \tag{39}$$

$$V_{rr} = V_x - \frac{t}{2} r \tag{40}$$

3.2.3. Vehicle Dynamics Model

For the simulation of the vehicle and the designed stability controller, an accurate but simple vehicle model is required. Several models are available in the literature for this purpose, containing different degree of freedoms (DOF). Hence, a decision making process should be done judging the complexity of additional DOFs and loss-of-accuracy of neglected DOFs. Added DOFs generally result in increased computing time while the accuracy of the vehicle model slightly increases. On the other hand, some essential DOFs should not be neglected so that the vehicle simulation has the same behavior as the real vehicle.

Considering the motions of interest and other motions strongly related to these, the non-linear vehicle model considered in this study for simulation has 4 DOFs. These DOFs are the longitudinal and lateral motions, yaw, and roll. This 4 DOF model is used by many authors studying VSC [10, 27, 45-47], since Segel [48]. The pitch motion, suspension motions, suspension geometry, and body bounce motions are neglected since this study is generally about controlling the handling behavior of the vehicle. Contrary to the aim of this study, these DOFs are more important to ride comfort studies and are relatively unimportant in handling studies.

The local coordinate system is attached to the center of gravity of the vehicle and all equations are derived accordingly. Considering the hybridized powertrain, the sprung and unsprung masses are considered separately so that the suspension stiffness/damping effects on roll motion can be investigated more accurately. The roll axis is defined as the line connecting the roll centers of the front and rear axles and assumed to be stationary throughout the vehicle length. The tilting and restoring moments due to the roll motion is taken into account while deriving the equations.

The degrees of freedom are shown in Figure 33.

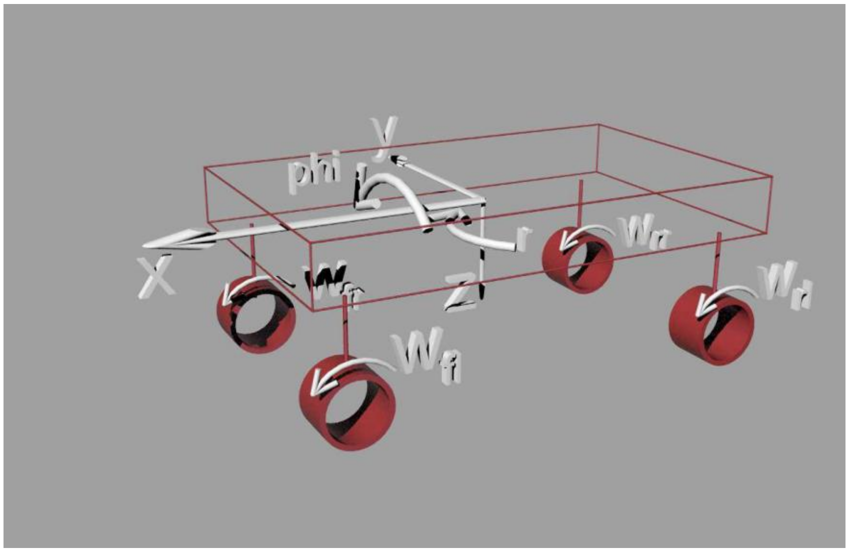

Figure 33 Vehicle model along with the DOFs utilized

As for the roll motion, the roll centers of the front and rear axles are assumed to be fixed during the motion of the vehicle. Furthermore, the rotational stiffness and damping constants for the roll motion are assumed to be fixed for the period of the roll motion. The forces derived from external sources, such as unbalanced loading of the car and road gradients etc., are neglected while deriving the equations of motion. However, longitudinal air drag is taken into account.

3.2.3.1. Equations of Motion and Their Representation

The Newtonian method is used to derive the equations of motion. The general free body diagram for the 4 DOF nonlinear vehicle model is shown in Figure 34. The roll motion's effects are shown using the free body diagram shown in Figure 34b.

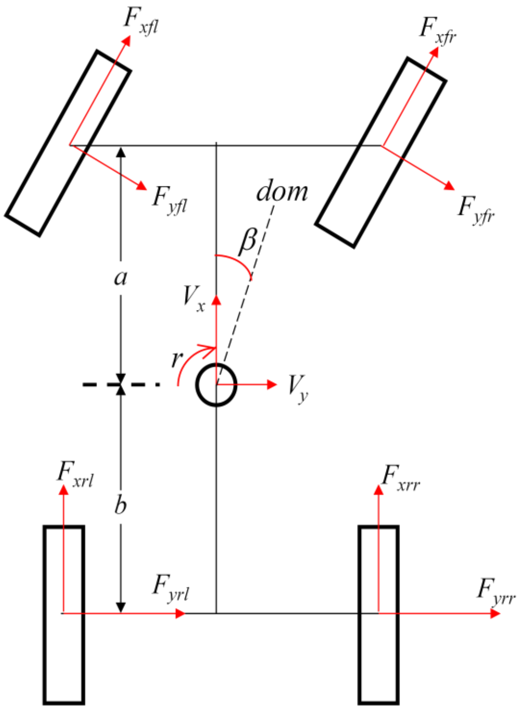

(a) Top view

continued

Figure 34 Different views of the vehicle model during a right turn

Figure 34 continued

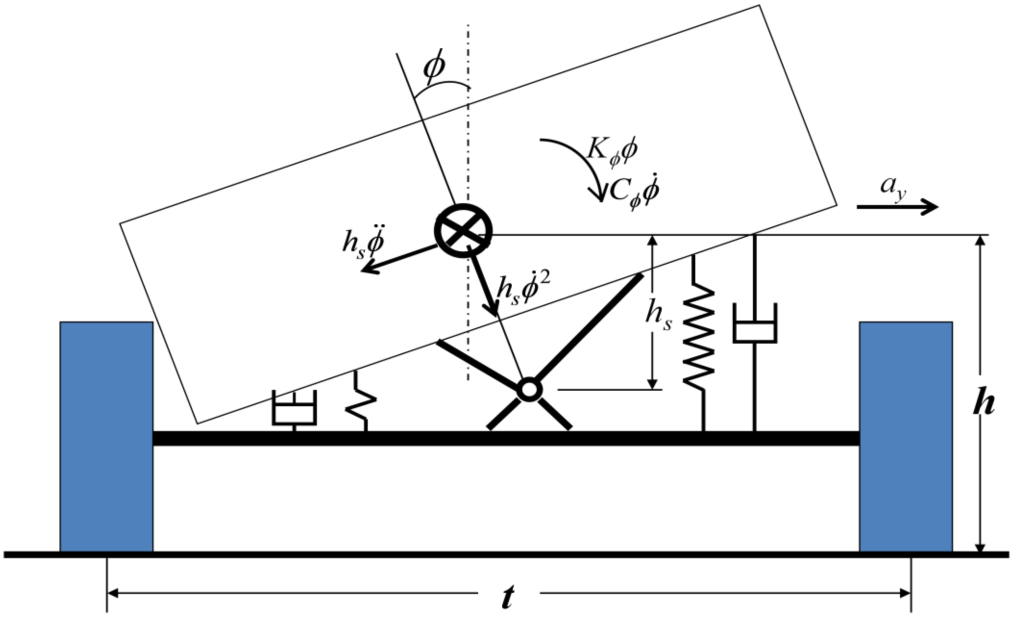

(b) Rear view

The general force equilibrium for the vehicle body in x-direction is as follows

$$M(\dot{V}_x - V_y r) + M_s h_s r \dot{\phi} = \sum F_x \tag{41}$$

where

$$\sum F_x = F_{xfl}\cos(\delta) - F_{yfl}\sin(\delta) + F_{xfr}\cos(\delta) - F_{yfr}\sin(\delta) + F_{xrl} + F_{xrr} - 0.047 C_D A_f V_x^2$$

(42)

The general force equilibrium for the vehicle body in y-direction is as follows

$$M(\dot{V}_y + V_x r) + M_s h_s \ddot{\phi}\cos(\phi) - M_s h_s \dot{\phi}^2 \sin(\phi) = \sum F_y \tag{43}$$

where

$$\sum F_y = F_{xfl}\sin(\delta) + F_{yfl}\cos(\delta) + F_{xfr}\sin(\delta) + F_{yfr}\cos(\delta) + F_{yrl} + F_{yrr} \tag{44}$$

and where V_x, and V_y are longitudinal and lateral velocities respectively, F_{xi} and F_{yi} represent the tire longitudinal and lateral forces respectively with the subscript i being either front left (*fl*), front right (*fr*), rear left (*rl*), or rear right (*rr*), δ is the steering angle of the front wheels, M is the total mass of the vehicle, M_s is the sprung mass, ϕ is the roll angle, A_f and C_d represent frontal area and the aerodynamic drag coefficient of the vehicle respectively, a and b are distances form front and rear axles to the center of mass, and l is the wheelbase, as illustrated in Figure 34a.

The equations for yaw and roll motion are coupled and these equations should be uncoupled before continuing.

$$I_{zz}\dot{r} - I_{xz}\dot{p} = \sum M_z \tag{45}$$

$$I_{xx}\dot{p} - I_{xz}\dot{r} = \sum M_x \tag{46}$$

where r and p are yaw and roll rates respectively. When the necessary elimination is done, the equations for the yaw and roll motion can be expressed as

$$\dot{r} = \frac{I_{xx}\sum M_z + I_{xz}\sum M_x}{I_{xx}I_{zz} - I_{xz}^2} \tag{47}$$

$$\dot{p} = \frac{I_{xz}\sum M_z + I_{zz}\sum M_x}{I_{xx}I_{zz} - I_{xz}^2} \tag{48}$$

Here, if mass symmetry of the real vehicles with respect to x and z axis is taken into account, the product of inertia I_{xz} term can be seen to have a significantly lower value relative to I_{xx} and I_{zz} in real vehicle data. Therefore, the terms with I_{xz} may be neglected. Then the equations simplify to

$$I_{zz}\dot{r}=\sum M_z=a\left(F_{xfl}\sin(\delta)+F_{yfl}\cos(\delta)+F_{xfr}\sin(\delta)+F_{yfr}\cos(\delta)\right)-b\left(F_{yrl}+F_{yrr}\right)$$
$$+\frac{t}{2}\left(F_{xfl}\cos(\delta)-F_{yfl}\sin(\delta)-F_{xfr}\cos(\delta)+F_{yfr}\sin(\delta)+F_{xrl}-F_{xrr}\right) \tag{49}$$

$$I_{xx}\dot{p}=\sum M_x=M_sh_s(\dot{V}_y+V_xr)+M_sh_sg\phi+M_{\phi f}+M_{\phi r} \tag{50}$$

where

$$M_{\phi f}=-K_{\phi f}\phi-C_{\phi f}\dot{\phi} \tag{51}$$

$$M_{\phi r}=-K_{\phi r}\phi-C_{\phi r}\dot{\phi} \tag{52}$$

with K_ϕ and C_ϕ representing roll stiffness and damping, respectively.

Up to this point, the motion of the vehicle is defined in terms of longitudinal and lateral acceleration along with yaw and roll angular acceleration. However, the normal load distribution changes due to longitudinal and lateral accelerations and yaw and roll motions should also be taken into account.

$$F_{zfl}=\frac{Mgb}{2l}-\frac{Ma_xh}{2l}+\frac{Ma_ybh}{2lt}+\frac{M_{\phi f}}{t} \tag{53}$$

$$F_{zfr}=\frac{Mgb}{2l}-\frac{Ma_xh}{2l}-\frac{Ma_ybh}{2lt}-\frac{M_{\phi f}}{t} \tag{54}$$

$$F_{zrl}=\frac{Mga}{2l}+\frac{Ma_xh}{2l}+\frac{Ma_yah}{2lt}+\frac{M_{\phi r}}{t} \tag{55}$$

$$F_{zrr}=\frac{Mga}{2l}+\frac{Ma_xh}{2l}-\frac{Ma_yah}{2lt}-\frac{M_{\phi r}}{t} \tag{56}$$

3.2.3.2. Longitudinal Vehicle Dynamics Model Validation

The 4 DOF model described above has been used by many authors studying vehicle stability control for decades, as mentioned previously. Therefore a great effort was not put in validating the model with vehicle tests. Figure 35 and Figure 36 show real measured data versus simulation results for the start from standstill test and the step steer tests at two different constant velocities on asphalt, respectively. The tests were carried out at the proving grounds of the Transportation Research Center [49]. The torque commands and steering wheel angle sensor output collected from the supervisory controller of the vehicle during the test was fed into the vehicle simulator and the results for wheel speeds, vehicle speed, yaw rate and lateral acceleration were compared..

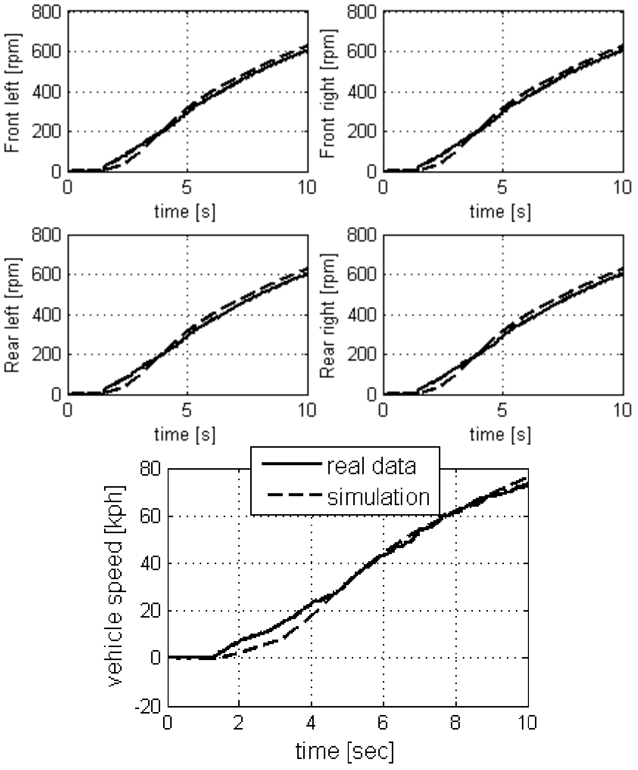

Figure 35 Comparison of the simulator output and real data for wheel and vehicle speeds during a start from standstill test.

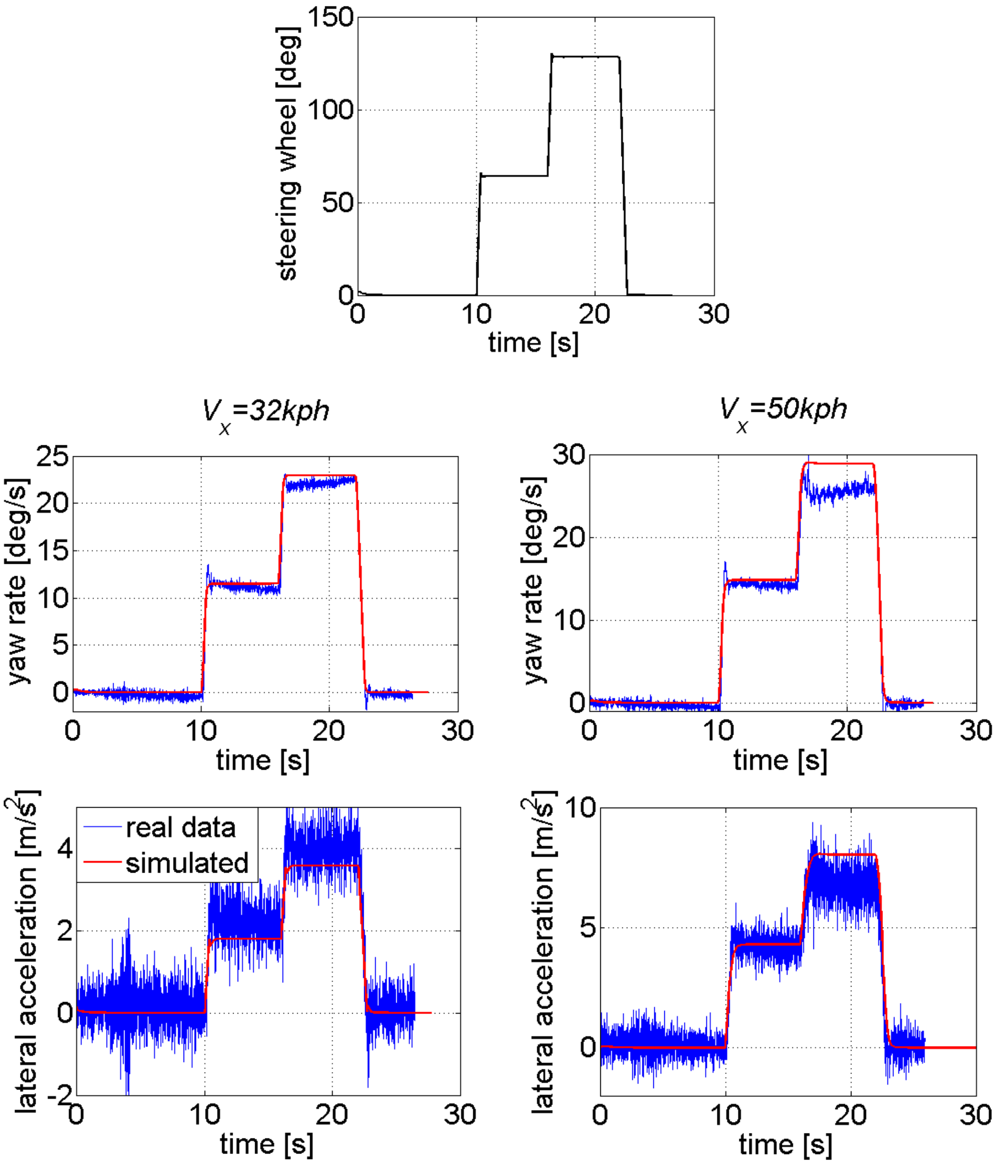

Figure 36 Comparison of the simulator output and real data for step steer test during cruising at two different speeds.

3.2.4. Supervisory Controller Model

The supervisory controller model, as implemented in EcoDYN simulator, is composed of two layers, as shown in Figure 37, the high-level controller and energy management strategy/vehicle dynamics control.

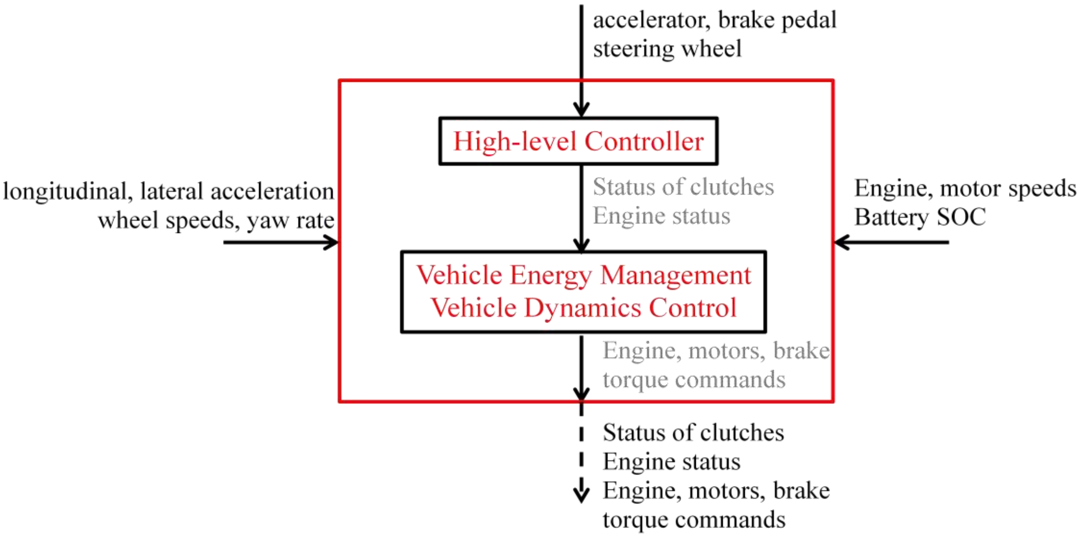

Figure 37 Overview of the supervisory controller

The supervisory control strategy decides the state of the clutches, or driving mode, depending on SOC, vehicle speed and pedal positions. The OSU EcoCAR vehicle's twin-clutch transmission allows the vehicle to operate in multiple modes in order to optimize vehicle performance under various driving conditions. Different operating modes depending on the state of the clutches are shown in Figure 38.

The VSC proposed in this dissertation considers the electric all wheel drive mode when Clutch 1 is disengaged and Clutch 2 is engaged (top right mode in Figure 38). In this operating mode both of the electric motors are connected to the wheels so both axles can be utilized for traction or regenerative braking while the engine is disconnected from the powertrain in order to avoid the energy dissipation caused by engine drag. More information on other modes, switching conditions, and details on the fuel consumption minimization strategy applied during these modes can be found in [35].

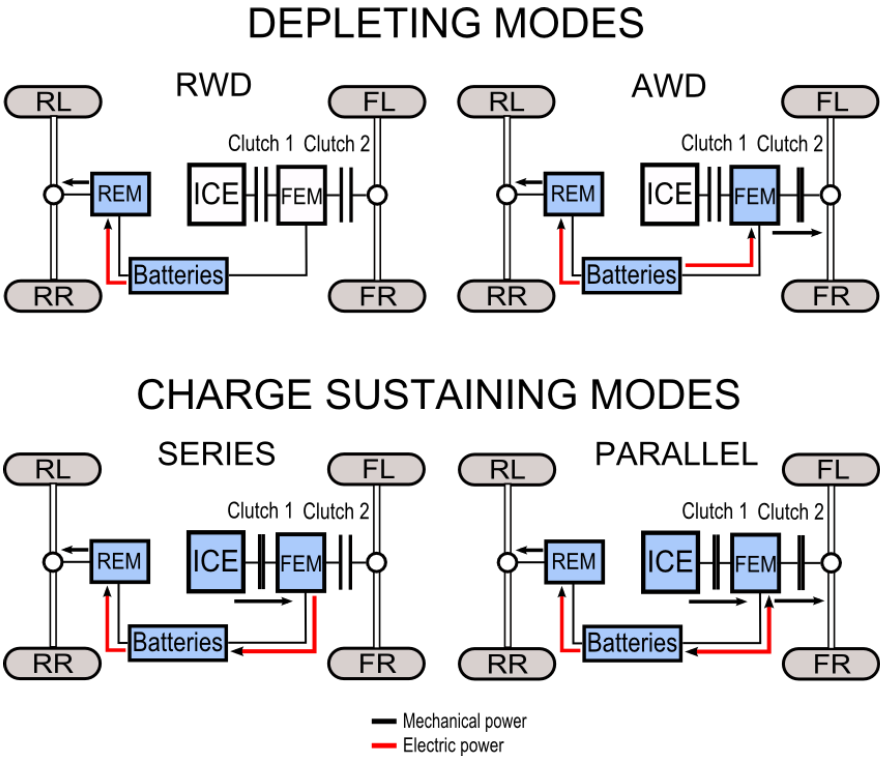

Figure 38 An illustration of the different operating modes of operation.

3.2.5. Vehicle State Estimation

Standard sensors in a VSC system are the yaw rate sensor, the lateral and longitudinal acceleration sensors, the wheel rotational speed sensors, the steering angle sensor and the brake pressure sensors. Some of these sensors along with the EHB module are shown in Figure 39. These sensors are used for determining the driver demand and the vehicle's actual response. Some variables such as vehicle speed, road friction coefficient, and vehicle sideslip angle cannot be measured directly, so these parameters can be estimated from existing sensor information.

There are a few alternatives for measuring vehicle speed. Among these are optic Correvit sensor, Doppler-Radar and GPS. Although these tools provide quite accurate speed measurement, they are costly and unsuitable for mass produced vehicles. On the other hand, estimation of vehicle speed using four wheel speed sensors that are already present in a production vehicle has already been studied extensively in the literature. In this method, the average value of the undriven wheel speeds are taken into account during normal driving. During braking or all wheel driving, estimation is performed using

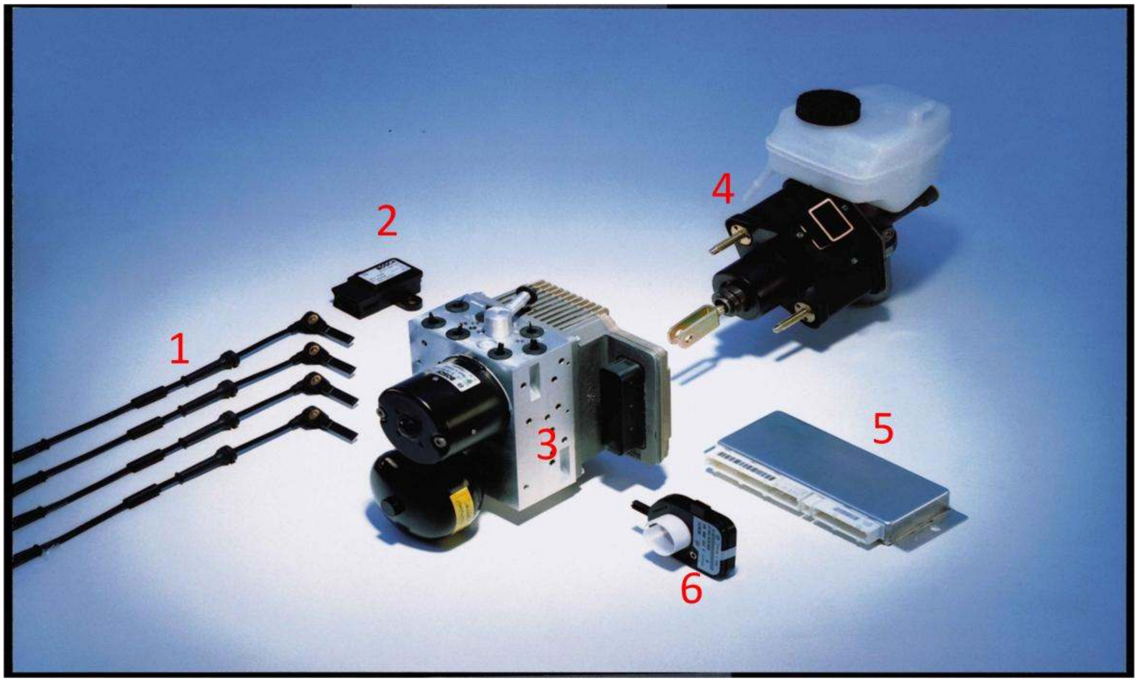

Figure 39 Basic components of Sensotronic Brake Control system, Daimler Chrysler AG® 1) Wheel speed sensors 2) Yaw rate and lateral acceleration sensor 3) Hydraulic modulator 4) Reservoir 5) Remote mounted ECU 6) Steering wheel angle sensor

all wheel speeds by giving a higher weighting to the fastest wheels during braking, and slowest wheels during traction. However this method also has a few drawbacks. It does not recognize changing rolling radius that may be due to tire wear in time. Furthermore slip in all wheels during all wheel driving or braking is a problematic case. Despite those problems, the speed estimation using wheel speed sensors gives a maximum error of 2% [4]. To enhance the estimation, accelerometer measurements are used in addition to the wheel speed measurement can be used with a Kalman filter approach. Some examples for this approach are given in [26, 50, 51].

In this study, vehicle longitudinal speed is assumed to be measured or estimated with sufficient accuracy.

Coefficient of friction estimation has been also studied in literature [52-54]. The selected estimation method should be robust during braking and/or steering situations as is the case for VSC studies. Also the estimation algorithm should not depend on the traction/braking force distribution ratio between the front and rear axles since the distribution is changing dynamically for VSC.

For the estimation of friction coefficient, the approach in [54] is utilized in this study. Once the vehicle speed is known, the slip can be calculated. Therefore, the friction coefficient estimation relies on the knowledge of longitudinal or lateral forces. Once they are known the friction coefficient can be estimated using a look-up table. Inverting the wheel dynamics equation yields

$$F_{xi} = \frac{T_{ihs} - T_{EHBi} - I_{\omega}\dot{\omega}_i}{r_{\omega}} \tag{57}$$

where T_{EHBi} is the pressure in the calipers and is measured directly via pressure transducers. The half shaft torque is obtained from motor and/or engine torque from the motor/engine controllers. Finally the wheel acceleration can be obtained by differentiating the wheel speed measurement. In case derivation is not desired due to potential instability issues in the real time controller, the following linear observer can be utilized:

$$I_\omega \dot{\hat{\omega}} = T_{ihs} - T_{EHBi} - r_\omega \hat{F}_{xi} + l\tilde{\omega} \tag{58}$$

$$\dot{\hat{F}}_{xi} = -\eta\tilde{\omega} \tag{59}$$

where $\tilde{\omega}_i = \omega_i - \hat{\omega}_i$ and $\tilde{F}_{xi} = F_{xi} - \hat{F}_{xi}$ is the estimation error for wheel speed and longitudinal tire force respectively. The error dynamics can be derived as:

$$\begin{Bmatrix} \dot{\tilde{\omega}}_i \\ \dot{\tilde{F}}_{xi} \end{Bmatrix} = \begin{bmatrix} \dfrac{-l}{I_\omega} & \dfrac{-r_\omega}{I_\omega} \\ \eta & 0 \end{bmatrix} \begin{Bmatrix} \tilde{\omega}_i \\ \tilde{F}_{xi} \end{Bmatrix} + \begin{bmatrix} 0 \\ 1 \end{bmatrix} \dot{F}_{xi} \tag{60}$$

It can be shown that the error dynamics are stable by choosing the positive gains l and η such that $l^2/\eta \leq 4r_\omega I_\omega$ yields negative eigenvalues.

Once the longitudinal force is computed, the remaining task is using the tire model in an inverse manner to calculate the friction coefficient. Recall from Equation 30, Equation 31 and Figure 32 that slip, slip angle, normal load on the tire and the friction coefficient contribute to the generation of longitudinal and lateral forces. Therefore the map that computes the friction coefficient is shown in Figure 40.

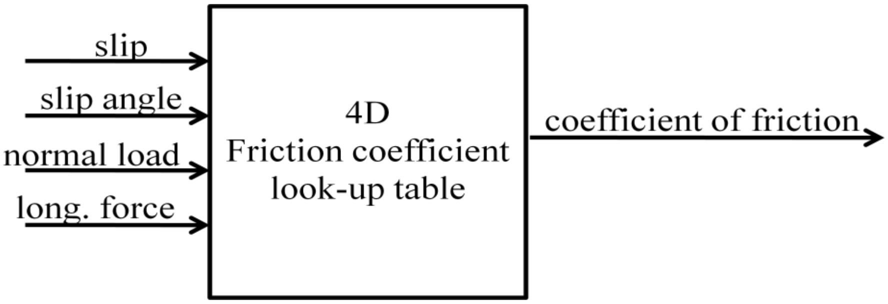

Figure 40 Friction coefficient estimator

Since both slip and slip angle depend on the knowledge of lateral velocity, or sideslip angle (Equations 32 through 40), the coefficient of friction estimation relies on the estimation of lateral velocity, or sideslip angle (yaw velocity is already measured.) Lateral velocity can be estimated with a Kalman filter approach using the lateral acceleration and yaw rate measurements as explained in [14]. In this study, lateral velocity is assumed to be measured or estimated with a sufficient accuracy.

3.3. Summary of this Chapter

The vehicle platform and its architecture are introduced in this chapter for which the proposed VSC scheme is developed. The vehicle simulator EcoDYN that represents the dynamic model of this hybrid SUV is also explained with the model equations for the driver, powertrain, and vehicle dynamics models. The structure of the supervisory controller is also described.

4. Vehicle Stability Control for Hybrid Electric Vehicles

This chapter is composed of two sections. Section 4.1 presents a literature survey on VSC strategies developed specifically for HEVs equipped with axle motors, such as the hybrid SUV considered in this dissertation. Section 4.2 presents the results of simulations of the response of the vehicle to the steering maneuvers considered in Section 2.4 for the SUV with the conventional version of the powertrain (front wheel drive engine); this time the simulations are carried out for the hybridized version of the SUV, described in Chapter 3. The objective of this chapter is to evaluate the potential benefits afforded by a hybrid powertrain with respect to VSC.

4.1. Literature on VSC for HEVs

If one considers the braking decision discussed earlier and illustrated in Figure 10, it becomes clear that, instead of braking the inner wheels and outer wheels to prevent understeering and oversteering respectively, accelerating the outer wheels and the inner ones can be an alternative solution. If this can be achieved in a rapid way, comparable to the speed of brake actuation, it may be possible to achieve the end goal of VSC without sacrificing performance. Electric and hybrid vehicles can, in principle, provide this functionality.

Most of the studies that focus on vehicle stability control for HEVs, consider independently braked/driven and/or steered wheels [30, 33-35, 55, 56]. However not many studies concentrate on combining axle motor traction/braking with individual wheel braking [19, 21, 57, 58]. In some of these studies [21, 57], rule based fuzzy approaches similar to the ones described in the previous section are applied to combine differential friction braking with regenerative axle motor braking.

For instance [20] proposes generating a yaw moment using the rear motor regenerative braking during oversteering; this causes a decrease in slip angle of the rear wheels inducing a compensatory understeering tendency. If that is not sufficient to keep the sideslip angle in the stable limit, the yaw moment is further decreased by individual wheel friction braking. In a similar fashion, during understeering, the rear motor is controlled to provide tractive torque, which increases the rear tire slip angles and the oversteering tendency. If that is not sufficient to track the desired yaw rate, the yaw moment is increased by individual wheel braking.

Cheong [19] also assumes a HEV architecture equipped with two axle motors. A 2DOF control oriented model for yaw rate and sideslip angle is used to design a sliding mode controller to find the corrective yaw moment in order to track the desired yaw rate and achieve zero sideslip angle. The paper does not describe how this corrective yaw moment is distributed to motor and/or friction braking.

Hancock [57] suggests, that applying regenerative braking to the rear axle can degrade vehicle stability, since it causes weight transfer onto the front wheels, which in turn results in a loss of lateral force at the rear (i.e. increase in rear slip angles inducing oversteering tendency). The resulting reduction in stability can be contained by brake-actuated VSC with an increase in brake pressures, for high friction surfaces, but for slippery surfaces the reduction in stability is much more severe and cannot be compensated with brake-actuated VSC. In order to resolve this issue two solutions are considered: first, simply switching to friction braking once the longitudinal slip of either rear wheel exceeds a specified threshold and, second, locking the central diferential.

In reference [58] friction braking at four corners is blended with rear axle motor braking with the control objective stated as: "Maximize the regenerative braking while (i) delivering the requested braking force (ii) limiting the yaw rate tracking error and (iii) fulfilling constraints on the maximum regenerative braking set by the hybrid powertrain." Simulation results show that maximization of the rear axle regenerative braking induces oversteering of the vehicle, which is compensated by individual wheel braking. So the recuperation energy maximized by regenerative braking brings the cost of dissipating more energy by increasing the friction braking to compensate the oversteering effect. This observation also matches [57]; i.e. while utilizing energy recuperation by regenerative braking; additional friction braking is needed to provide stability of the vehicle, which may yield the same net energy consumption in the end.

This brief literature survey conducted for VSC strategies specifically for HEVs equipped with axle motors can be summarized as follows: Axle motor braking and/or traction is either disabled or treated as a separate actuation combined with individual wheel braking via rule based fuzzy approaches. There is no consensus on how to use axle electric motors within a VSC scheme. In this chapter, we explore this question using simulation tools.

4.2. Simulations For The Fuzzy Controllers with the Hybrid Powertrain

To analyze potential benefits of using electric motors within the VSC scheme, the steering maneuvers simulated for the vehicle with the conventional powertrain (front wheel drive engine) in Section 2.4 are reconsidered this time for the hybridized version of the powertrain. The rule based controllers mentioned for the two fuzzy VSC schemes in Section 2.3 are kept unchanged, but the only difference this time is that the traction and braking command coming from the driver is satisfied by the electric motors, instead of the engine. In other words these simulations can be considered equivalent to keeping the stock brake actuated VSC scheme and utilizing the electric motors for traction and braking. This can be expressed as:

$$T_{EMi} = \alpha T_{EM\max i}\left(\omega_{EMi}\right) + \beta T_{EM\min i}\left(\omega_{EMi}\right) \tag{60}$$

where T_{EMi} and ω_{EMi} are the electric motor torque command and speed for the front or rear motor, respectively, α and β are the accelerator and brake pedals respectively. T_{EMmaxi} and T_{EMmini} represent the maximum and minimum torque limits of the motors corresponding to the motor speed. Note that Equation 60 represents the simplest control that can be applied to the motors in supplying the torque demanded by the driver.

For the lane change maneuvers on both dry and wet asphalt, and the J-turn maneuver on dry asphalt, Fuzzy1 controller is selected, and for the J-turn maneuver on wet asphalt, Fuzzy2 controller is selected and named as the stock VSC scheme from this point on, as the aim is not to compare different fuzzy schemes but the stock differential braking VSC with and without the electric motors.

Simulation results are shown in Figure 41. The longitudinal speed, sideslip angle, yaw velocity, and the vehicle trajectory are shown at the top, for the vehicles controlled by the stock fuzzy controller utilizing the conventional (F Con) and the hybrid (F Hyb) powertrains. The desired values for speed, yaw rate and trajectory, and the sideslip angle threshold are also shown in the plots. Brake and engine/motor torque profiles are given for these two configurations for each maneuver at the bottom. Simulation results for the vehicle without VSC for each maneuver are also shown. Tables showing maximum and root mean square (RMS) of the deviation of yaw rate and speed from the desired values, maximum sideslip angle and deviation from the allowed sideslip angle threshold (if any) and the energy consumption while VSC is active are also included for each maneuver and configuration as well. For the F Hyb scheme, the energy consumed is calculated as $E_{net}=E_{batt}+E_{braking}$ where:

$$E_{batt} = \int_{\substack{VSC \\ on}} V_{oc} I_{batt} dt \tag{61}$$

$$E_{brake} = \sum_{i=1}^{4} \int_{\substack{VSC \\ on}} \omega_i T_{EHBi} dt \tag{62}$$

The main observation from the lane change maneuver simulation results of Figure 40a and 40b that compare the utilization of the conventional and hybrid powertrains for VSC is that the involvement of the electric motors to provide tractive torque prevents the decrease in vehicle speed in comparison to the vehicles controlled by the stock VSC. As a

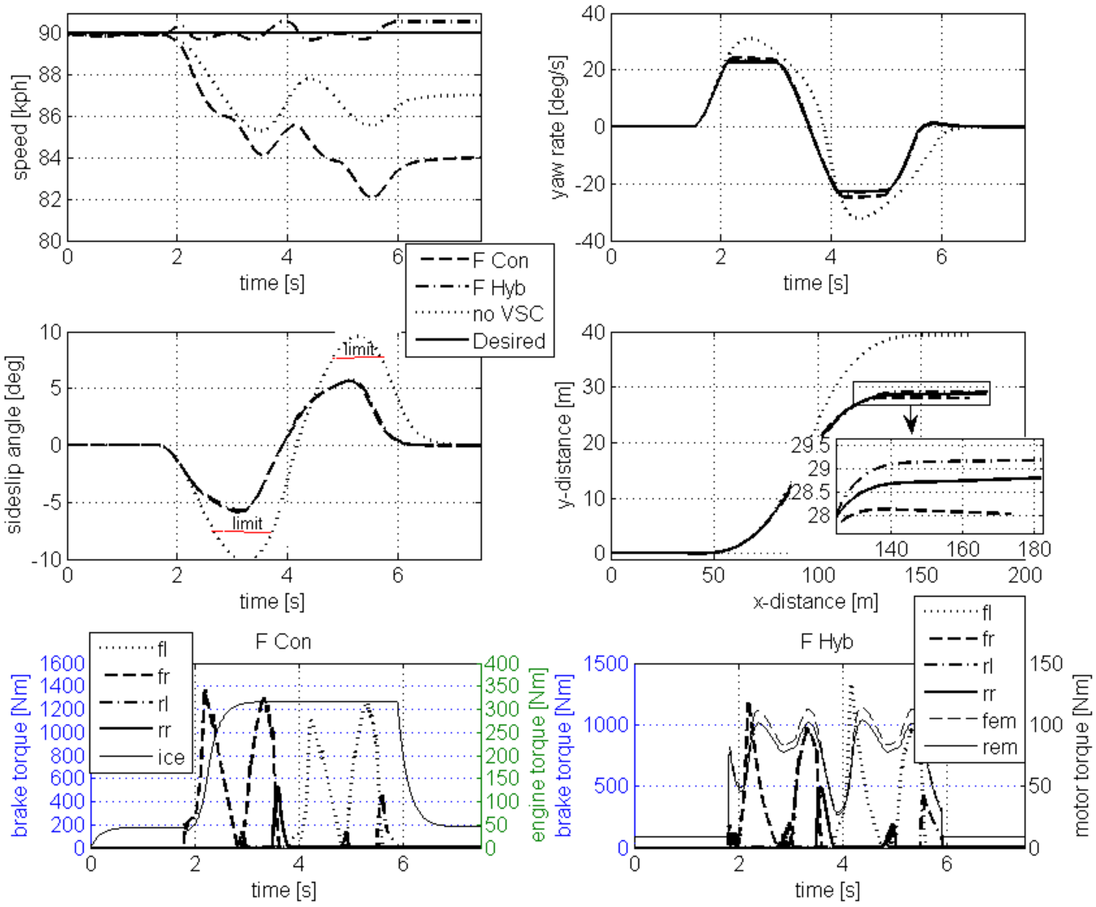

Powertrain	$(V_{x\_error})_{max}$ *[kph]*	$(V_{x\_error})_{rms}$ *[kph]*	$(r_{error})_{max}$ *[deg/s]*	$(r_{error})_{rms}$ *[deg/s]*	β_{max} *[deg]*	$(\beta_{deviation})_{max}$ *[deg]*	Consumed energy *[kJ]* *(Tractive/Battery+Brake=Total)*
Con	7.92	5.14	1.30	0.71	5.91	-	724.8+165.4=890.2
Hyb	0.59	0.24	1.34	0.51	5.77	-	487.3+134.8=625.1

(a) Lane change dry asphalt

continued

Figure 41 Simulation results comparing the stock VSC scheme with and without the electric motors

Figure 41 continued

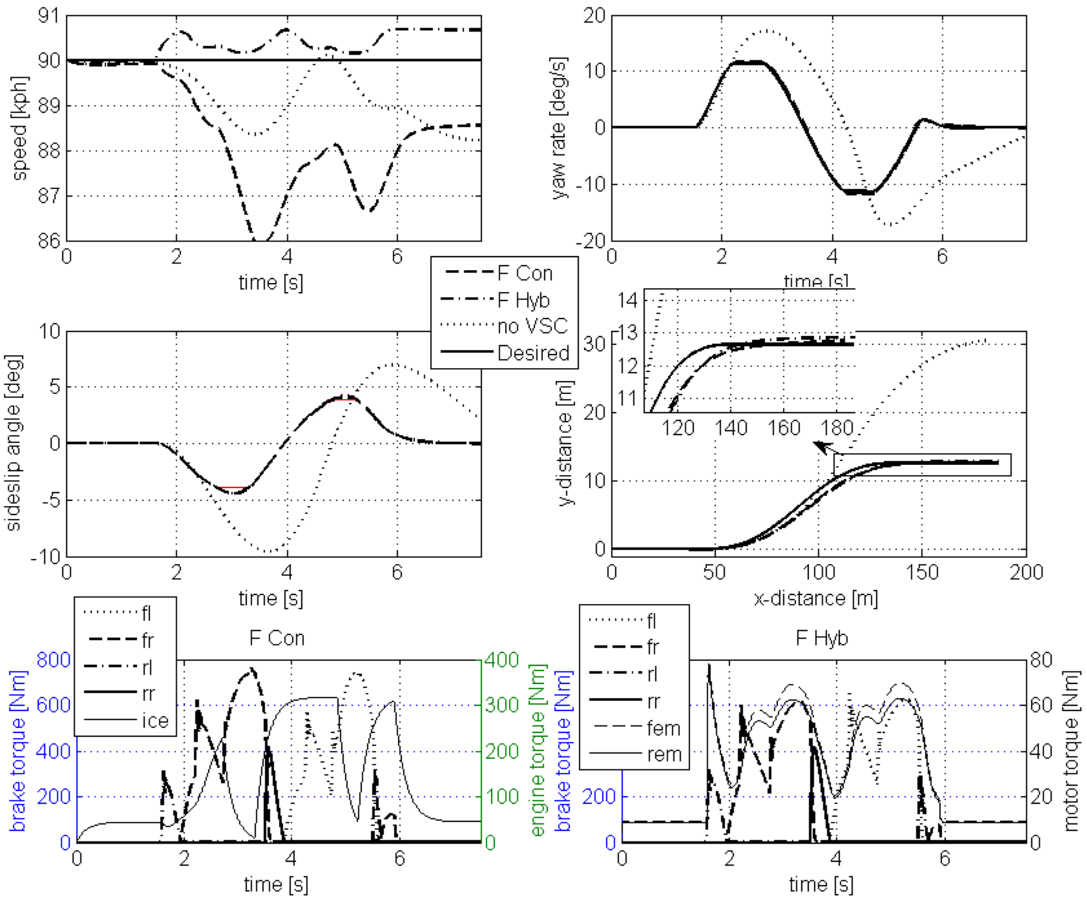

Powertrain	$(V_{x\_error})_{max}$ *[kph]*	$(V_{x\_error})_{rms}$ *[kph]*	$(r_{error})_{max}$ *[deg/s]*	$(r_{error})_{rms}$ *[deg/s]*	β_{max} *[deg]*	$(\beta_{deviation})_{max}$ *[deg]*	Consumed energy *[kJ]* *(Tractive/Battery+Brake=Total)*
Con	4.13	2.48	0.65	0.39	4.44	0.56	458.2+122.0=580.2
Hyb	0.68	0.36	0.50	0.34	4.41	0.53	301.3+119.8=421.1

(b) Lane change wet asphalt continued

Figure 41 continued

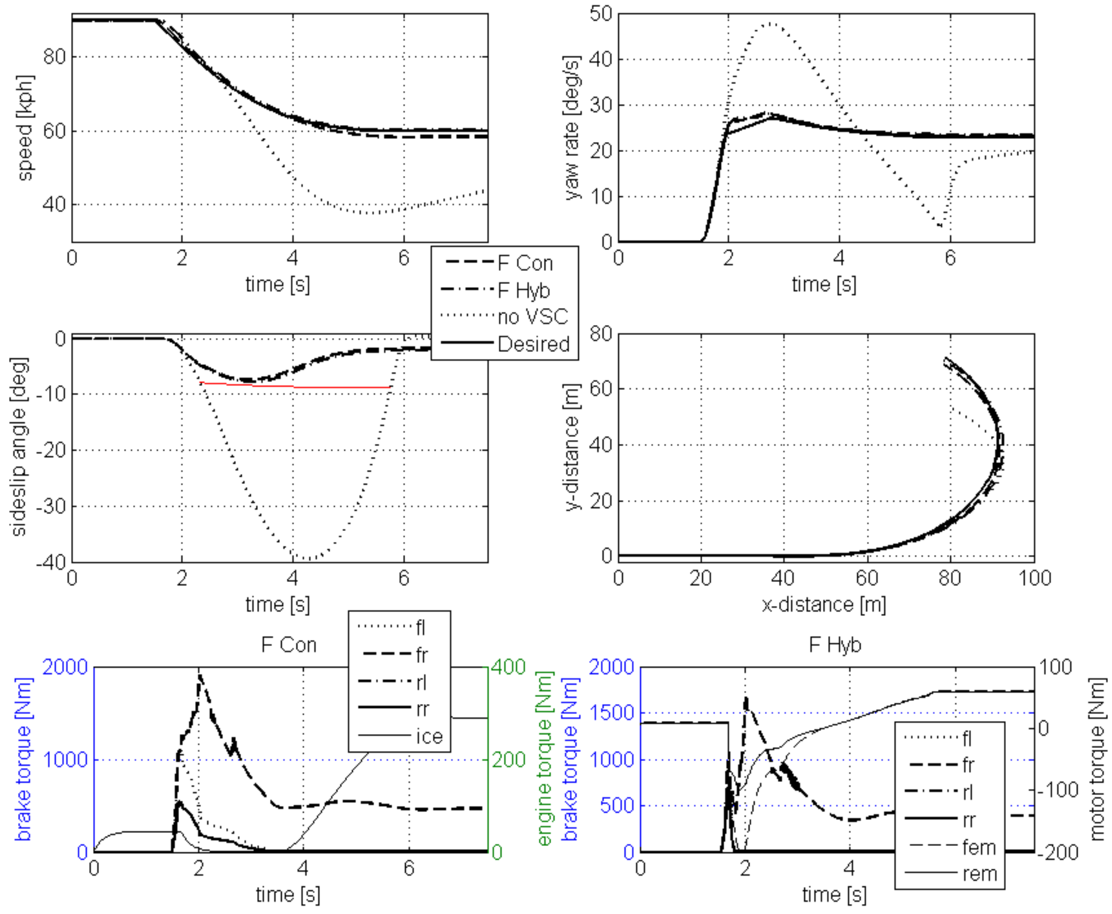

Powertrain	$(V_{x\_error})_{max}$ *[kph]*	$(V_{x\_error})_{rms}$ *[kph]*	$(r_{error})_{max}$ *[deg/s]*	$(r_{error})_{rms}$ *[deg/s]*	β_{max} *[deg]*	$(\beta_{deviation})_{max}$ *[deg]*	Consumed energy *[kJ]* *(Tractive/Battery+Brake=Total)*
Con	1.76	1.19	1.78	0.63	7.39	-	353.6+294.5=648.0
Hyb	2.50	1.09	2.44	0.87	7.76	-	96.0+185.4=281.4

(c) J-turn dry asphalt continued

Figure 41 continued

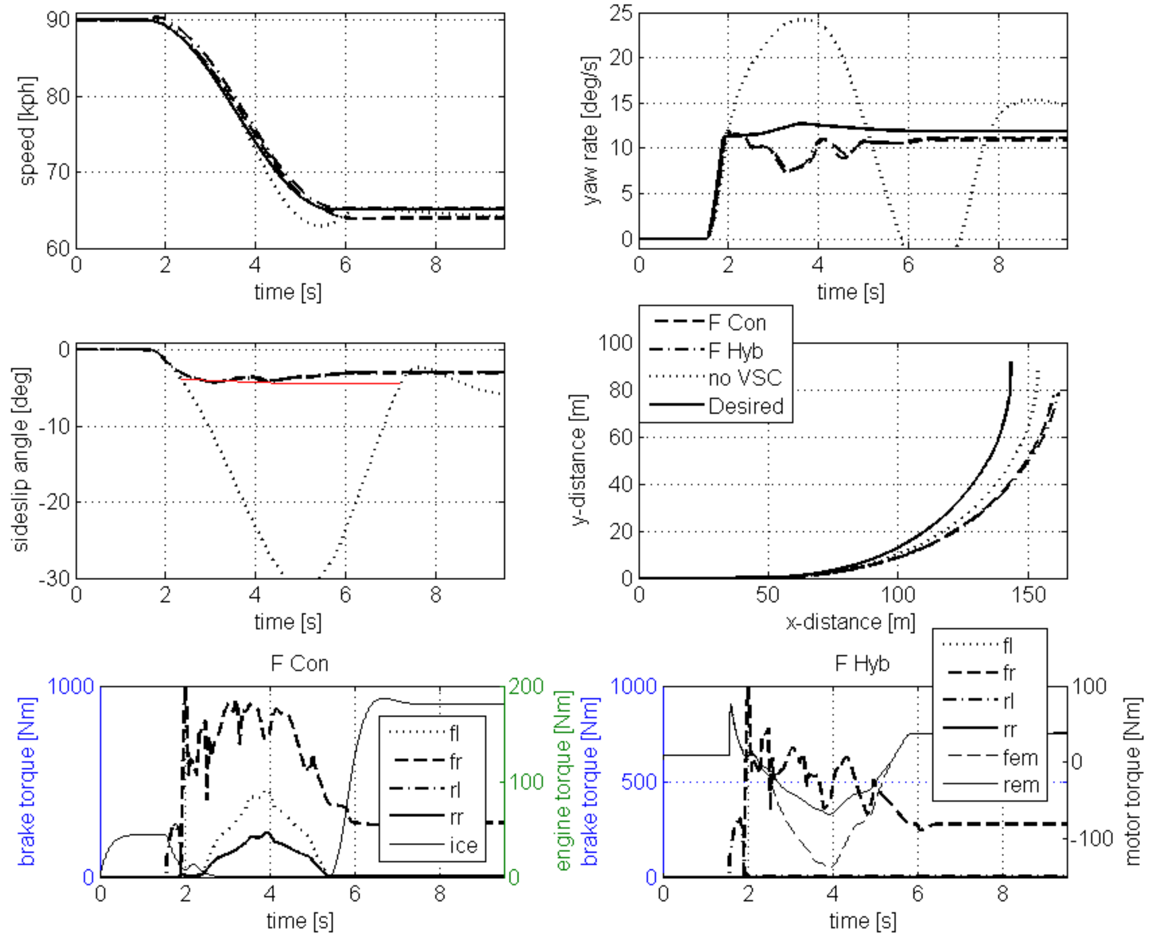

Powertrain	$(V_{x\_error})_{max}$ *[kph]*	$(V_{x\_error})_{rms}$ *[kph]*	$(r_{error})_{max}$ *[deg/s]*	$(r_{error})_{rms}$ *[deg/s]*	β_{max} *[deg]*	$(\beta_{deviation})_{max}$ *[deg]*	Consumed energy *[kJ]* *(Tractive/Battery+Brake=Total)*
Con	1.15	0.83	5.20	1.94	4.23	-	325.3+320.7=646.0
Hyb	1.70	0.90	5.08	1.95	4.28	-	41.1+182.4=223.5

(d) J-turn wet asphalt

result, F Hyb completes the lane change maneuver in 10 meters and 5 fewer meters in comparison to F Con, as seen in the dry asphalt and wet asphalt cases respectively. This is achieved without any cost in terms of VSC performance. In other words yaw tracking and sideslip angle results for both cases with and without the motors are almost identical. There is a secondary benefit in using the motors in terms of energy consumption as well, which is mainly due to the difference between the energy conversion efficiencies of the engine and the electric motors.

Similar to the lane change maneuver simulation results, for the j-turn maneuver simulation results shown in Figures 40c and 40d, it is again observed that the VSC performance, i.e. tracking the desired yaw rate and sideslip angle, does not change significantly when the electric motors are involved for supplying the tractive/braking torque. There is again a benefit of using the electric motors in terms of energy consumption, this time more significant than the benefit obtained for the lane change maneuver case, since regenerative braking is utilized with the electric motors, which reduces the load on friction brakes as well, as seen in the comparison of tabulated dissipated brake energy for Con and Hyb cases.

The simulation results can be summarized as follows:

1 No interference in the driver’s longitudinal speed demand during the lane change maneuver with the utilization of rapid torque actuation provided by the electric motors

2 Lower energy consumption during both maneuvers due to higher energy efficiency and regenerative braking capability of electric motors.

On the other hand, it is obvious that involving the electric motors through Equation 60 is not the “optimal” scenario of involving them within a VSC scheme. As a matter of fact, using the electric motors in such a way may cause excessive slip values and earlier activation of slip controllers (ABS, TCS) than intended. Figure 42 shows simulation results for the tire slip values of the vehicles controlled with F Con and F Hyb schemes during the j-turn maneuver on dry asphalt.

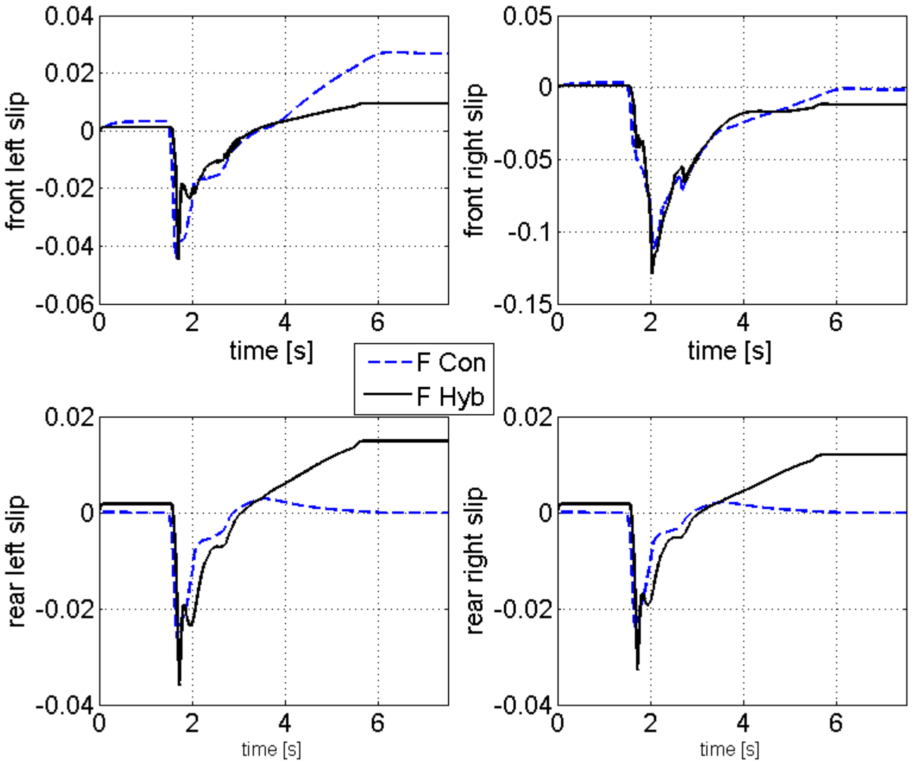

Figure 42 Tire longitudinal slip during the j-turn maneuver on dry asphalt for the stock VSC utilizing the conventional and hybrid powertrains

One can see that the front right slip reaches a minimum of 0.11 with F Con. However, it reaches a minimum of 0.13 with F Hyb. Although a stock ABS system is not modeled in this study, such increases in tire slip caused by the electric motors may trigger activation of ABS earlier than usual, as also noted in [57]. Therefore, the distribution of the control action to individual wheel brakes and electric motors should be further investigated, and this is the subject of the next Chapter.

4.3. Summary of this Chapter

1) Most of the studies that investigate VSC specifically for HEVs consider independent braking/traction at four corners, i.e. hub motors, rather than vehicle architectures having axle motors, which is more common among the hybrid electric vehicles in the market. Among the few studies that consider axle electric motors, the common approach is to disable motor braking and/or traction, or to treat it as a separate actuation combined with individual wheel braking via rule based fuzzy approaches. There is no consensus on how to best use axle electric motors within a VSC scheme.

2) (H)EVs provide an additional degree of actuation freedom, namely giving traction to wheels in addition to braking them. In such a case, using the already built-in brake actuated VSC may not be the optimal solution for yaw tracking and stability, as the motors are excluded from the VSC strategy. It is shown by simulations that involving the axle electric motors as the tractive/braking torque provider within a VSC scheme, prevents decrease in vehicle speed during the lane change maneuver. Furthermore, using

the electric motors reduces energy consumption, especially for the j-turn maneuver where regenerative braking is utilized and the load on friction braking is reduced.

3) The optimal allocation of the control action to individual wheel brakes and electric motors is an open problem. Empirical approaches such as the one expressed by Equation 60 may cause anticipated ABS/TCS activation. Therefore, there is a need for developing a control strategy that makes better use of electro-mechanical actuation, not only to remove the speed constraint, but also to enhance stability and to optimize actuator usage.

5. Integrated EHB and Axle Motor Torque Control for Vehicle Stability

This chapter presents a vehicle stability control strategy that makes explicit use of the additional actuation available in a HEV. Before introducing the controller, some important considerations within the control methodology are presented in Section 5.1. A literature survey on VSC strategies utilizing control allocation is given in Section 5.2. The proposed strategy is introduced in Section 5.3. Its performance is evaluated in comparison to the conventional stock Fuzzy controllers in Section 5.4. Finally, the proposed strategy is tested via Model-in- the-Loop (MIL) simulations in order to evaluate its performance in real time in Section 5.5.

5.1. VSC from a Control Allocation Standpoint

It is noted in Section 2.3 that the decision of "braking the inner rear wheel during understeering and the outer front wheel during oversteering" is a widely accepted principle in VSC on the basis of geometry relations and tire force characteristics. However, there may be occasions where braking a single wheel may not be sufficient to generate the required pro/contra moment required to track the desired yaw rate, whereas distributing the control action to multiple wheels offers greater freedom to generate pro/contra yaw moment. Furthermore, braking a single tire may cause the tire to saturate faster, i.e. reach the peak point of the force vs. slip curve, and activate ABS or TCS, in comparison to supplying the required moment by distributing the effort equally, as illustrated in Figure 43.

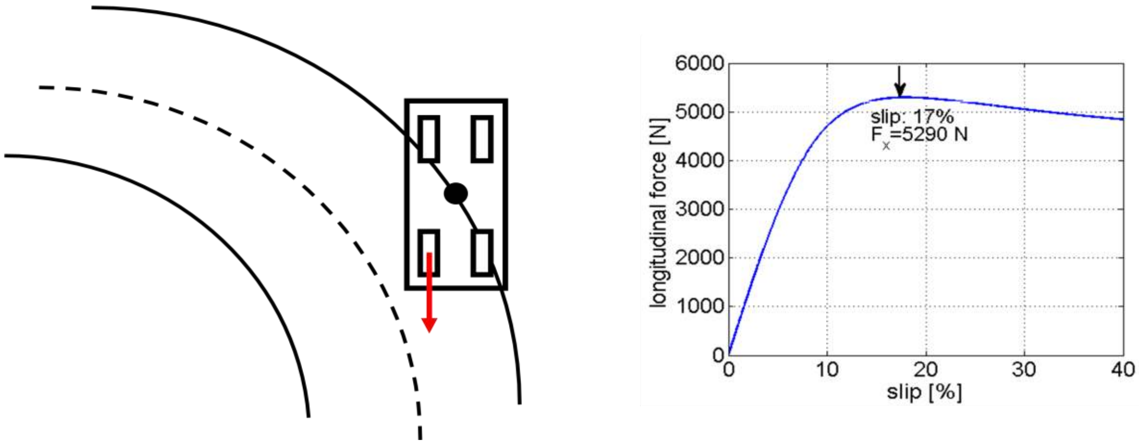

(a) Braking a single tire causing the tire to saturate and activate ABS.

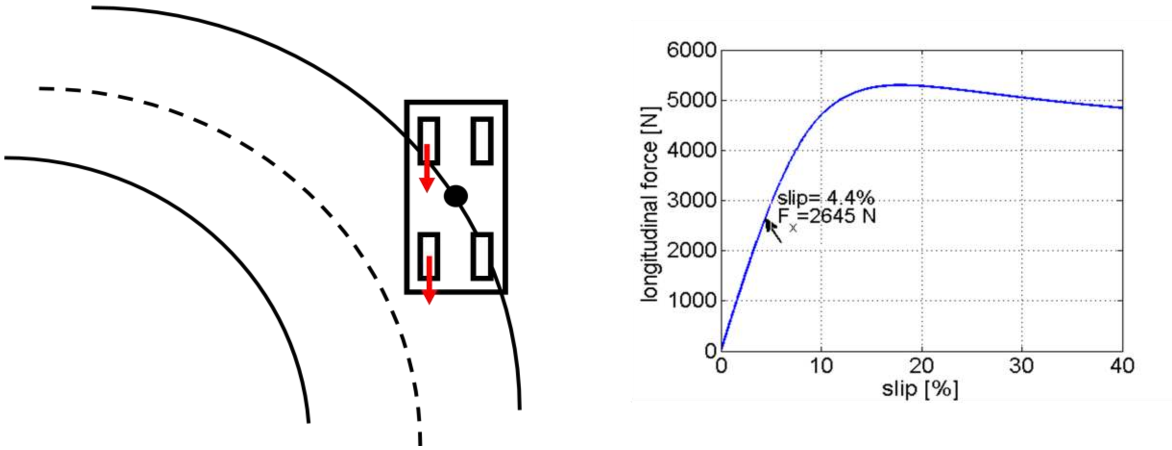

(b) Splitting the control action to two tires yielding a lower slip value for each tire.

Figure 43 Simplified illustrations of two alternative ways for getting the same corrective yaw moment

Longitudinal slip is not the only factor that affects force generation capacity of tires. Slip angle, coefficient of friction, and the normal load on the tire are other parameters that affect tire force generation, as shown in Figure 44, and should be considered as well in selecting a braking force allocation strategy, as these variables are affected by vehicle lateral and longitudinal forces to a different extent at each corner.

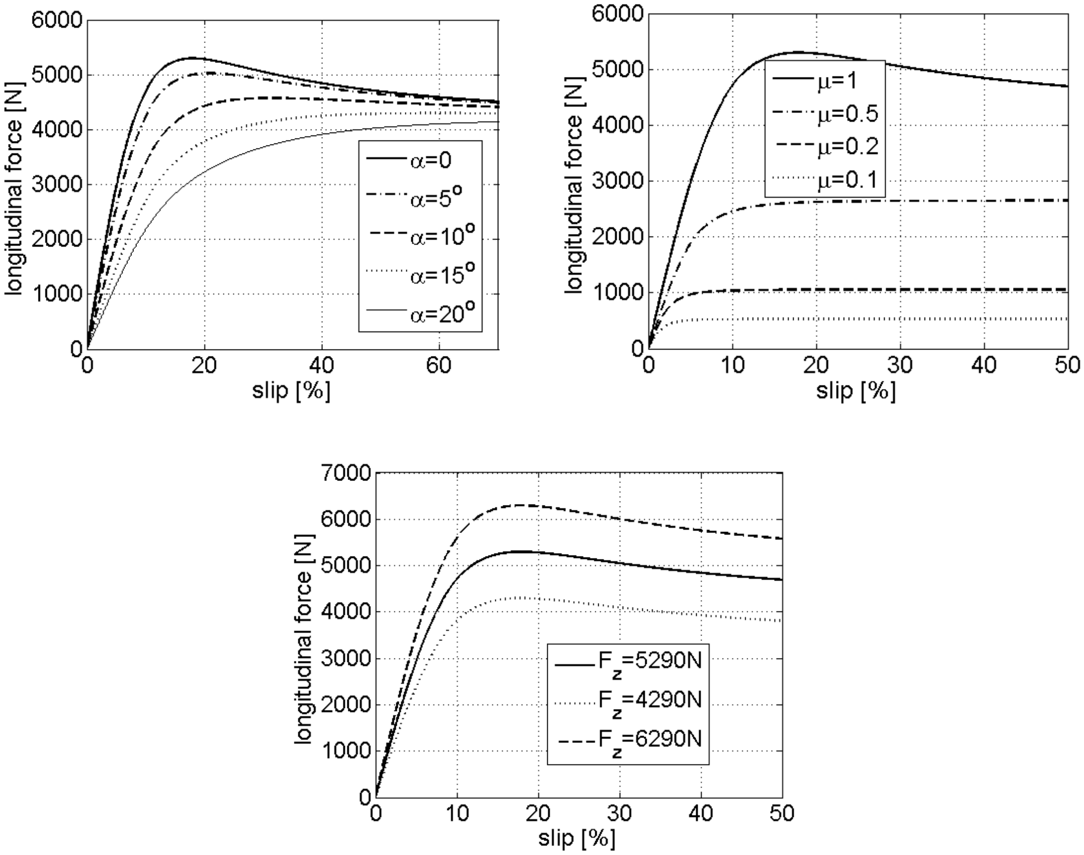

Figure 44 Tire longitudinal force with respect to slip angle, coefficient of friction and normal load on tire

In addition to this, braking only the inner rear wheel may not be the best solution in understeer condition under certain circumstances. For instance, during braking and steering as is the case for the J-turn maneuver, the normal load and therefore force generation capacity of the front tires increase as the normal load on them increase due to load transfer. In this case, braking the inner front wheel may be a better choice to create the required correcting yaw moment.

On the other hand, with the addition of the electric motors in EVs and HEVs, additional degrees of freedom become available, as the wheels can be subject to tractive as well as braking torques. In what proportion to distribute this pro/contra yaw moment action to each wheel can be formulated as an optimization problem. Considering the two control objectives, speed and yaw tracking, and the six actuators for the hybrid SUV considered in this study, namely the four wheel braking and axle motor traction/braking, the system can be characterized as an over-actuated system. With this high actuation level, the VSC problem turns into tire force/torque distribution problem. Control allocation for an over actuated VSC system is the principal subject of the present chapter.

5.2. Literature on VSC Strategies from a Control Allocation Standpoint

Control allocation has been studied in the aerospace literature. Ground vehicle stability control has also been the subject of control allocation methods [10, 22, 23, 25, 59, 60]. Most of them use static quadratic programming based control allocation methods [17, 22, 23, 59, 60] since the actuator (electric motor and brake system) dynamics are faster than the vehicle dynamics.

Zheng [10] applies the LQR method to find the optimal set of slip values for each wheel, where the cost function is a weighted sum of yaw rate and sideslip angle error.

Mokhiamar [22] applies a sliding mode controller for yaw and lateral velocity, and after the desired lateral force and yaw moment are determined, the control effort is distributed to eight forces, namely 4 longitudinal and 4 lateral forces associated with each wheel, considering a vehicle architecture where all four wheels can be individually braked/driven and steered. The interesting aspect of this study is the cost function, a weighted sum of the absolute normalized forces. With eight control variables and three constraints, namely desired moment and lateral force from the previous stage, and longitudinal force as a function of accelerator/brake pedal pressure command from the driver, a new objective function is derived with five independent variables, which is subject to a simple unconstrained multivariable optimization.

Fredriksson [59] applies a decoupling feedback linearization to find the desired longitudinal and lateral forces and the yaw moment, and uses a linear control allocation method to distribute the individual wheel forces. Two different hybrid architectures are considered, one with all four wheels individually braked/driven and steered, and the other with all wheels individually braked and front ones individually driven. Simulation results show that the latter exhibits worse results since the lateral forces are not directly controlled.

Plumlee [60] applies quadratic programming with inequality constraints used for the peak values of slip and slip angle, to a differential braking vehicle model. A control method called “Sign Preserving Quadratic Programming” [61] is applied in this study, such that in case the optimal solution lies outside of the constraints, the cost function is relaxed and the constraints are redefined for individual scaling of the components of the actuation vector. This separate scaling maintains feasibility while preserving the sign of the total actuation vector. Simulation results show that although this method performs well for yaw rate tracking, it fails to keep the sideslip angle within an acceptable range.

An overview of different control allocation methods and a comparison of different algorithms in terms of the floating point operations (flop) for solving the quadratic optimization problem is given in [23, 62]. Among the algorithms reviewed, fixed point method [60] is proven to result in the lowest computational burden in converging to the optimal solution. This is shown both theoretically and by simulation results. Fixed point method is used in this study as well, to distribute the corrective longitudinal force and yaw moment to longitudinal wheel slip ratios, which is applied in Section 5.3.3.

5.3. Integrated EHB and axle motor torque control for VSC

The overall scheme of the proposed controller is shown in Figure 45, along with the inputs to it coming from the vehicle dynamics and driver models. The inputs to the controller are: measured yaw rate, wheel speeds, lateral and longitudinal accelerations that come from the vehicle dynamics model, and accelerator, and brake pedal and steering wheel input from the driver. The outputs of the controller are motor and brake torque commands. Each component of the controller is explained next.

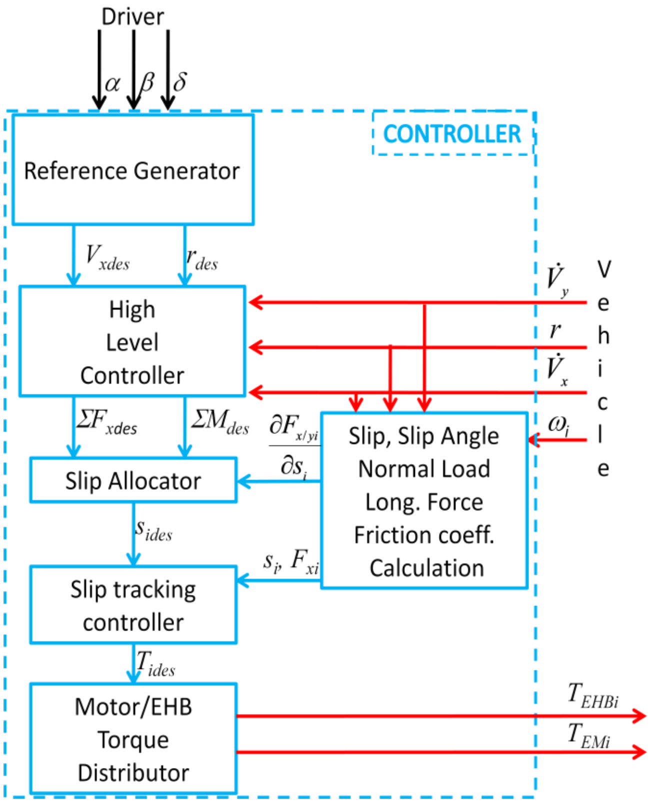

Figure 45 Overall structure of the proposed VSC.

5.3.1. Reference Generator

Figure 45 shows a reference generator block, responsible for generating the desired longitudinal speed and yaw rate that the controller is intended to track. The desired longitudinal speed can be expressed as

$$V_{xdes} = V_{x0} + \int \frac{F_{dest} - F_{desb}}{M} dt \qquad (63)$$

where V_{x0} is the initial velocity and F_{dest} and F_{desb} are the desired longitudinal tractive and braking force as a function of accelerator/brake pedal positions, respectively, as shown in Figure 46. It is typical that drivers prefer to have a low level of braking force sensitivity during the first part of the pedal stroke and a proportionally greater increment of the braking force in the last part of the pedal stroke (abrupt braking).

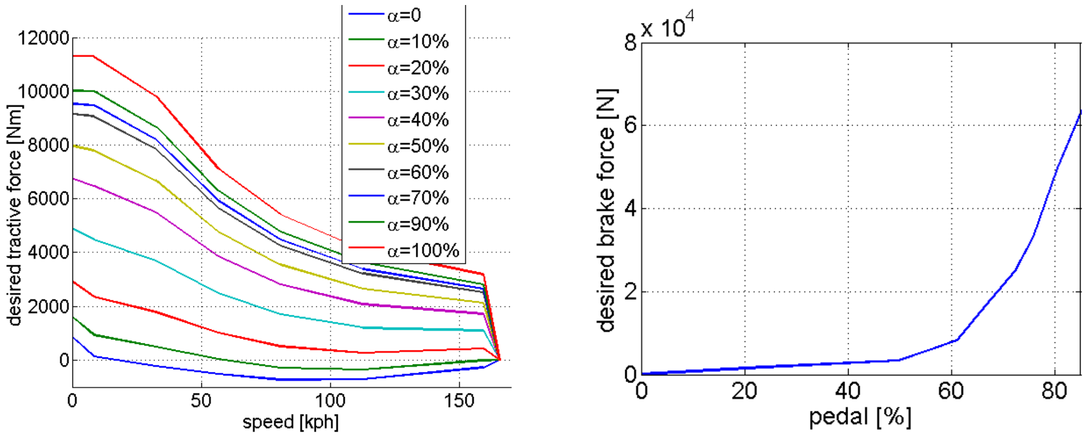

(a) Desired tractive force as a function of vehicle speed and accelerator pedal

(b) Desired braking force as a function of brake pedal

Figure 46 Desired forces

The desired yaw rate is generated using the bicycle model as described in Section 2.2. Specifically it is given by the expression in Equation 4 saturated by $g\mu/V_x$ derived from the steady state cornering conditions.

5.3.2. High Level Controller

The inputs to the high level controller are actual and desired longitudinal speed and yaw rate, respectively. The outputs are the desired net longitudinal force and yaw moment, as shown in Figure 47.

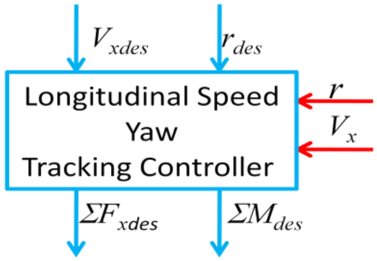

Figure 47 High level controller

The equation of motion for longitudinal dynamics of the vehicle model was given by Equations 41 and 42. They can be combined to express the longitudinal dynamics as shown in (64):

$$\dot{V}_x = V_y r - \frac{\rho C_D A_f}{M} V_x^2 - \frac{M_s h_s}{M} rp + \frac{\sum F_x}{M} + w_x \tag{64}$$

where w_x represents the disturbance and unmodeled dynamics in longitudinal direction, and ΣF_x is the sum of all tire forces in longitudinal direction and can be treated as the input. Due to the presence of non-linear terms, sliding-mode control is the design method chosen to stabilize the closed loop system. The sliding surface is selected as

$$S = c\left(V_x - V_{xdes}\right) + d\int\left(V_x - V_{xdes}\right)dt \tag{65}$$

where c and d are positive constants. The Lyapunov function can be written as

$$V = \frac{1}{2}S^2 \tag{66}$$

with the results that

$$\dot{V} = S\dot{S} = S\left(cV_y r - \frac{c\rho C_D A_f}{M} V_x^2 - c\frac{M_s h_s}{M} rp + \frac{c\sum F_x}{M} + cw_x - c\dot{V}_{xdes} + de \right) \tag{67}$$

where $e=V_x-V_{xdes}$ is the velocity tracking error.

The control law that assigns the total longitudinal force is:

$$\sum F_x = -\frac{M_0}{c} Ksign\left(S\right) \tag{68}$$

where M_0 is the nominal mass (average of unloaded and fully loaded vehicle mass). With the right hand side of Equation 68 substituted for ΣF_x in Equation (67), we obtain

$$\dot{V} = S\left(cV_y r - \frac{c\rho C_D A_f}{M} V_x^2 - c\frac{M_s h_s}{M} rp - K\frac{M_0}{M} sign\left(S\right) + cw_x - c\dot{V}_{des} + de \right) \tag{69}$$

Following the approach used in [62], one can show the closed loop system is stable as follows:

$$\dot{V} = Ssign\left(S\right)\begin{pmatrix} sign\left(S\right)cV_y r - sign\left(S\right)\frac{c\rho C_D A_f}{M} V_x^2 - sign\left(S\right)\frac{ch_s M_s}{M} rp \\ -K\frac{M_0}{M} + sign\left(S\right)cw_x - sign\left(S\right)c\dot{V}_{des} + sign\left(S\right)de \end{pmatrix} \tag{70}$$

and

$$\dot{V} \le \left|S\right|\left(c\left|V_y r\right| + \frac{c\rho C_D A_f}{M} V_x^2 + \frac{ch_s M_s}{M}\left|rp\right| - K\frac{M_0}{M} + c\left|w_x\right| + c\left|\dot{V}_{xdes}\right| + d\left|e\right| \right) \tag{71}$$

The condition for attractivity of the sliding surface can be expressed as

$$\dot{V} \le -k\left|S\right| \tag{72}$$

where k is a positive constant. Equation 71 and Equation 72 guarantee that if

$$c\left|V_y r\right| + \frac{c\rho C_D A_f}{M} V_x^2 + \frac{ch_s M_s}{M}\left|rp\right| - K\frac{M_0}{M} + c\left|w_x\right| + c\left|\dot{V}_{des}\right| + d\left|e\right| \le -k \tag{73}$$

or similarly

$$K \ge c\frac{M}{M_0}\left|V_y r\right| + \frac{c\rho C_D A_f}{M_0} V_x^2 + \frac{ch_s M_s}{M_0}\left|rp\right| + c\frac{M}{M_0}\left|w_x\right| + c\frac{M}{M_0}\left|\dot{V}_{xdes}\right| + d\frac{M}{M_0}\left|e\right| + k\frac{M}{M_0} \tag{74}$$

then the attractivity of the surface is satisfied. Picking the controller gain K as

$$K = c\left(2V_{y\max} r_{\max} + \frac{\rho C_D A_f}{M_0} V_{x\max}^2 + 1 + 2w_{x\max} + g\right) + 2de_{\max} + 2k \tag{75}$$

along with Equation 68 yields the control law. Note that constants in Equation 75 such as V_{ymax}, r_{max}, V_{xmax} and w_{xmax} are all maximum physical limits associated with vehicle motion. For instance V_{xmax} is the maximum vehicle speed 180 kph. The constant k is the tuning parameter that establishes the convergence rate of the sliding surface.

The yaw motion equation was given by Equation 49. Following the same approach as above, the control law is chosen as:

$$\sum M = -\frac{I_{zz0}}{c} K sign\left(\Sigma\right) \tag{76}$$

where

$$S = c\left(r - r_{des}\right) + d\int\left(r - r_{des}\right)dt \tag{77}$$

With the Lyapunov function

$$V = \frac{1}{2}S^2 \tag{78}$$

and its gradient

$$\dot{V} = Ssign\left(S\right)\left(-\frac{I_{zz0}}{I_{zz}}K + csign\left(S\right)w_z - csign\left(S\right)\dot{r}_{des} + sign\left(S\right)de\right) \tag{79}$$

For attractivity of the surface, one must choose *K* such that

$$K \geq c\frac{I_{zz}}{I_{zz0}}\left|\dot{r}_{des}\right| + c\frac{I_{zz}}{I_{zz0}}\left|w_z\right| + d\frac{I_{zz}}{I_{zz0}}\left|e\right| + \frac{I_{zz}}{I_{zz0}}k \tag{80}$$

so the control gain *K* is selected to be

$$K = 2\left(c\left(\dot{r}_{des\max} + w_{z\max}\right) + de_{\max} + k\right) \tag{81}$$

With the selection of K, the design of the yaw moment controller is complete.

To avoid chattering for the control laws for both longitudinal speed and yaw rate, the sign function can be replaced by a saturation function [64]. The saturation function is given as:

$$sat\left(\frac{S}{\Phi}\right) = \left\{\begin{matrix} 1 & for & S \geq \Phi \\ \frac{S}{\Phi} & for & -\Phi < S < \Phi \\ -1 & for & \mathrm{S} \leq -\Phi \end{matrix}\right\} \tag{82}$$

So the final expression for the control laws can be written as:

$$\begin{aligned} \sum F_x = & \left[-M_0\left(2V_{y\max}r_{\max} + 2w_{x\max}1 + g\right) - \rho C_D A_f V_{x\max}^2 - \frac{2M_0}{c}\left(de_{\max} + k\right)\right] \\ & sat\left[c\left(V_x - V_{xdes}\right) + d\int\left(V_x - V_{xdes}\right)dt\right] \end{aligned} \tag{83}$$

and

$$\sum M = -2I_{zz0}\left(\dot{r}_{des\max} + w_{z\max} + \frac{1}{c}\left(de_{\max} + k\right)\right) sat\left[c\left(r - r_{des}\right) + d\int\left(r - r_{des}\right)dt\right] \tag{84}$$

Note that the total lateral force, i.e. ΣF_y is not treated as a control input since the high level control objective is to track desired longitudinal speed and yaw rate. However, as mentioned in Section 2.2, another control objective is to keep the sideslip angle within bounds specified by Equation 7. The reader may recall that simulation results in Section 2.4 show that there may be a trade-off between yaw rate and sideslip angle. In other words, tracking the desired yaw rate very accurately may cause high values of sideslip angle that exceeds the limit specified by Equation 7. To avoid such a phenomenon, the following strategy is applied in the proposed controller: As long as the sideslip angle is lower than the threshold, yaw rate and speed are tracked as accurately as possible. If sideslip angle exceeds the threshold, then the understeer coefficient that specifies the desired yaw rate as given in Equation 4 is increased with the prior knowledge that reducing the yaw rate would reduce the sideslip angle as well. The outcome of this correction will be shown by simulation results in Section 5.4.

5.3.3. Control Allocation

An important point that should be taken into account in the control allocation scheme is the decision of the variables to which the control action should be allocated. There are usually two approaches in literature, namely, allocation to individual tire forces (or torque) [22, 59, 60], and allocation to individual wheel slips [10, 22, 25]. It is explained in [61] that the former approach may yield unstable slip values exceeding the peak point of the force vs. slip curve, as shown in Figure 48.

On the other hand, the latter approach, i.e. allocation to wheel slips, provides the freedom of adding constraints to wheel slip values within the control allocation scheme so that they do not exceed the peak point of the curve, which simplifies the problem. Furthermore, if the control objective is not only tracking the desired yaw rate, but also the desired longitudinal vehicle speed, as is the case in this dissertation, then the desired slip values generated by the control allocation will be the optimal slip values, not only in terms of yawing, but also in terms of traction/braking performance of the vehicle. In other words, the control allocator serves as an anti-lock brake/traction controller as well as VSC since it generates the optimal slip values for both. Due to these advantages, individual wheel slips are chosen as the allocation variables. As a result, the objective of control allocation can be formulated in terms of

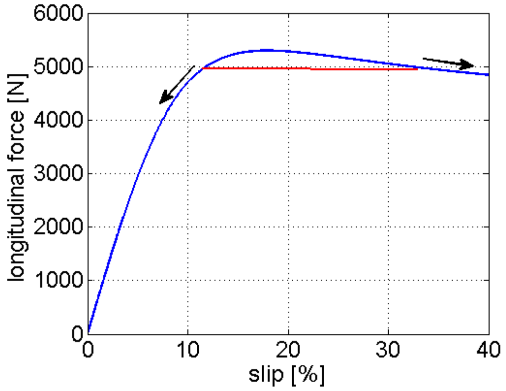

Figure 48 5000 N longitudinal force corresponds to both 11% and 33 % slip. The arrows show the direction of reducing force.

$$v = \begin{Bmatrix} \Sigma F_x \\ \Sigma M \end{Bmatrix} \tag{85}$$

$$u = \begin{Bmatrix} s_{fl} \\ s_{fr} \\ s_{rl} \\ s_{rr} \end{Bmatrix} \tag{86}$$

where v is the output of the high level controller, i.e. desired net longitudinal force and yaw moment that will be allocated to u, the vector of individual wheel slips. The generic quadratic optimization problem can now be formulated:

$$J = \arg\min_{x} \ \frac{1}{2} x^T Q x + c^T x \tag{87}$$

subject to equality or inequality constraints such as

$$Ax<b \tag{88}$$

$$Ex=d \tag{89}$$

To complete the formulation of the quadratic optimization problem as in Equation 87, the control effectiveness matrix B is defined as

$$B = \frac{\partial v}{\partial u} = \begin{Bmatrix} \dfrac{\partial \sum F_x}{\partial u} \\ \dfrac{\partial \sum M}{\partial u} \end{Bmatrix} \tag{90}$$

and the optimization problem can be stated as

$$J = \arg\min_{U} = \frac{1}{2}\left(Bu - v\right)^T W_v \left(Bu - v\right) + \frac{1}{2} U^T W_u U \tag{91}$$

Subject to

$$\left|u\right| \le u_{thr}(\mu, \alpha) \tag{92}$$

The problem can be stated in words as: Given the control input v (that comes from the high level controller), find the slip vector u that minimizes the cost function given by Equation 91, satisfying the constraint given by Equation 92. The control effectiveness matrix can be derived using Equation 42 and Equation 49 as

$$B = \left\{ \begin{array}{cc} \frac{\partial F_{xfl}}{\partial s_{fl}}\cos(\delta) - \frac{\partial F_{yfl}}{\partial s_{fl}}\sin(\delta) & a\frac{\partial F_{xfl}}{\partial s_{fl}}\sin(\delta) + \frac{t}{2}\frac{\partial F_{xfl}}{\partial s_{fl}}\cos(\delta) + a\frac{\partial F_{yfl}}{\partial s_{fl}}\cos(\delta) - \frac{t}{2}\frac{\partial F_{yfl}}{\partial s_{fl}}\sin(\delta) \\ \frac{\partial F_{xfr}}{\partial s_{fr}}\cos(\delta) - \frac{\partial F_{yfr}}{\partial s_{fr}}\sin(\delta) & a\frac{\partial F_{xfr}}{\partial s_{fr}}\sin(\delta) - \frac{t}{2}\frac{\partial F_{xfr}}{\partial s_{fr}}\cos(\delta) + a\frac{\partial F_{yfr}}{\partial s_{fr}}\cos(\delta) + \frac{t}{2}\frac{\partial F_{yfr}}{\partial s_{fr}}\sin(\delta) \\ \frac{\partial F_{xrl}}{\partial s_{rl}} & -b\frac{\partial F_{yrl}}{\partial s_{rl}} + \frac{t}{2}\frac{\partial F_{xrl}}{\partial s_{rl}} \\ \frac{\partial F_{xrr}}{\partial s_{rr}} & -b\frac{\partial F_{yrr}}{\partial s_{rr}} - \frac{t}{2}\frac{\partial F_{xrr}}{\partial s_{rr}} \end{array} \right\}^{T} \qquad (93)$$

Using the tire model equations, namely Equation 30 and Equation 31, the variation of longitudinal and lateral force with respect to slip, can be obtained analytically. The expressions for $\partial F_{xi}/\partial s_i$ and $\partial F_{yi}/\partial s_i$ are given in *Appendix C*. Note that these variations of forces with respect to slip are also functions of slip, slip angle, normal load, and friction coefficient, just like the forces themselves. Therefore, the control allocation block takes those variables as inputs in addition to net longitudinal force and yaw moment, as shown in Figure 49.

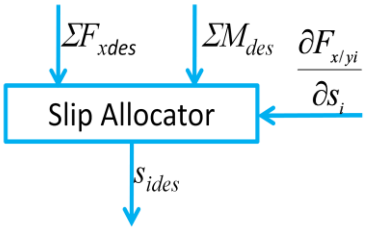

Figure 49 Control allocator

The weighting matrices for optimization error and energy can be written as

$$W_v = \begin{bmatrix} w_{v1} & 0 \\ 0 & w_{v2} \end{bmatrix} \tag{94}$$

$$W_u = \begin{bmatrix} w_{u1} & 0 & 0 & 0 \\ 0 & w_{u2} & 0 & 0 \\ 0 & 0 & w_{u3} & 0 \\ 0 & 0 & 0 & w_{u4} \end{bmatrix} \tag{95}$$

The selection is done such that $w_{v1} << w_{v2}$ since the high priority control objective is to track the desired yaw rate.

Note that the inequality constraints as given by Equation 92 correspond to the peak point of the longitudinal force versus slip curve. In other words, the control allocation dictates that the system stays in the stable region of the force vs. slip curve. However, it is important to note that this peak point is not only a function of slip, but also it changes with respect to slip angle and coefficient of friction due to tire characteristics as shown in Figure 50. Therefore the inequality constraint of the optimization varies accordingly.

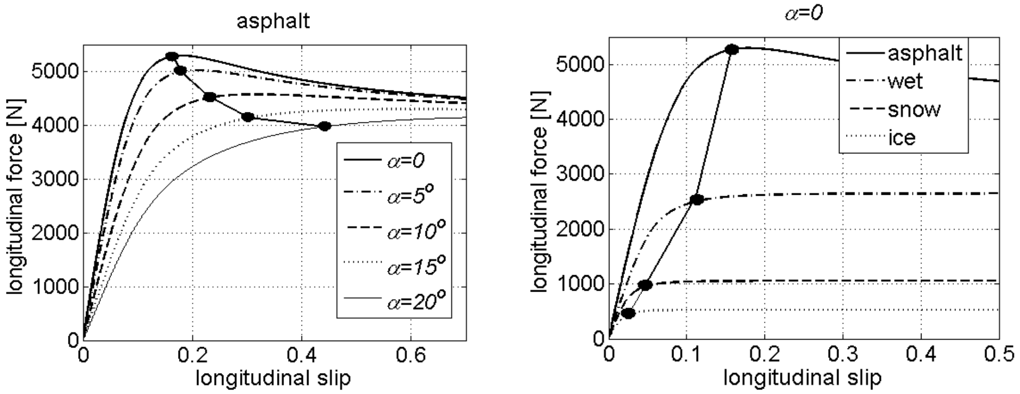

(a) Force vs. slip for different slip angles

(b) Force vs. slip for different friction coefficients

Figure 50 Change of the threshold in inequality constraints depending on different variables

Another important consideration in regard to the control allocation is the computational effort required to solve the optimization problem. This becomes a critical factor in real time implementation due to limited computational resources offered by VSC processors in vehicles. There are various algorithms for solving the optimization problem stated by Equation 91 and Equation 92. A detailed comparison of different algorithms for solving this quadratic optimization problem can be found in [62]. It is shown in that study that “fixed-point method” as explained in [62, 63], yields the lowest number of flops per iteration in comparison to two other algorithms. This method is also used in this dissertation study. The code for the iteration implemented within an Embedded Matlab Function in Simulink can be found in *Appendix D*.

5.3.4. Slip tracking controller

The objective of the slip tracking controller is to generate the net torque T_{ides} for each wheel that would track the reference slip values generated by the control allocation.

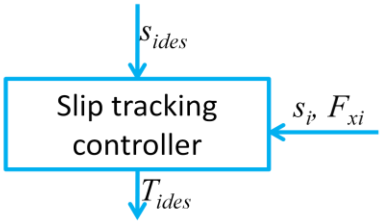

Figure 51 Slip tracking controller

Different control approaches for wheel slip control can be found in literature, such as Lyapunov based solutions [25, 65-67], sliding mode controllers [10, 22, 68] and PID controllers [69]. A sliding mode controller is used in this study which is suitable for direct wheel slip regulation to track the dynamic reference slip. Slip dynamics can be derived by combining Equation 29 and Equation 36:

$$\dot{s}_i = -\frac{r_w^2 F_{xi}}{I_w V_i} - \frac{\dot{V}_i}{V_i} s_i - \frac{\dot{V}_i}{V_i} + \frac{r_w}{I_w V_i} T_i \tag{96}$$

where r_w is the rolling radius of the tire, I_w is the rotational mass moment inertia of the wheel, V_i is the velocity component across wheel plane, and T_i is the net torque at wheel level, treated as the control input. Defining the sliding surface as

$$S = c\left(s - s_{des}\right) + d\int\left(s - s_{des}\right)dt \tag{97}$$

where c and d are positive constants, the Lyapunov function can be written as

$$V = \frac{1}{2} S^2 \tag{98}$$

$$\dot{V} = S\dot{S} = \Sigma\left(-\frac{c r_w^2 F_{xi}}{I_w V_i} - \frac{c\dot{V}_i}{V_i} s_i - \frac{c\dot{V}_i}{V_i} + \frac{c r_w}{I_w V_i} T_i - c\dot{s}_{des} + de \right) \tag{99}$$

where $e = s - s_{des}$.

Assigning the control law as

$$T_i = -\frac{I_w K}{r_w c} sign\left(S\right) \tag{100}$$

yields

$$\begin{aligned}\dot{V} &= S\left(-\frac{cr_w^2 F_{xi}}{I_w V_i} - \frac{c\dot{V}\left(s_i+1\right)}{V_i} - \frac{K}{V_i} sign\left(S\right) - c\dot{s}_{des} + de \right) \\ &= Ssign\left(S\right)\left(-\frac{cr_w^2 F_{xi}}{I_w V_i} sign\left(S\right) - \frac{c\dot{V}\left(s_i+1\right)}{V_i} sign\left(S\right) - \frac{K}{V_i} - c\dot{s}_{des} sign\left(S\right) + design\left(S\right) \right)\end{aligned} \tag{101}$$

Therefore the following inequality can be written

$$\dot{V} \leq \left|\Sigma\right| \left(\frac{cr_w^2}{I_w V_i}\left|F_{xi}\right| + \frac{c\left(s_i+1\right)}{V_i}\left|\dot{V}\right| - \frac{K}{V_i} + c\left|\dot{s}_{des}\right| + d\left|e\right| \right) \tag{102}$$

The condition for attractivity of the sliding surface can be expressed as

$$\dot{V} \leq -k\left|S\right| \tag{103}$$

where *k* is a positive constant. Equation 102 and Equation 103 guarantee that if

$$\frac{cr_w^2}{I_w V_i}\left|F_{xi}\right| + \frac{c\left(s_i+1\right)}{V_i}\left|\dot{V}\right| - \frac{K}{V_i} + c\left|\dot{s}_{des}\right| + d\left|e\right| \leq -k \tag{104}$$

or similarly

$$K \geq \frac{cr_w^2}{I_w}\left|F_{xi}\right| + c\left(s_i+1\right)\left|\dot{V}_i\right| + kV_i + cV_i\left|\dot{s}_{des}\right| + dV_i\left|e\right| \tag{105}$$

then the attractivity of the surface is satisfied. The controller gain *K* is chosen to be:

$$K = \frac{cr_w^2}{I_w}F_{xi\max} + 2cg + V_{i\max}\left(k + cr + 2d\right) \tag{106}$$

where F_{ximax} is the maximum longitudinal force that a single tire can generate (considering a coefficient of adhesion of 1 and the entire vehicle load is on that single tire), V_{imax} is the maximum speed across wheel plane (which is around the maximum speed of the vehicle), and r is the maximum rate of change of the desired slip value as constrained by the electric motor actuation rate. Like the sliding mode controller used for the high level controller, a saturation function replaces the sign function to avoid chattering.

$$sat\left(\frac{S}{\Phi}\right)=\begin{Bmatrix} 1 \quad for \quad \mathrm{S}\geq\Phi \\ \dfrac{\Sigma}{\Phi} \; for \quad \text{-}\Phi<S<\Phi \\ \text{-1} \; for \quad \mathrm{S}\leq\text{-}\Phi \end{Bmatrix} \tag{107}$$

finally the expression for the control law can be written as:

$$T_i=\left[-r_wF_{xi\max}-2\frac{I_w}{r_w}g-\frac{I_w}{r_w}V_{i\max}\left(\frac{k}{c}k+r+2\frac{d}{c}\right)\right]sat\left[c\left(s-s_{des}\right)+d\int\left(s-s_{des}\right)dt\right] \tag{108}$$

With this control law, the performance of the slip tracking controller is shown in Figure 52a for the lane change maneuver simulation on dry asphalt. Note that this controller relies on the information of the desired and the actual slip only, and treats the force term in Equation 96 as a disturbance. With the estimation of longitudinal forces as explained in Section 3.2.5, the controller performance can be enhanced by including the force eliminating feedback term in the control as:

$$T_i=-\frac{I_wK}{r_wc}sign\left(S\right)+r_wF_{xi} \tag{109}$$

and a relaxed control gain would be sufficient for achieving the attractivity of the sliding surface:

$$K=2cg+V_{i\max}\left(k+cr+2d\right) \tag{110}$$

The performance of this enhanced control law expressed by

$$T_i = -\frac{I_w\left[2cg + V_{i\max}\left(k + cr + 2d\right)\right]}{r_w c} sat\left(S\right) + r_w F_{xi} \tag{111}$$

is shown in Figure 52b.

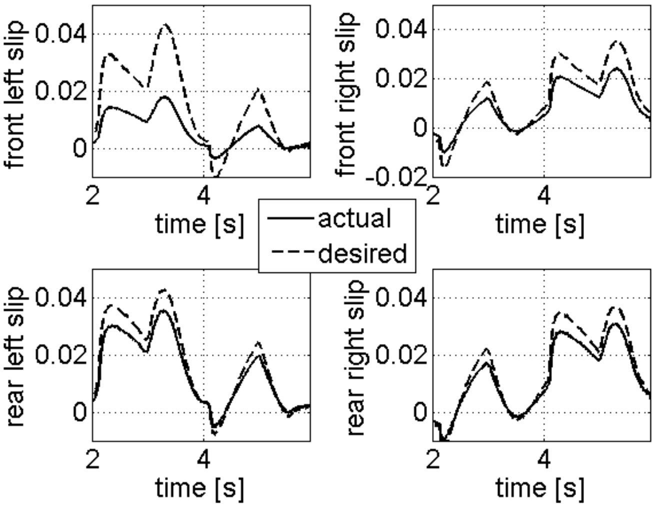

(a) Sliding mode controller

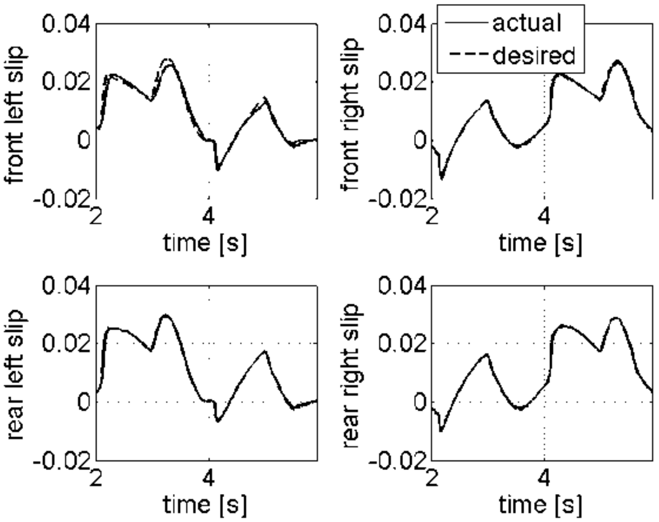

(b) Sliding mode controller with force compensation

Figure 52 Desired and actual slip values during the lane change maneuver simulation

5.3.5. Motor/EHB Torque Distributor

The last part of the controller is the motor/EHB torque distributor.

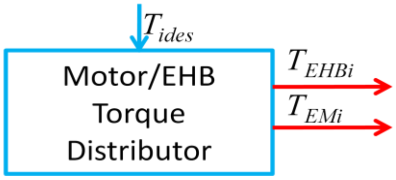

Figure 53 Motor/brake torque distributor

The net torque at the wheel demanded by the slip tracking controller is supplied from two sources: Electric motors and EHB system. As evident from Figure 51, the net torque generated by the slip tracking controller may have different signs on each side of an axle, i.e. the controller may dictate a positive torque on left wheel and a negative torque on the right one, and vice versa, occasionally. For such cases, the controller needs to distribute the net torque on each wheel to the axle motor torque and EHB torque on both sides. Equations 112 to 114 show how the control strategy commands motor and brake torque with the knowledge of net torque required at each wheel level.

$$T_{EM} = \frac{2T_{ihigh}}{i_{em}\eta\left(T_{EM}, \omega_{EM}\right)} \tag{112}$$

$$T_{bhigh} = 0 \tag{113}$$

$$T_{blow} = T_{ihigh} - T_{ilow} \tag{114}$$

where T_{ihigh} is the net torque request for the wheel with a higher demand (magnitude wise), i_{em} is the gear reduction ratio of the axle motor, T_{EM} is the torque request sent to the motor, η is the combined efficiency of the powertrain between the motor and the wheel as a function of motor speed and torque, T_{bhigh} is the brake torque request corresponding to that wheel with the higher (magnitude wise) torque request, and T_{blow} is the brake torque request for the other wheel on that axle. This logic can be interpreted in words as: Supply torque to the wheel that needs more torque (magnitude wise), with the electric motor, and for the remaining wheel on the same axle, subtract the excessive torque by friction braking.

Once the split decision is made, the desired torque request is commanded to the electric motors and the electro-hydraulic friction brakes. The rate of change of the torque commands are limited prior to feeding them into the powertrain model, to prevent chattering issues, since the dynamics of the motors and the EHB system are different. Therefore the torque commands are limited by rate of the slower actuator, i.e. the motors. The net torque as a combination of electric motor torque and EHB torque during the J-turn maneuver is shown in Figure 54.

5.4. Evaluation of the proposed VSC

In this section, the proposed strategy is compared to the Fuzzy VSC scheme described in Section 2.3, which mirrors current industry practice. The same maneuvers are simulated for the hybrid SUV model described in the previous Chapter, controlled by the proposed VSC. F Hyb is replaced by the proposed controller in order to compare the “stock” VSC utilizing the conventional powertrain with the proposed one involving the electric motors and the new control allocation policy.

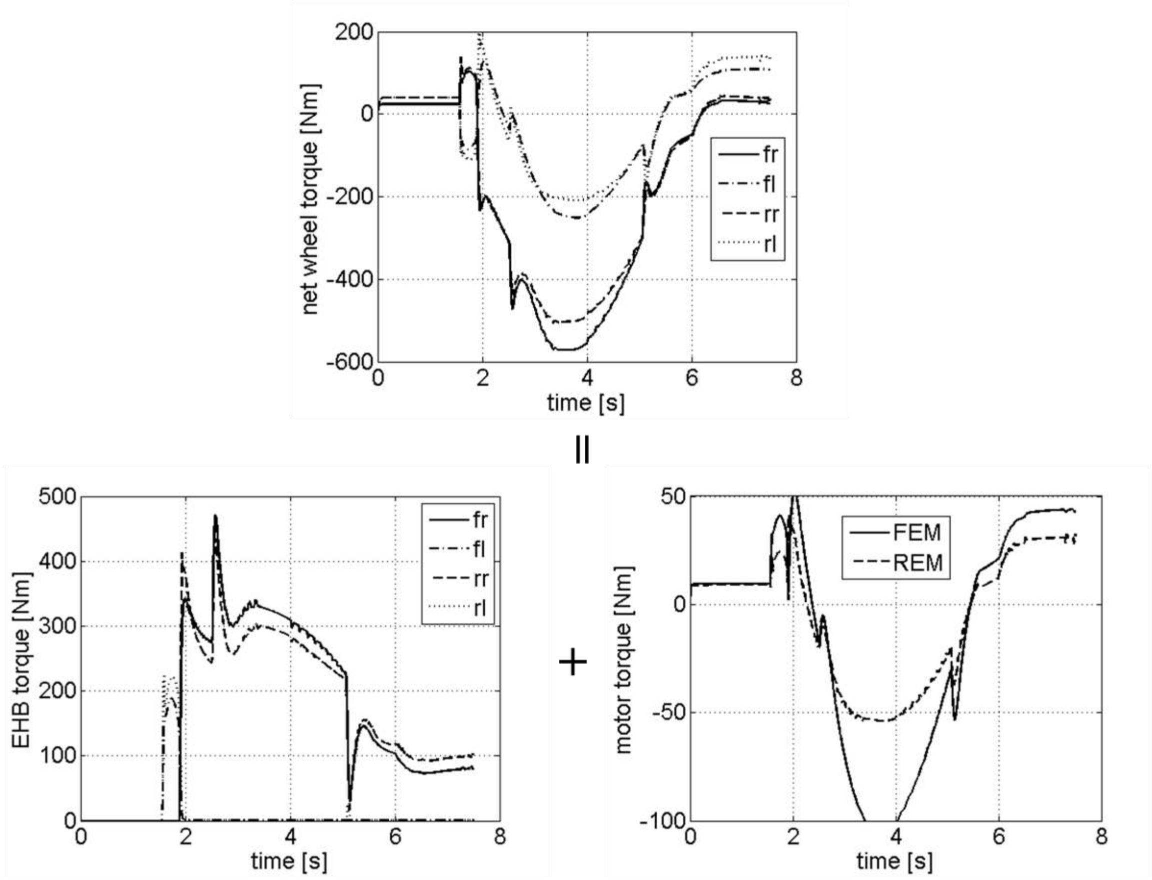

Figure 54 Components of the net torque at wheel level are EHB torque and electric motor torque

Simulation results are shown in Figures 55 through 58. The longitudinal speed, sideslip angle, yaw velocity, and the vehicle trajectory are shown at the top of each figure, for the stock Fuzzy controller and the proposed VSC, together with the desired values for speed and yaw rate. For the sideslip angle, the limit specified by Equation 7 is also shown (in case it is exceeded) on the plot. In the bottom third of the figure, the brake and motor torque profiles for the vehicle controlled with the proposed VSC during the maneuver are shown. Tables showing maximum and root mean square (RMS) of the deviation of yaw rate and speed from the desired values, maximum sideslip angle and deviation from the allowed sideslip angle limit, and the net energy consumption while VSC is active, are also given. Simulation results for net torque, normal load, and desired (as dictated by the control allocation) and actual slip when VSC is active for each wheel, are also shown.

The main observation from the lane change maneuver simulation results in Figure 55 and Figure 56 that compare the proposed and the stock VSC, is that the involvement of the electric motors within the proposed scheme to provide tractive torque prevents the decrease in vehicle speed in comparison to the vehicles controlled by the stock VSC, without any cost in desired yaw tracking and sideslip angle limitation. Furthermore there is a benefit of using the motors in terms of energy consumption as well, as also noted in Section 4.2, mainly due to the difference between the energy conversion efficiencies of the engine and the electric motors.

It is observed from the net wheel torque profiles of Figures 55b and 56b that both front and rear inner (left) wheels are accelerated, and that both outer (right) wheels are braked, almost equally, to prevent oversteering. For the dry asphalt case, the net wheel torque becomes negative for a shorter period in comparison to the wet asphalt case. The reason is that more tractive torque is required for the dry asphalt case in comparison to the wet asphalt case in order to achieve the desired longitudinal speed, as in the former case the steering is almost twice as large as in latter case, yielding the need for more tractive torque to keep the initial longitudinal speed throughout the maneuver.

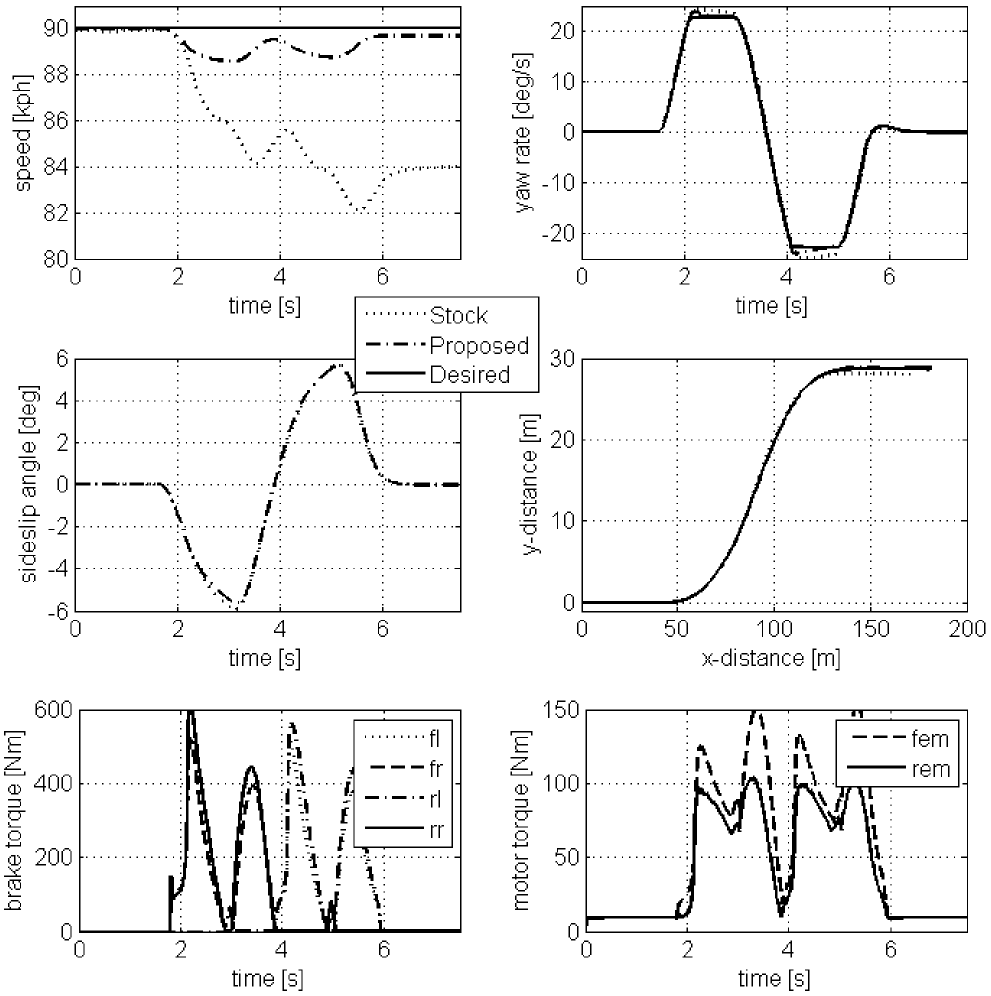

Control	$(V_{x\_error})_{max}$ *[kph]*	$(V_{x\_error})_{rms}$ *[kph]*	$(r_{error})_{max}$ *[deg/s]*	$(r_{error})_{rms}$ *[deg/s]*	β_{max} *[deg]*	$(\beta_{deviation})_{max}$ *[deg]*	Consumed energy *[kJ]* *(Tractive/Battery+Brake=Total)*
Stock	7.92	5.14	1.30	0.71	5.91	-	724.8+165.4=890.2
Proposed	1.40	1.01	1.38	0.58	5.69	-	*460.8+139.9=600.7*

(a) Vehicle dynamics, brake and motor torque profiles continued

Figure 55 Lane change on dry asphalt maneuver simulation results for the vehicle controlled with the proposed controller

Figure 55 continued

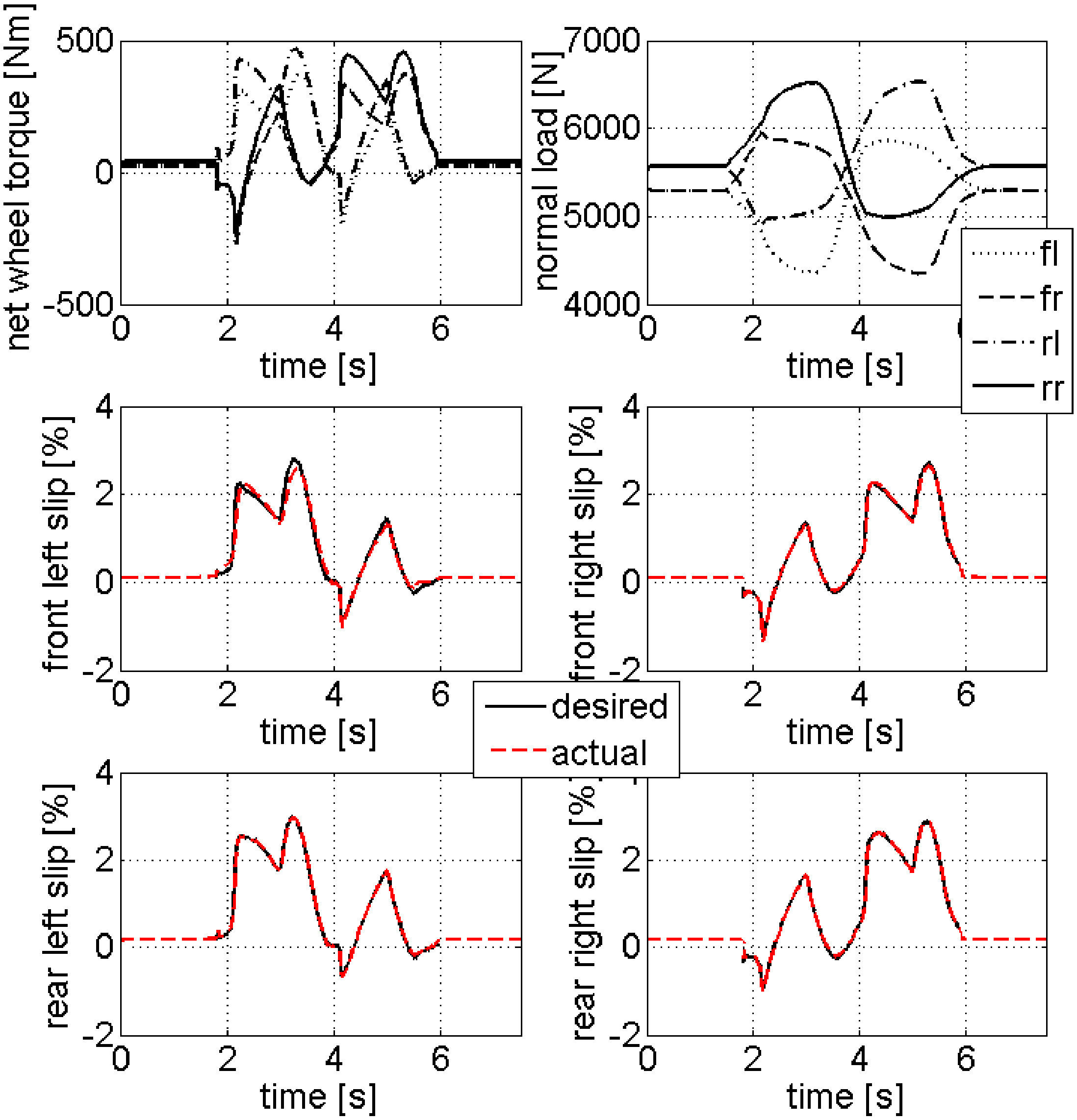

(b) Net wheel torque, normal load, desired and actual longitudinal slip for each wheel

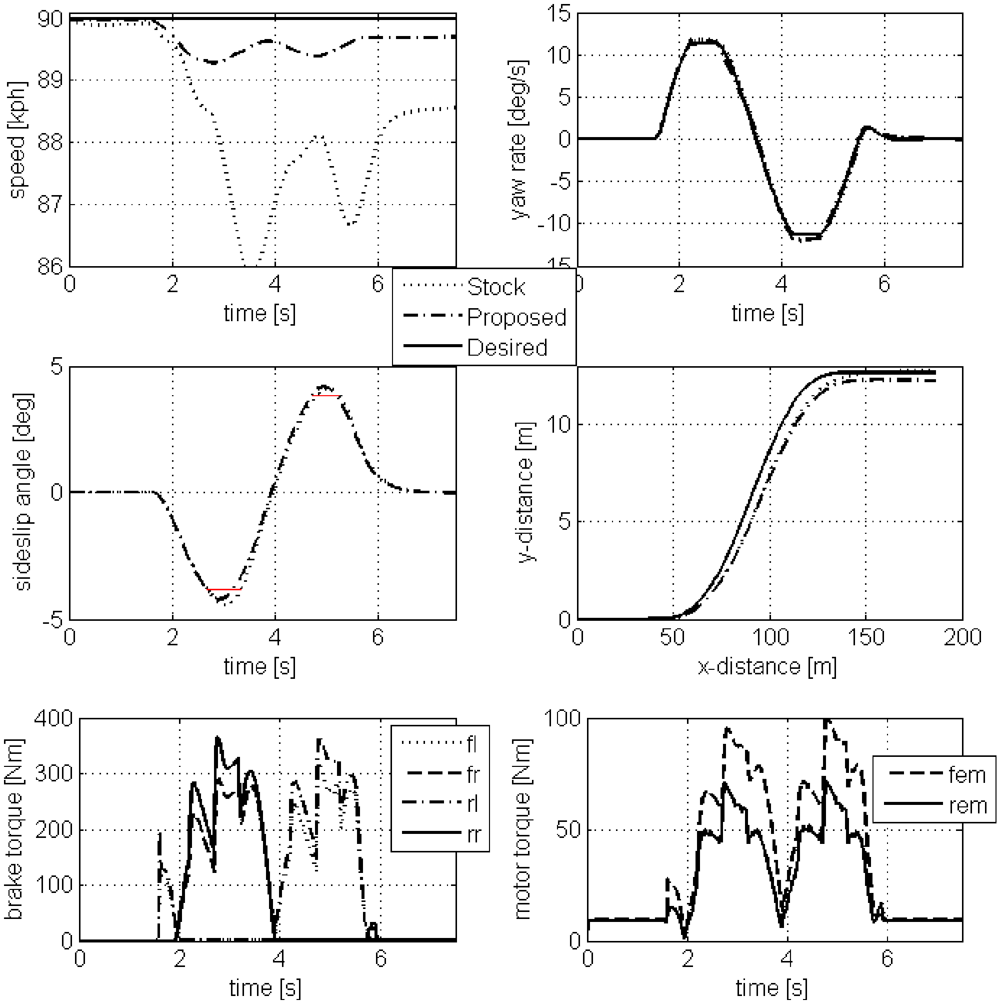

Control	$(V_{x\_error})_{max}$ *[kph]*	$(V_{x\_error})_{rms}$ *[kph]*	$(r_{error})_{max}$ *[deg/s]*	$(r_{error})_{rms}$ *[deg/s]*	β_{max} *[deg]*	$(\beta_{deviation})_{max}$ *[deg]*	Consumed energy *[kJ]* *(Tractive/Battery+Brake=Total)*
Stock	4.13	2.48	0.65	0.39	4.44	0.56	458.2+122.0=580.2
Proposed	0.72	0.51	0.95	0.51	4.20	0.32	*282.4+126.3=408.7*

(a) Vehicle dynamics, brake and motor torque profiles continued

Figure 56 Lane change on wet asphalt maneuver simulation results for the vehicle controlled with the proposed controller

Figure 56 continued

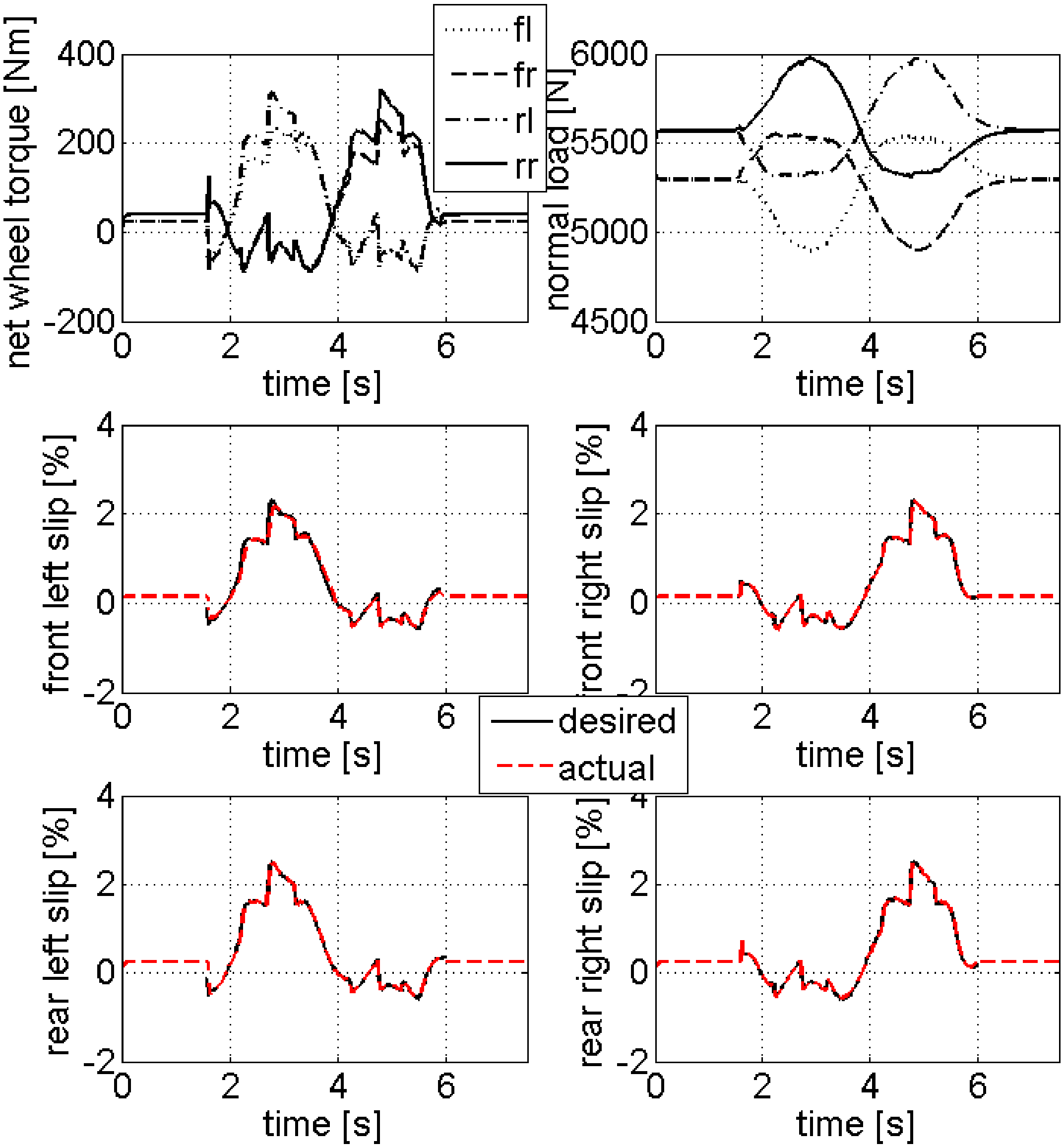

(b) Net wheel torque, normal load, desired and actual longitudinal slip for each wheel

Another observation from the net wheel torque profiles is that the magnitude of the net torque on rear wheels is slightly higher than the one on the front ones. The reason, as shown by the normal load profiles, is that the load and therefore force generation capacity on the rear tires is higher than on the front ones, due to both static load distribution and lateral load transfers.

Another interesting observation is that, although both rear and front wheels are braked to avoid oversteering, the brake energy consumed is less than that of the stock fuzzy scheme for the dry asphalt case that applies braking to a single wheel.

The final observation from the lane change maneuver simulation results is that the desired longitudinal slip values, as dictated by the control allocation, are tracked quite well by the proposed VSC strategy.

The main observation from the J-turn maneuver simulation results for speed, yaw rate and sideslip angle responses of Figures 57a and 58a is that there is not much difference between the stock and proposed VSC schemes. For the J-turn on wet asphalt (and also for the lane change on wet asphalt), as the sideslip angle exceeds the threshold, desired yaw rate tracking is sacrificed by increasing the understeer coefficient until the sideslip angle goes back below the threshold, preventing excessive increase of the sideslip angle. For this maneuver, the proposed scheme achieves better yaw tracking in comparison to the stock VSC, and allows the vehicle to stay closer to the desired trajectory.

For both J-turn maneuvers, there is again a benefit of using the electric motors in terms of energy consumption, this time more significant than the benefit obtained for the

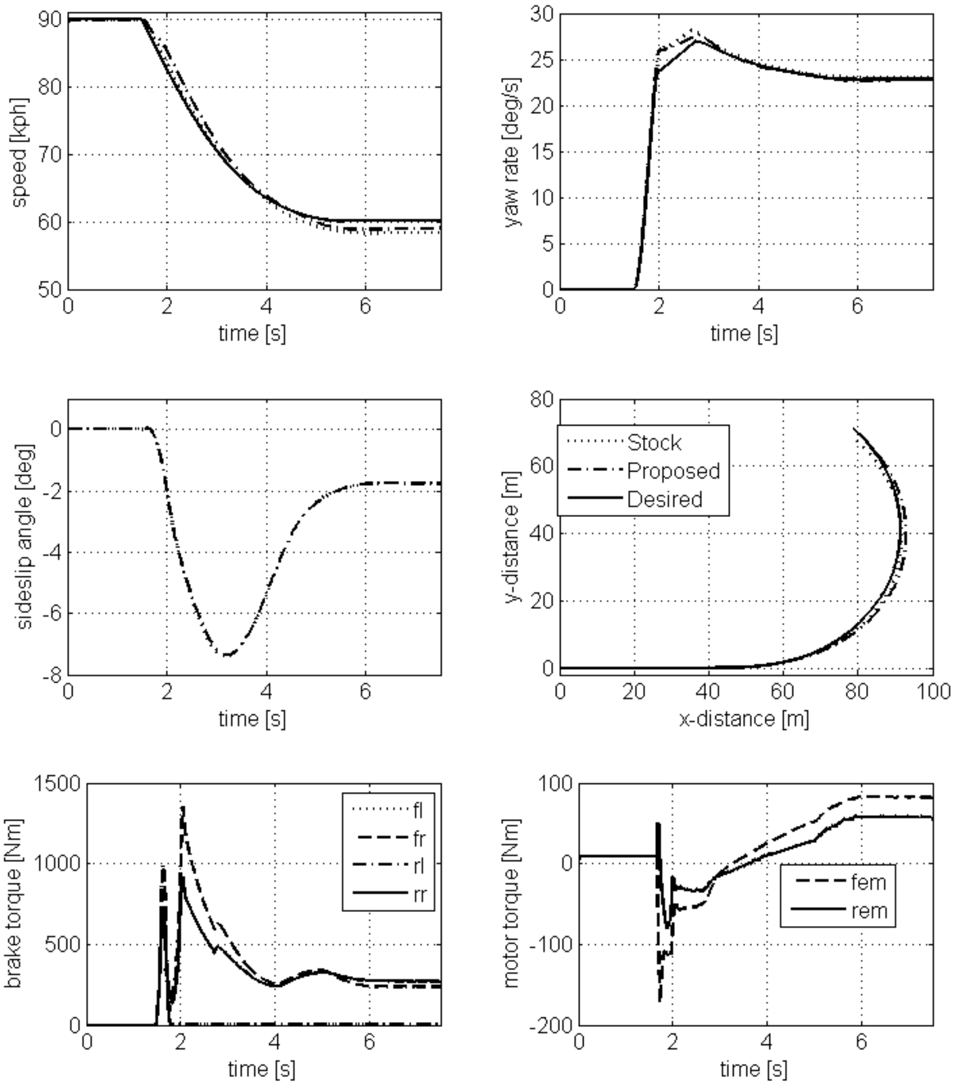

Control	$(V_{x\_error})_{max}$ *[kph]*	$(V_{x\_error})_{rms}$ *[kph]*	$(r_{error})_{max}$ *[deg/s]*	$(r_{error})_{rms}$ *[deg/s]*	β_{max} *[deg]*	$(\beta_{deviation})_{max}$ *[deg]*	Consumed energy *[kJ]* *(Tractive/Battery+Brake=Total)*
Stock	1.76	1.19	1.78	0.63	7.39	-	353.6+294.5=648.0
Proposed	2.75	2.03	2.32	1.10	7.36	-	128+247.3=375.3

(a) Vehicle dynamics, brake and motor torque profiles continued

Figure 57 J-turn on dry asphalt maneuver simulation results for the vehicle controlled with the proposed controller

Figure 57 continued

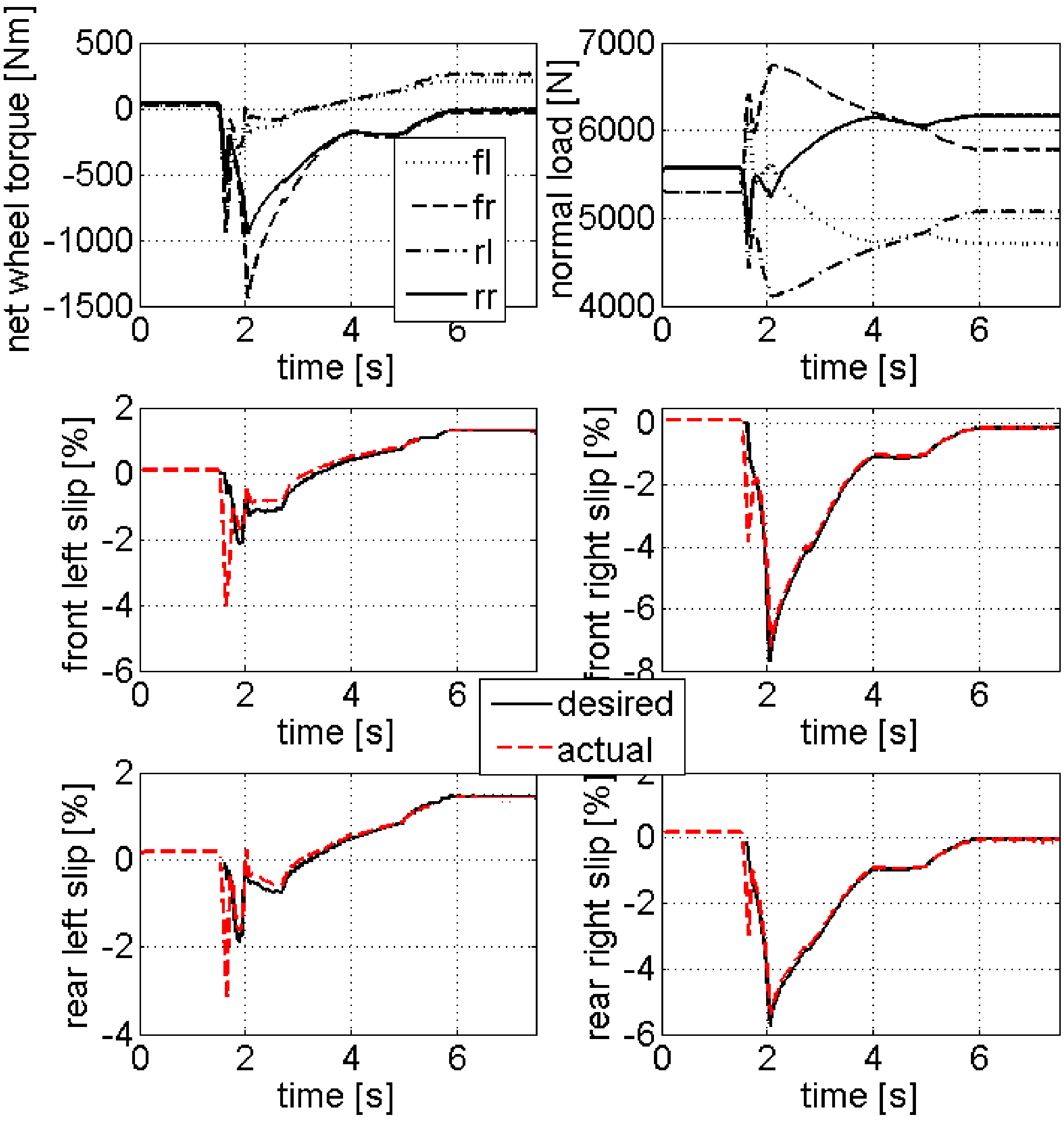

(b) Net wheel torque, normal load, desired and actual longitudinal slip for each wheel

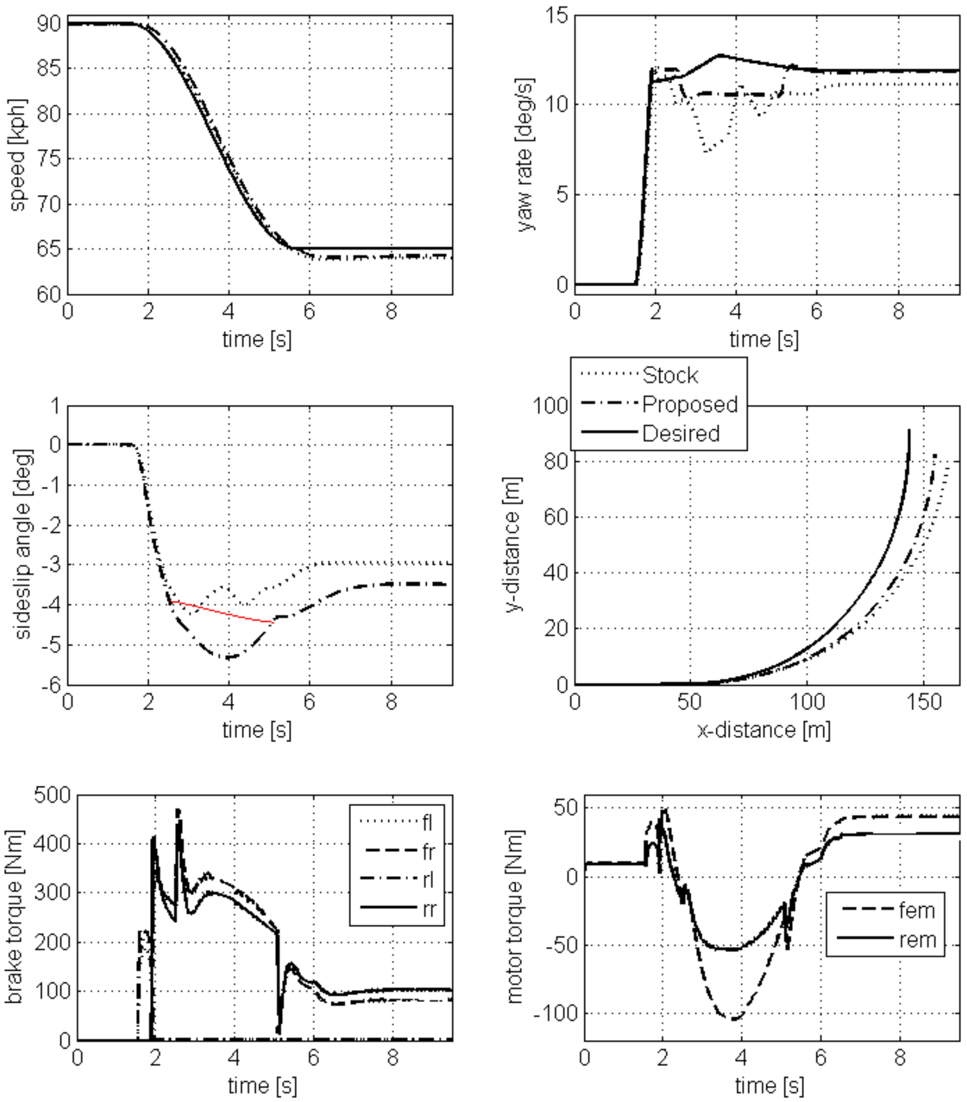

Control	$(V_{x\_error})_{max}$ *[kph]*	$(V_{x\_error})_{rms}$ *[kph]*	$(r_{error})_{max}$ *[deg/s]*	$(r_{error})_{rms}$ *[deg/s]*	β_{max} *[deg]*	$(\beta_{deviation})_{max}$ *[deg]*	Consumed energy *[kJ]* *(Tractive/Battery+Brake=Total)*
Stock	1.15	0.83	5.20	1.94	4.23	-	325.3+320.7=646.0
Proposed	1.40	1.08	2.14	1.51	5.32	1.09	39.3+177=216.3

(a) Vehicle dynamics, brake and motor torque profiles continued

Figure 58 J-turn on wet asphalt maneuver simulation results for the vehicle controlled with the proposed controller

Figure 58 continued

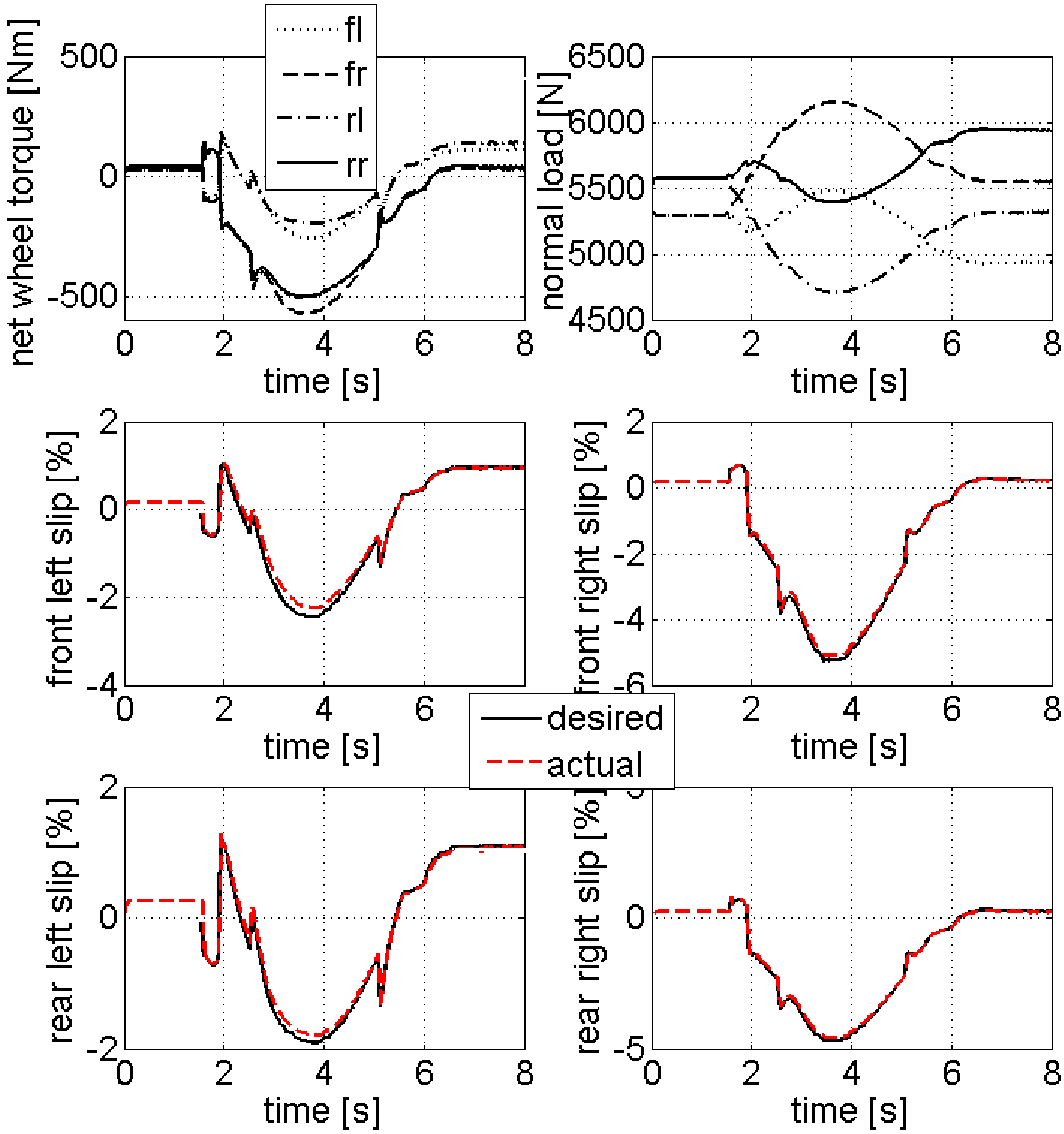

(b) Net wheel torque, normal load, desired and actual longitudinal slip for each wheel

lane change maneuver case. This is true because regenerative braking provided by the electric motors, reduces the load on friction brakes as well, especially during the wet asphalt case, where the dissipated brake energy is halved in comparison to the stock VSC case.

The net wheel torque profiles of Figures 57b and 58b show that during deceleration, the right (outer) wheels are braked more than the left (inner) ones to avoid oversteering. The front right wheel is braked with the highest magnitude. This is due to the longitudinal and lateral load transfers that increase the load on the front right wheel. For the dry asphalt case, the load on the rear right wheel also increases despite longitudinal load transfer due to deceleration, since the lateral load transfer is dominant.

For the J-turn maneuver simulation results, it is interesting to observe from the net torque profiles that that there are instances where the outer (right) wheels are braked whereas the inner (left) ones are accelerated, although the vehicle still decelerates. For instance, for the dry asphalt case of Figure 57b, the sign of the net torque (or slip) changes from negative to positive for the left wheels around t=3s although the vehicle keeps decelerating at that time. For the wet asphalt case of Figure 58, it is observed that the left wheels are accelerated initially, approximately half a second after VSC is activated, although the vehicle is decelerating. This is due to the fact that yaw tracking error is penalized more than speed tracking error in the control allocation scheme since the high priority control objective is to track the desired yaw rate, as also noted in Section 5.3.3. As the steady state speed is reached, this time tractive torque is provided to the wheels on the left side in order to keep the constant turning radius and speed.

Another important consideration in the evaluation of the proposed VSC is the effect of the control strategy and of the actuation effort on the drivetrain, as the strategy blends axle motor braking/traction with individual wheel braking. As mentioned earlier, the two ends of the half shafts are occasionally subject to torques with different signs. The resulting torque fluctuation may produce undesired stress or vibration.

The angle of twist of the half shafts is shown in Figure 59 for all four aforementioned maneuvers. As evident from the figure, the maximum amplitude of the angle of twist of the half shafts is less than half a degree. By using the relation between angle of twist and maximum shear strain at the outer surface of the shaft [70], the maximum shear stress can be expressed as

$$\tau_{\max} = \frac{r\phi}{l} G \tag{114}$$

where r and l are the half shaft radius and length, respectively, ϕ is the angle of twist, and G is the shear modulus. When the parameters for the half-shafts of the vehicle are substituted into Equation 114 the maximum stress comes out to be 34.6 MPa which is lower than the steel yield strength for shear, 144.8 MPa. Therefore, the proposed strategy that blends axle motor traction with individual wheel braking would not cause a plastic deformation of the half shafts. Furthermore, undesirable oscillation is not observed.

Another consideration in evaluating the proposed VSC scheme is the response of the battery. Figure 60 shows the battery current and SOC for the four maneuvers mentioned above, with an initial battery SOC 90%. Positive and negative currents represent battery discharging and charging, respectively.

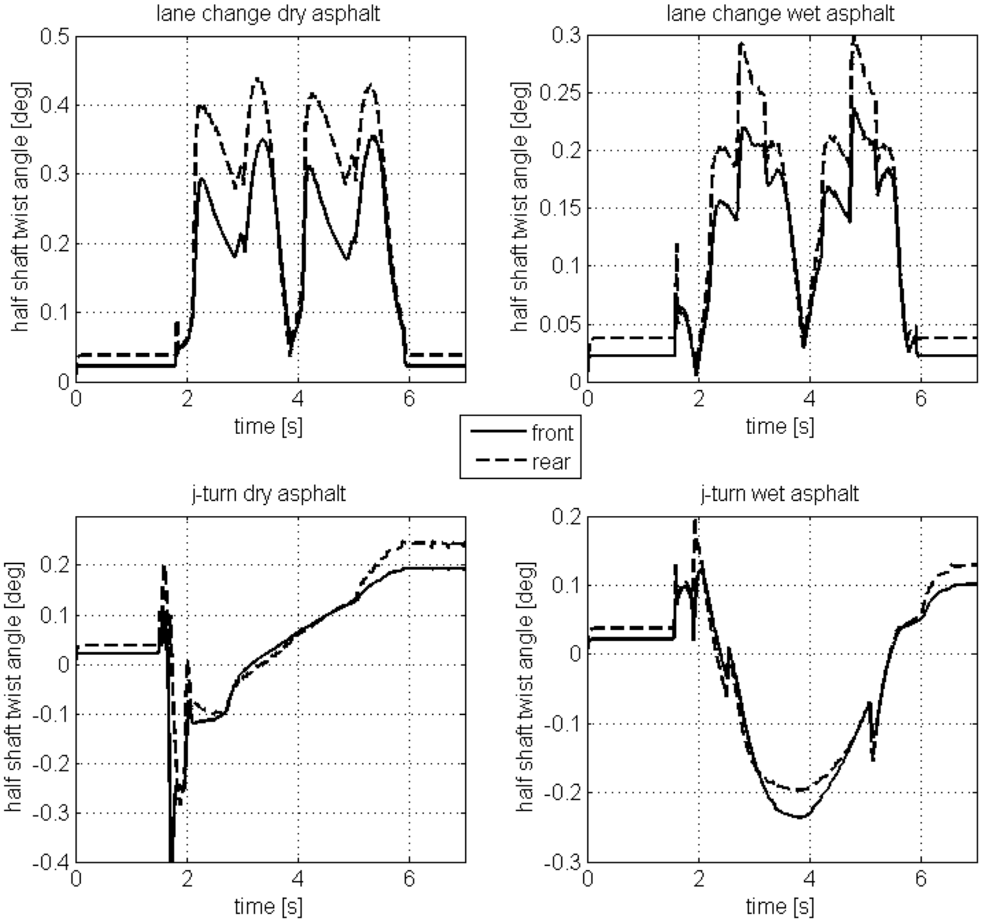

Figure 59 Angle of twist of the front and rear half-shafts during different maneuvers

It is observed that for the lane change maneuvers, the battery SOC drops as current is supplied to the electric motors from the battery to generate the required tractive torque in order to keep vehicle speed constant during cornering. For the dry asphalt case, discharge current reaches a high level of 500 amps, below the maximum current limit of the 22 kwh lithium ion battery pack for discharging, which is around 600 amps.

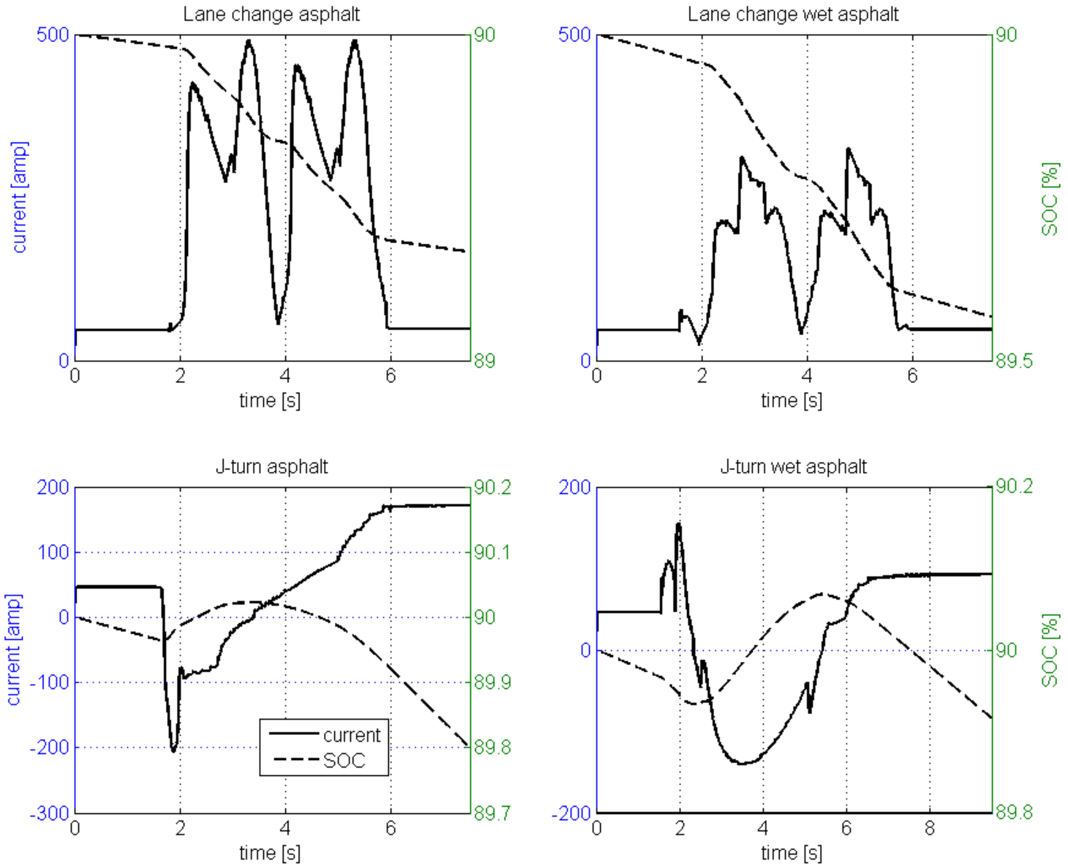

Figure 60 Simulation results for the battery current and SOC

During the J-turn maneuvers, the effect of regenerative braking is observed as the battery SOC increases initially during the maneuvers. For the dry asphalt case, a high level of charging current of 200 amps is reached, which is again below the maximum current limit of the battery pack during charging which is around 300 amps. For the wet asphalt case, the SOC comes back to its initial value after 8 seconds, thanks to utilization of motor regenerative braking.

5.5. Model in-the-loop (MIL) simulations

The simulation results illustrated in the previous section are satisfactory in the sense that yaw rate tracking and sideslip angle stabilization is accomplished without interfering in the driver's speed demand and much less energy is consumed with the proposed VSC in comparison to the conventional fuzzy controllers. Furthermore, the response of the powertrain, mainly the half-shafts and the battery, is within safe limits. However, further verification of the controller is required in real time, as it is important to see if the controller works properly in real time operation. For this purpose, the driver, powertrain and vehicle dynamics model built for the hybrid SUV as described in earlier chapters are simulated using the DSpace DS1006 Processor Board along with DS 2210 HIL I/O board; the controller model is loaded on the DS MicroAutoBox (MABX) 1401 vehicle controller [71]. The real time simulation set-up is shown in Figure 61. Signal communication in between for yaw rate, acceleration, wheels speed, steering angle, torque commands, etc. is established via CAN protocol. In creating the database for these signals, the GM CAN database for the original production vehicle was used. For custom signals that do not exist in the GM CAN database such as EHB or motor torque commands, 16 bit signals are created. The spec list of these CAN signals used for the proposed VSC is provided in *Appendix E*. For the real time simulations, the fixed simulation step time is selected as 1 millisecond. A higher step size can be chosen but step sizes lower than 1 millisecond are not possible, as the controller records task over-runs, which are an indication that the time it takes for execution of one control loop is insufficient. However, a 1 ms time step is quite acceptable.

Figure 61 Real time simulation set-up showing the main components.

The conceptual illustration of the real time simulation set-up is shown in Figure 62.

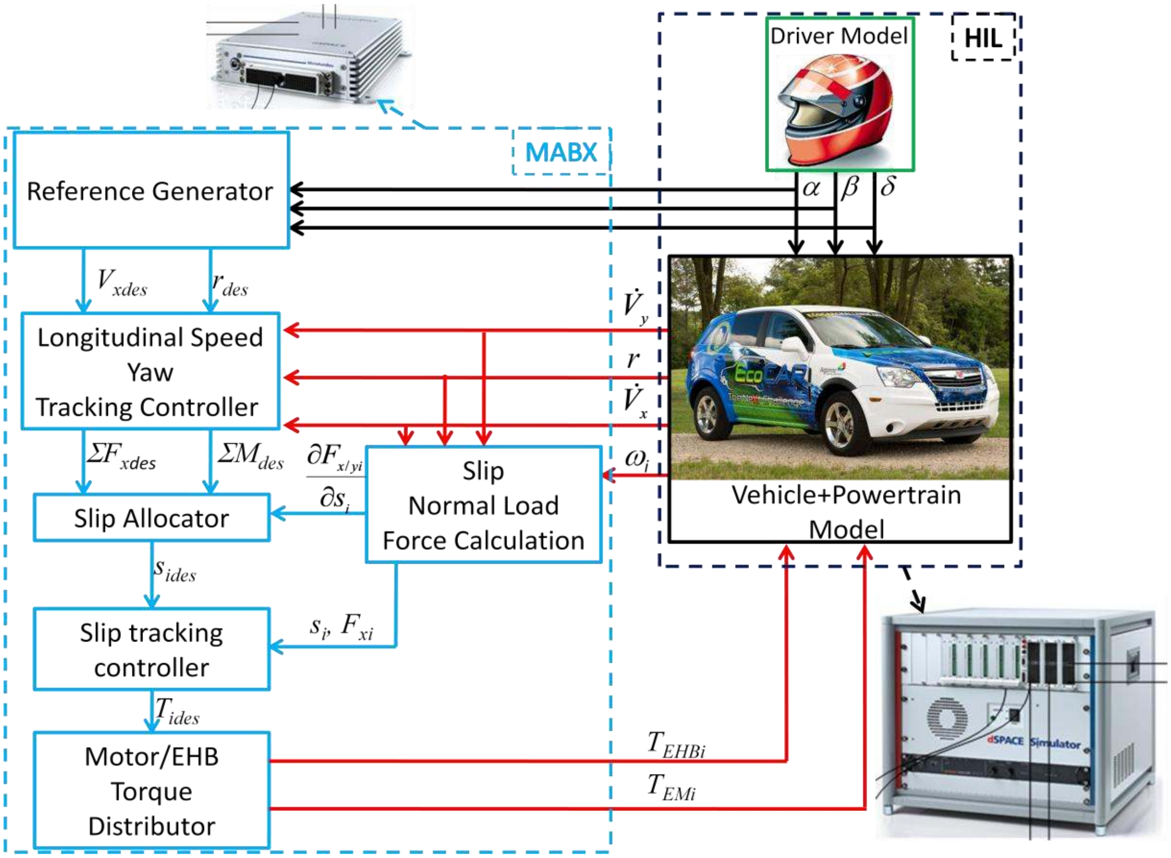

Figure 62 Model in-the-loop (MIL) simulation set-up

Figures 63through 66 show the real time simulation results for the lane change and J-turn maneuvers imposed on the SIL simulation results of the previous section in order to compare SIL and MIL simulation results for the vehicle controlled with the proposed VSC.

These results show that there is a nearly perfect match between SIL and MIL simulation results for the lane change and J-turn maneuvers on dry and wet asphalt, confirming that the proposed VSC is implementable in real time. The proposed strategy is

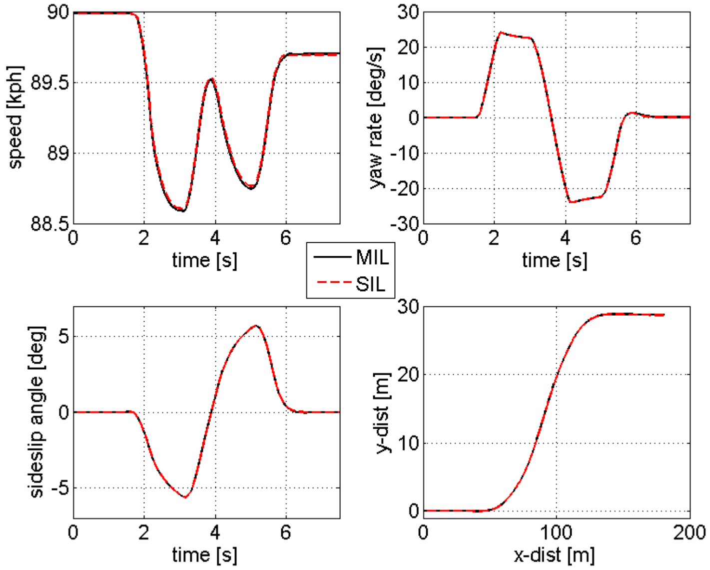

(a) Vehicle dynamics

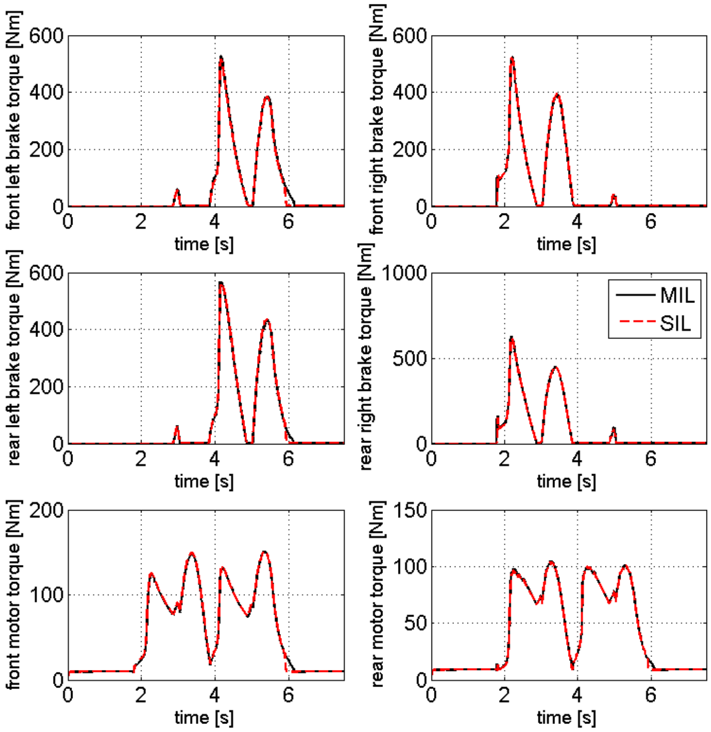

(b) Brake and motor torques

Figure 63 Comparison of SIL and MIL simulation results for lane change on asphalt maneuver.

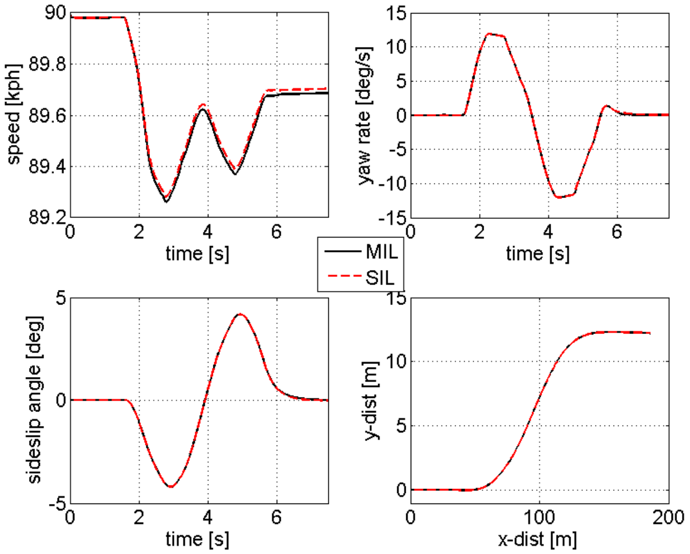

(a) Vehicle dynamics

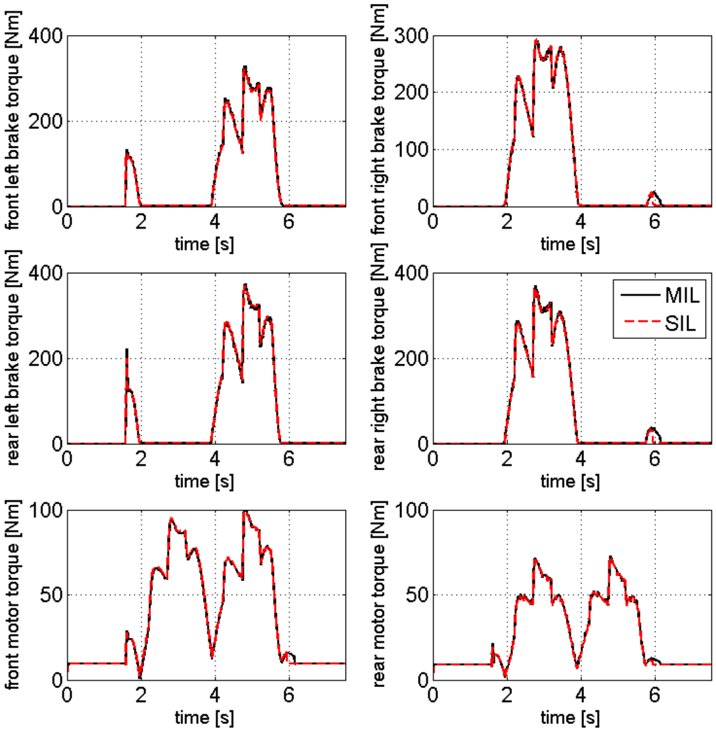

(b) Brake and motor torques

Figure 64 Comparison of SIL and MIL simulation results for lane change on wet asphalt maneuver.

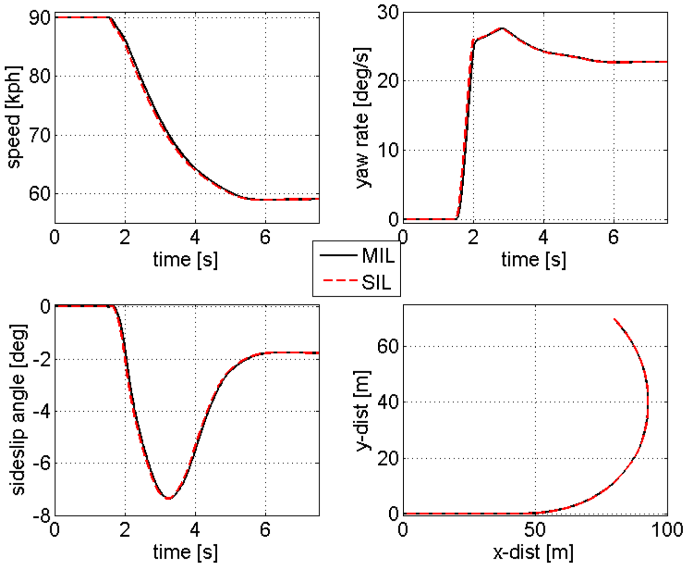

(a) Vehicle dynamics

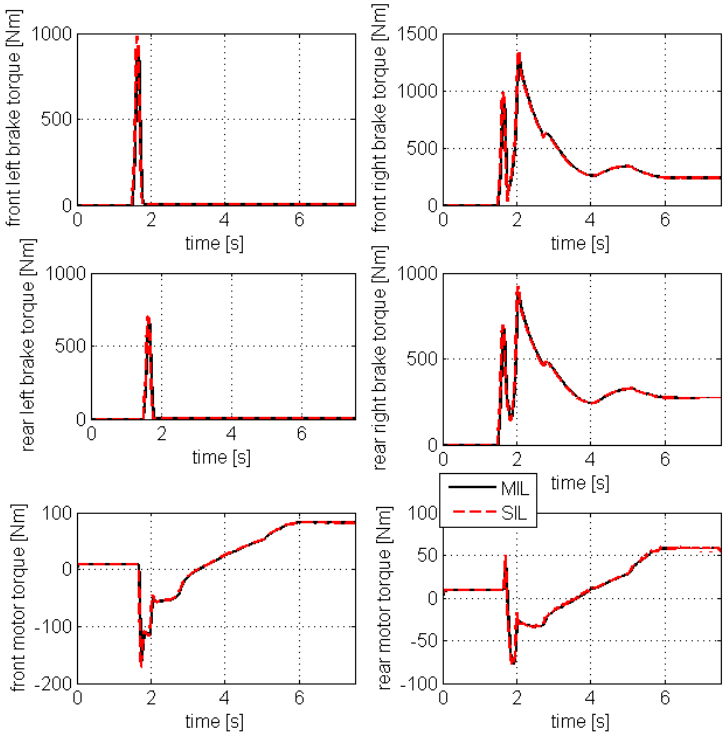

(b) Brake and motor torques

Figure 65 Comparison of SIL and MIL simulation results for J-turn on asphalt maneuver.

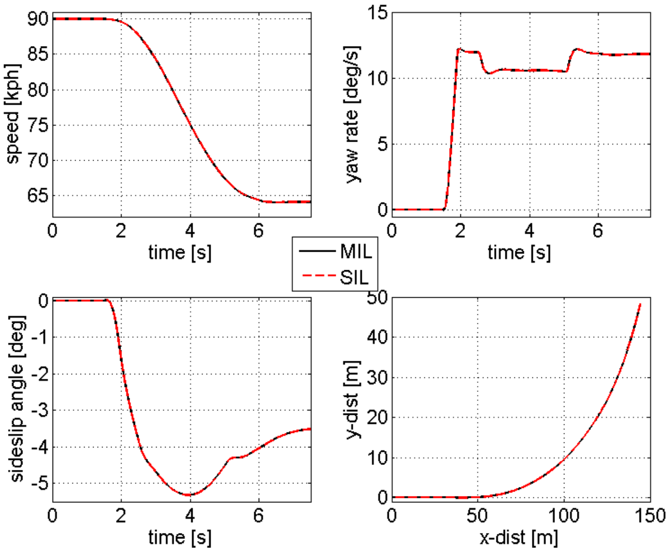

(a) Vehicle dynamics

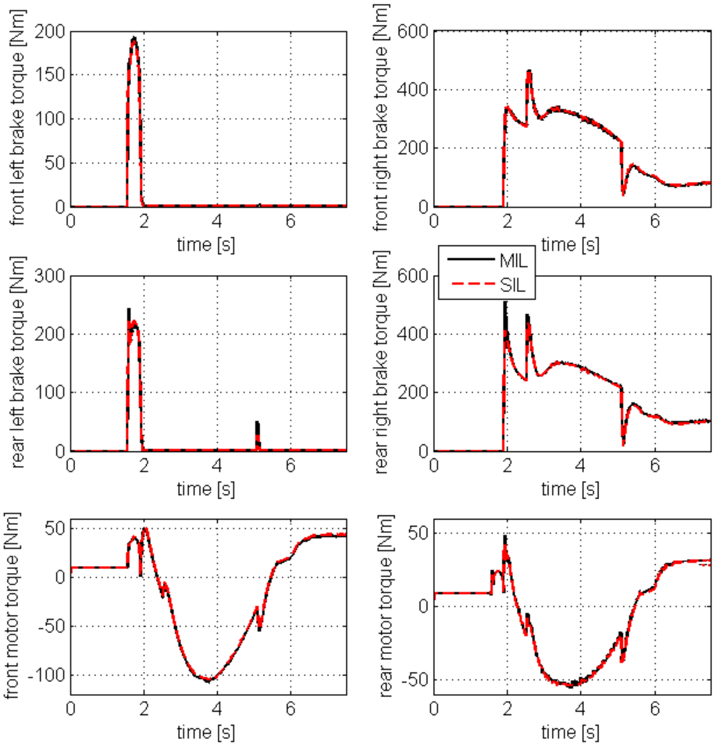

(b) Brake and motor torques

Figure 66 Comparison of SIL and MIL simulation results for J-turn on wet asphalt maneuver.

tested with one final set of maneuvers directly in real time this time on a snowy surface, where the coefficient of friction is 0.2. For these maneuvers the initial velocity is 50 kph and the maximum steering angle is 50 degrees similar to the wet asphalt case as shown in Figure 12. The real time simulation results are shown in Figure 67 and Figure 68 for the lane change and J-turn maneuvers on the snowy surface, respectively.

The first observation from the lane change maneuver simulation results of Figure 67a is that the desired yaw velocity and speed are tracked quite well, as seen from the tabulated results. The understeer coefficient is kept higher for this maneuver in comparison to the one for the dry and wet asphalt maneuvers. Although the desired trajectory is not tracked perfectly, the driver would be able to steer further as the steerability threshold for sideslip angle (which is around 2.5 degrees for this maneuver) is not exceeded.

The net torque and slip profiles of Figure 67b show that the vehicle is understeering for around half a second initially, as the right side wheels are accelerated whereas the left ones are braked. Then for the rest of the maneuver, in order to prevent oversteering, the outer wheels are braked, and the inner ones are accelerated, as expected. During the entire maneuver, longitudinal slip is kept quite low, namely below 1%, as required by the inequality constraint of the control allocation.

Similar observations are made for the J-turn maneuver simulation results of Figure 68. Desired speed and yaw rate are tracked satisfactorily without exceeding the sideslip angle steerability threshold of 2.5 degrees, as seen in Figure 68a. Around half a second after VSC is activated, the net wheel torque (and slip) values of the left wheels are

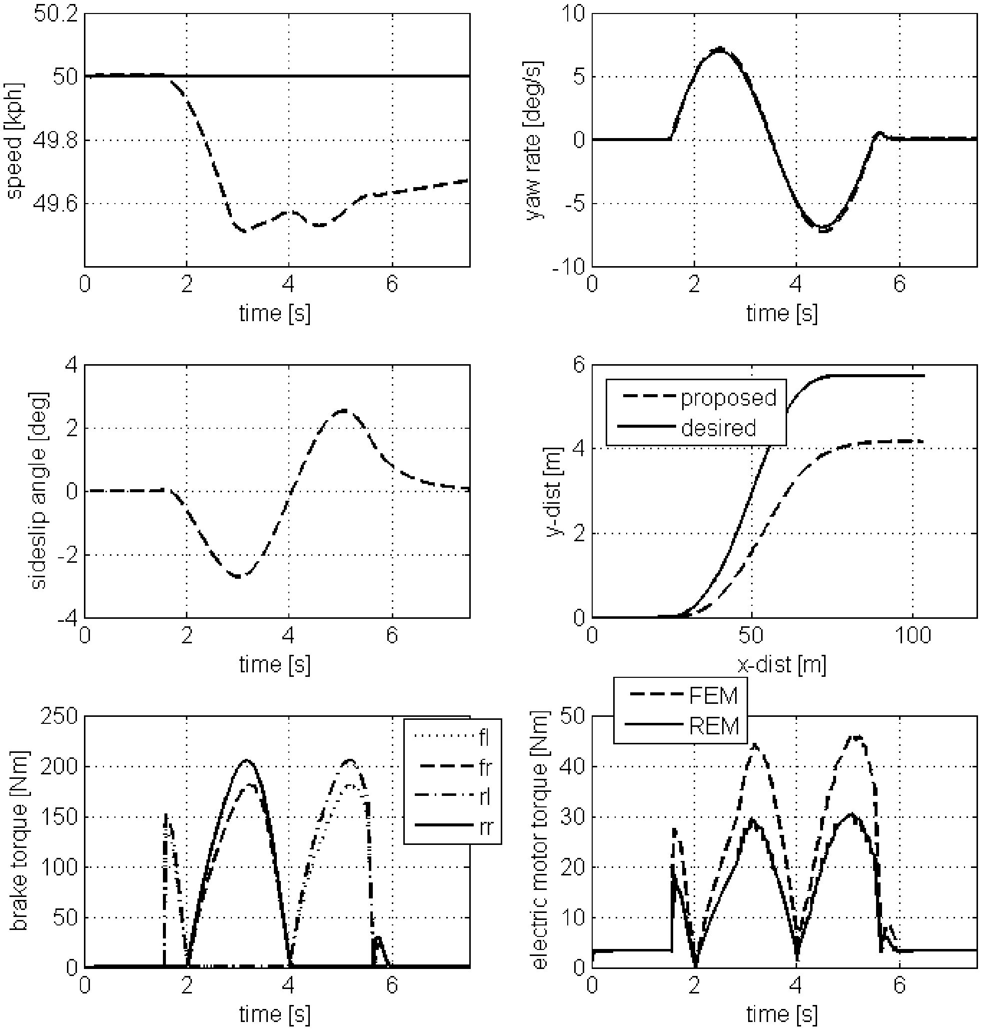

Control	$(V_{x\_error})_{max}$ *[kph]*	$(V_{x\_error})_{rms}$ *[kph]*	$(r_{error})_{max}$ *[deg/s]*	$(r_{error})_{rms}$ *[deg/s]*	β_{max} *[deg]*	$(\beta_{deviation})_{max}$ *[deg]*	Consumed energy *[kJ]* *(Battery+Brake=Total)*
Proposed	0.49	0.40	0.12	0.09	2.73	-	51.2+41.4=92.6

(a) Vehicle dynamics, brake and motor torque profiles

continued

Figure 67 Real time simulation results for the lane change maneuver on snowy surface for the vehicle controlled with the proposed controller

Figure 67 continued

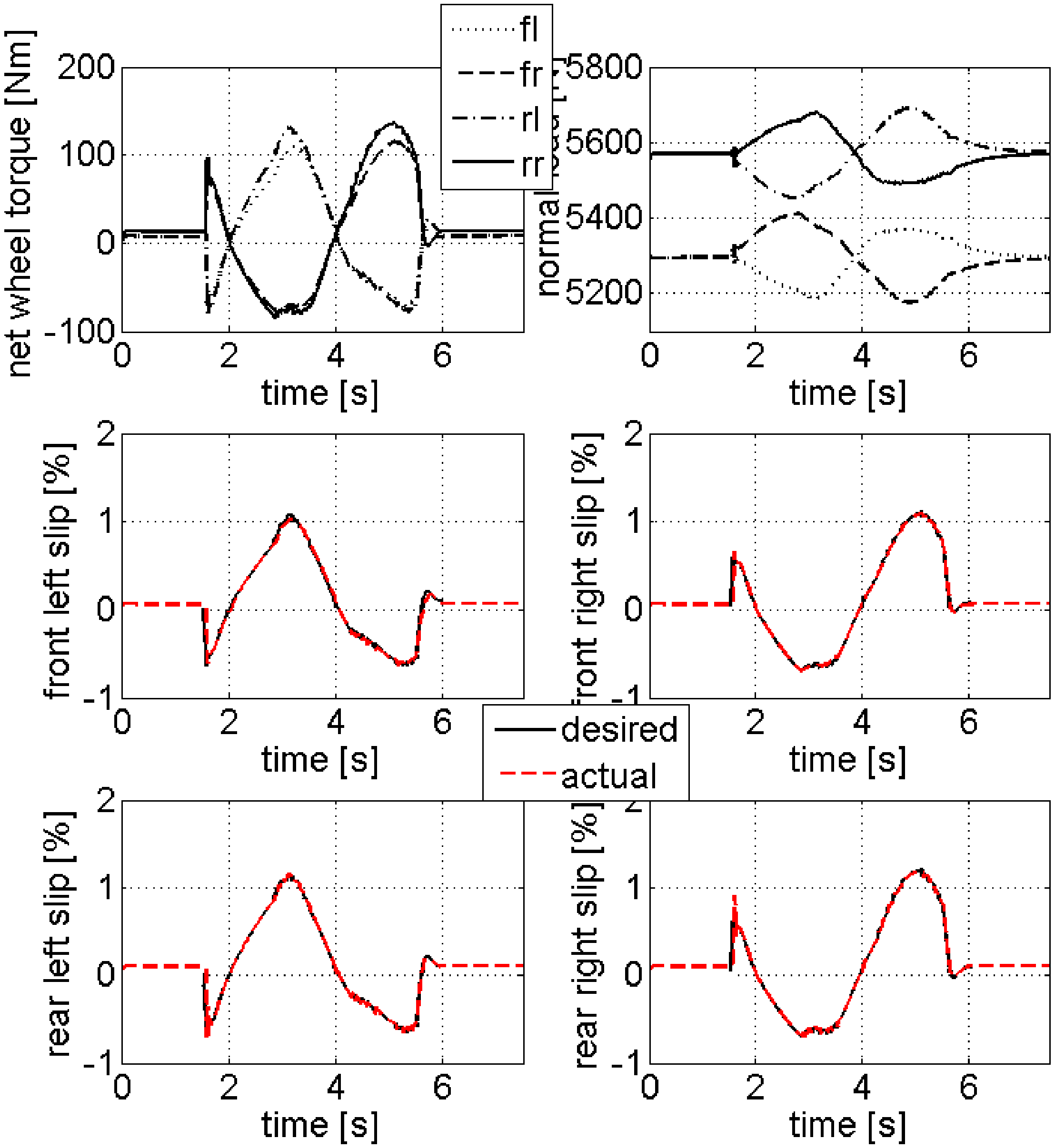

(b) Net wheel torque, normal load, desired and actual longitudinal slip for each wheel

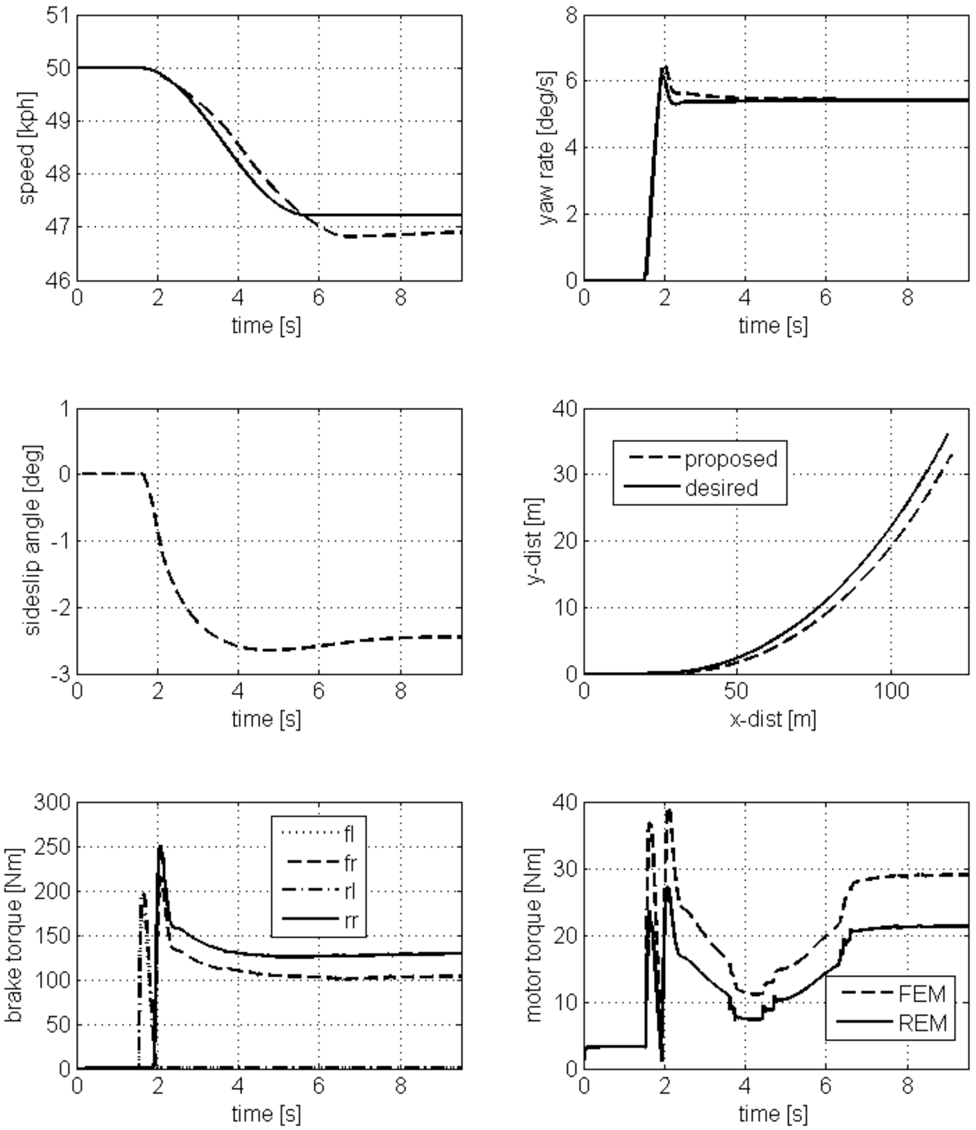

Control	$(V_{x\_error})_{max}$ *[kph]*	$(V_{x\_error})_{rms}$ *[kph]*	$(r_{error})_{max}$ *[deg/s]*	$(r_{error})_{rms}$ *[deg/s]*	β_{max} *[deg]*	$(\beta_{deviation})_{max}$ *[deg]*	Consumed energy *[kJ]* *(Battery+Brake=Total)*
Proposed	0.40	0.10	0.52	0.20	2.65	0.25	104.0+78.0=182.0

(a) Vehicle dynamics, brake and motor torque profiles continued

Figure 68 Real time simulation results for the j-turn maneuver on snowy surface for the vehicle controlled with the proposed controller

Figure 68 continued

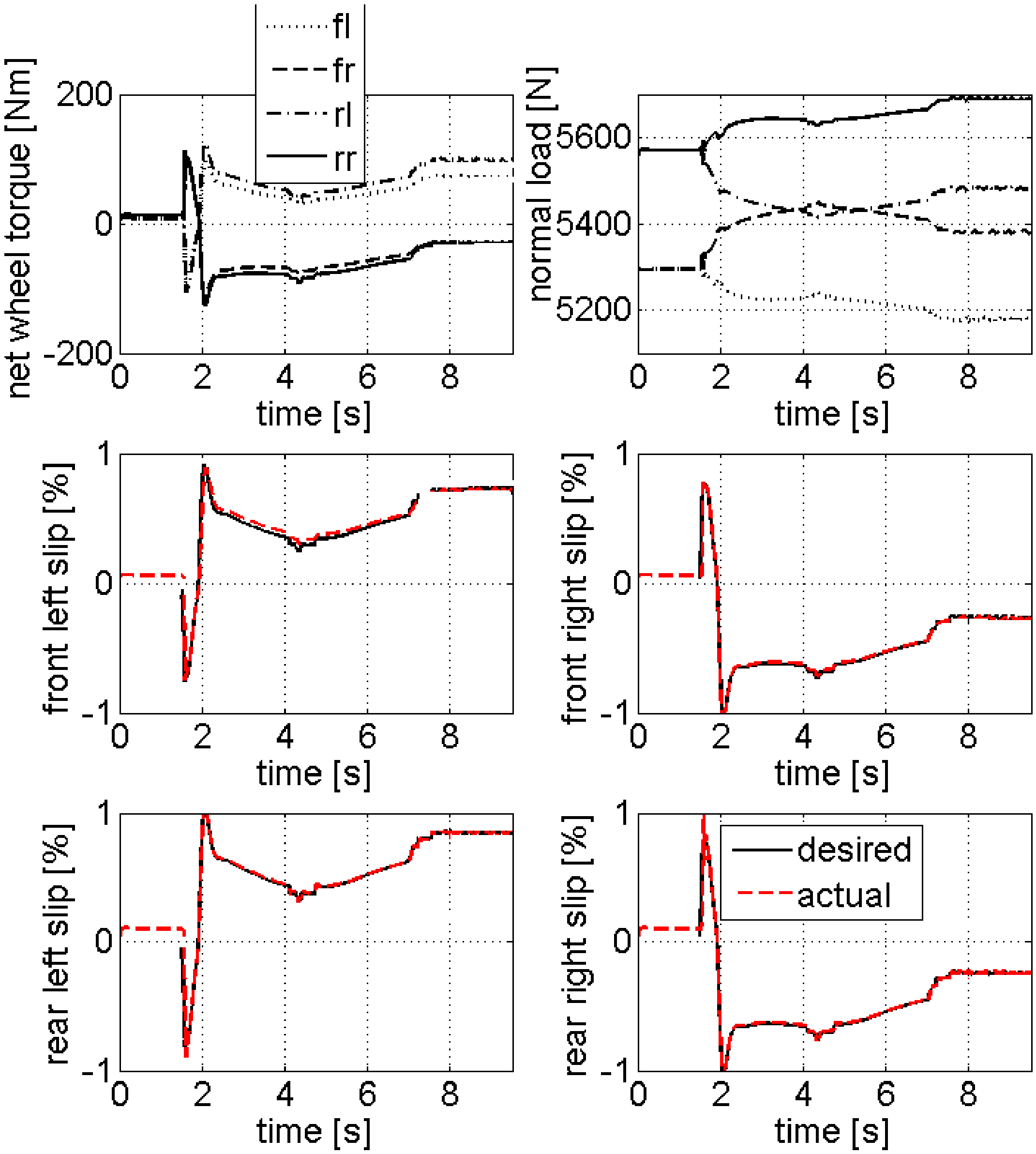

(b) Net wheel torque, normal load, desired and actual longitudinal slip for each wheel

negative, and the right ones positive, to track the desired yaw rate which is higher than the actual one, i.e. against understeering. Immediately after that instant, the left (inner) wheels are accelerated and the right (outer) ones are braked to reduce the yaw rate to the desired level, i.e. to prevent oversteering, as seen in Figure 68b. Slip is again kept below 1%. One difference of this maneuver from the J-turn maneuvers on the other road surfaces is that the driver does not brake this time. Instead he just releases the accelerator pedal simultaneously with the steering action. Therefore there is no regenerative braking this time as can be seen in the motor torque profiles.

The responses of the half shafts and the battery for the lane change and j-turn maneuvers on snowy surface are shown in Figure 69. Similar to the maneuvers on dry and wet asphalt, the results show that there is neither undesired vibration nor battery current saturation, which shows that the proposed strategy is compatible with the intended operation of the hybrid vehicle.

5.6. Roll Dynamics Response

Up to this point, the roll dynamics of the vehicle have not been considered among the criteria used to evaluate the proposed VSC scheme, since in all simulated steering maneuvers roll angles are fairly small, as shown in Figure 70.

Because of the increased mass of the hybrid powertrain, the center of gravity of the vehicle is lower than in the production vehicle, (measured around 580 mm), is lower than in the production vehicle, reducing the risk of roll over. In order to quantify the roll over risk, the net rolling moment with respect to the center of contact patch of the left tire of

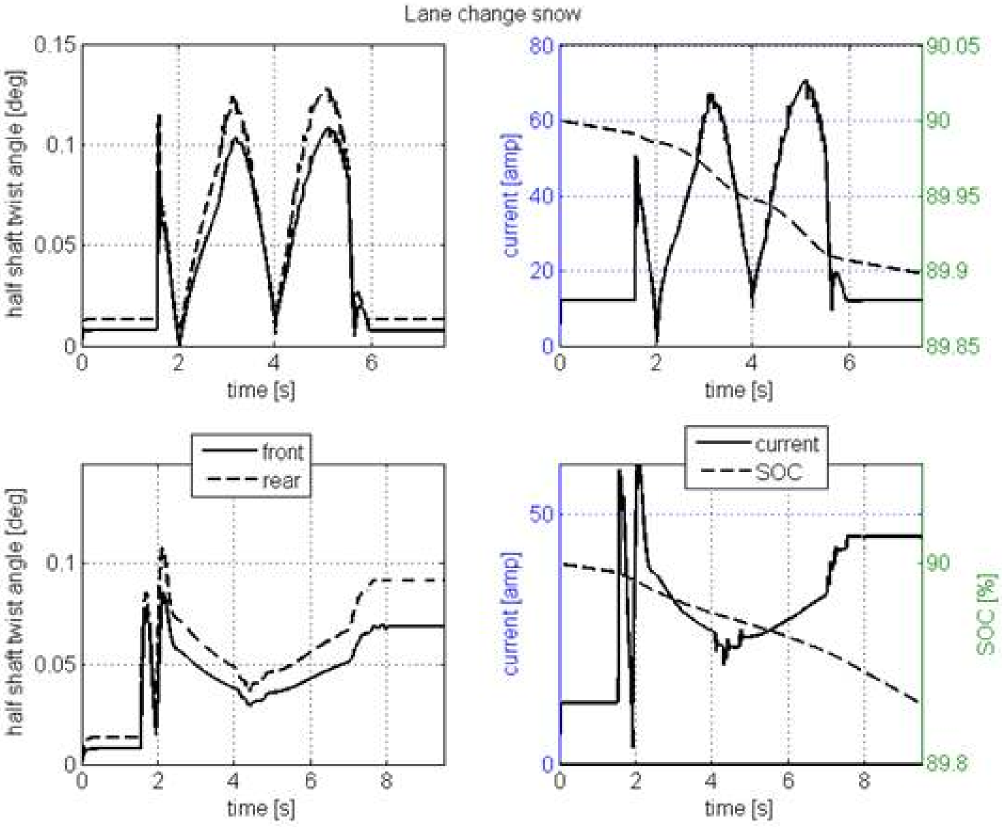

Figure 69 Angle of twist of the half shafts on the left, battery current and SOC on the right for the maneuvers on snowy surface

Figure 34b can be expressed, neglecting suspension effects, by

$$\sum M_o = Mg\left(\frac{t}{2} - h\sin(\phi)\right) - Ma_y h\cos\phi \tag{115}$$

Therefore the lateral acceleration limit that would initiate roll over can be expressed as:

$$a_y \geq \frac{g\left(\frac{t}{2} - h\sin(\phi)\right)}{h\cos\phi} \tag{116}$$

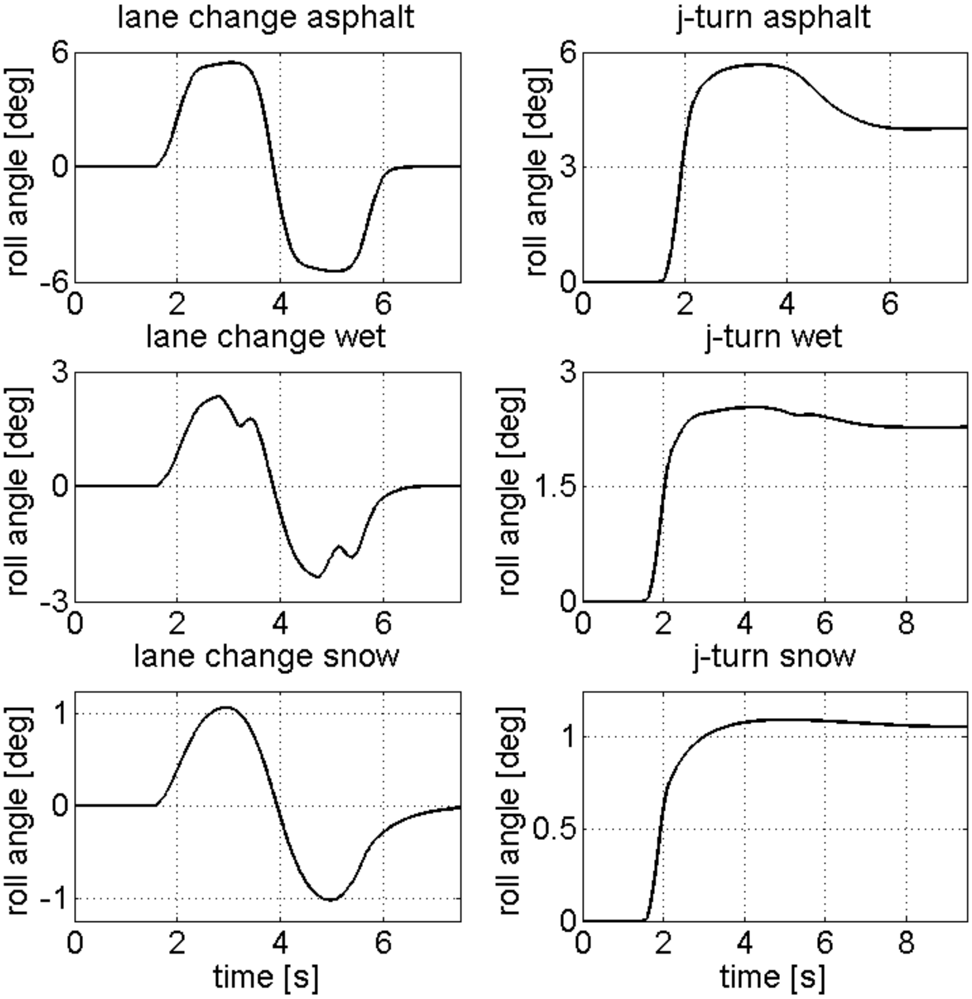

Figure 70 Real time simulation results for the roll angle of the vehicle during all the maneuvers considered

When the parameters for the hybrid SUV considered in this dissertation are substituted into Equation 116 (assuming the maximum roll angle of around 6 degrees where it is observed during the maneuvers on asphalt), the rollover threshold for lateral acceleration comes out to be 12.2 m/s^2. This value is higher than the maximum lateral acceleration attained during the aforementioned maneuvers which is around 9.5 m/s^2. Therefore, the vehicle rollover dynamics are in the stable range for all the aforementioned maneuvers.

5.7. Summary of this Chapter

Chapter 5 has presented a novel control approach for vehicle stability control that makes use of the electric traction system in a hybrid electric vehicle. The proposed methodology uses a hierarchical approach to allocate forces and moments in an over actuated system. The attractivity of the defined sliding mode controllers are shown theoretically.

A comparison of the performance of the new control strategy with those explored in Chapter 2 shows improved tracking performance without loss of vehicle longitudinal speed and with reduced energy consumption. The new control allocation strategy is also shown to operate within the mechanical and electrical limits of the hybrid drivetrain.

Finally, real time implementation of the strategy, using a DSpace HIL processor to simulate driver, powertrain, and vehicle dynamics, and a DSpace MicroAutoBox as the controller, demonstrates that the proposed strategy has the potential to be implemented in real time.

6. Conclusions and Future Work

6.1. Conclusions

This dissertation has documented the conception and development of a novel control strategy to allocate braking and tractive forces in a hybrid electric vehicle equipped with axle motors, for the purpose of enhancing the vehicle stability control system.

The work described in this dissertation documents the development of a hierarchical control strategy, its design and stability proofs, and its evaluation using software and hardware in-the-loop methods.

Part of this work includes the development of a dynamic HEV simulator that is capable of demonstrating vehicle dynamics responses. For this purpose, a hybrid powertrain simulation model including batteries, motor, differential, shaft, wheel, and electro-hydraulic brake system models was developed. Furthermore, a simple yet reliable vehicle dynamics model was integrated with the powertrain model to capture longitudinal, lateral, yaw and roll degrees of freedoms of the vehicle. The development of the simulator is one of the original contributions of this dissertation

The major contribution of this work is a novel and systematic VSC strategy that distributes the corrective longitudinal force and yaw moment action to generate individual wheel slip ratios by blending regenerative axle motor braking and/or traction with individual wheel braking; so as to track the desired yaw rate and vehicle speed without causing excessive vehicle sideslip angles. This dissertation shows that including the axle electric motors within the proposed VSC frame, improves the performance of vehicle stability control in comparison to stock VSC strategies. The potential benefit of electric motors, namely their ability to provide rapid braking/tractive torque actuation is utilized in addition to the friction brakes, within the proposed VSC scheme. The proposed strategy is the first published result that shows that yaw tracking and vehicle stabilization can be performed without interfering in the driver's longitudinal speed demand. Furthermore, the strategy limits the yaw rate in order to keep the vehicle sideslip angle in the safe range, by increasing the understeer coefficient whenever a sideslip angle safety threshold is exceeded. A secondary benefit of the proposed VSC scheme is its energy saving feature, thanks to the use of highly efficient electric motors and their regenerative braking capability in comparison to a standard vehicle stability control schemes that use only brake and engine intervention.

Finally the proposed VSC strategy is tested in real time by using a model-in-the-loop set-up that involved DSpace controllers. Model-in-the-loop simulation results performed for different road conditions and steering maneuvers showed that the proposed VSC performs satisfactorily in real time as well, suggesting that it is amenable to in-vehicle implementation.

6.2. Future Work

In addition to the obvious next step, which is to implement the new control strategy in the EcoCAR vehicle, a number of other improvements are possible, and should be the subject of future studies. SIL and MIL methods, along with Monte Carlo simulation approaches could be used to evaluate the effects of:

1) Sensor noise,
2) Different emergency maneuvers such as split-μ maneuver,
3) Uncertainty in model structure and in model parameters, including vehicle mass and mass distribution.

A further step would be extending the control objective, and including roll stability control in addition to lateral and yaw motion control. In this study, roll dynamics of the vehicle does not have an important role in evaluation of the stability of the vehicle because the heavy hybrid powertrain lowers the height of center of gravity drastically which reduces the roll angle to a few degrees in the simulations performed. However, for a hybrid vehicle platform such as a passenger vehicle where the motors and batteries are lighter, the simulated maneuvers may cause roll angle to increase excessively, which may lead to roll stabilization need as well as yaw.

Finally, a natural evolution of this work is the application of similar hierarchical control allocation methods to vehicles equipped with individual hub motors at each wheel.

Appendix A: Derivation of Bicycle Model

The following differential equations of motion can be written from the bicycle model of Figure 4:

$$\begin{aligned} M(\dot{V}_x - V_y r) &= F_{xf}\cos(\delta_f) - F_{yf}\sin(\delta_f) + F_{xr} \\ M(\dot{V}_y + V_x r) &= F_{xf}\sin(\delta_f) + F_{yf}\cos(\delta_f) + F_{yr} \\ I_z\dot{r} &= a\left(F_{xf}\sin(\delta_f) + F_{yf}\cos(\delta_f)\right) - bF_{yr} \end{aligned} \tag{A.1}$$

If the steering angles of the front wheels are assumed to be small, such that $\cos(\delta) \cong 1$ and $\sin(\delta) \cong 0$, then Equations A.1 reduce to:

$$\begin{aligned} M(\dot{V}_x - V_y r) &= F_{xf} + F_{xr} \\ M(\dot{V}_y + V_x r) &= F_{yf} + F_{yr} \\ I_z\dot{r} &= aF_{yf} - bF_{yr} \end{aligned} \tag{A.2}$$

The term $V_y r$ on the left hand side of the first equation above is a product of two variables of small magnitude and hence can be neglected. Then the equation reduces to $M\dot{V}_x = F_{xf} + F_{xr}$ which is uncoupled from other two equations and can be used to study the acceleration performance of the vehicle in straight motion.

Treating the forward velocity of the vehicle V_x as a parameter, the degrees of freedom of the remaining system reduce to two, namely lateral and yaw velocity and formulated as:

$$\begin{aligned} M(\dot{V}_y + V_x r) &= F_{yf} + F_{yr} \\ I_z\dot{r} &= aF_{yf} - bF_{yr} \end{aligned} \tag{A.3}$$

With the knowledge that under normal driving conditions, slip angles are usually smaller than approximately four degrees, the bicycle model assumes the cornering force vs. slip angle relation in the linear range.

$$\begin{aligned} F_{yf} &= -C_f^{right}\alpha_f - C_f^{left}\alpha_f \\ F_{yr} &= -C_r^{right}\alpha_r - C_r^{left}\alpha_r \end{aligned} \tag{A.4}$$

Assuming the cornering stiffness values of tires on the same axle are equal

$$\begin{aligned} C_f^{right} &= C_f^{left} = C_f \\ C_r^{right} &= C_r^{left} = C_r \end{aligned} \tag{A.5}$$

one may arrive at:

$$\begin{aligned} F_{yf} &= -2C_f\alpha_f \\ F_{yr} &= -2C_r\alpha_r \end{aligned} \tag{A.6}$$

Substituting the above equations into Equation A.3 yields:

$$\begin{aligned} M(\dot{V}_y + V_x r) &= -2C_f\alpha_f - 2C_r\alpha_r \\ I_z\dot{r} &= -2aC_f\alpha_f + 2bC_r\alpha_r \end{aligned} \tag{A.7}$$

The slip angle expressions which can be written from Figure 4 as:

$$\begin{aligned} \alpha_f &= \delta_f - \arctan\left(\frac{V_y + ar}{V_x}\right) \quad \cong \quad \delta_f - \frac{V_y + ar}{V_x} \\ \alpha_r &= -\arctan\left(\frac{V_y - br}{V_x}\right) \quad \cong \quad -\frac{V_y - br}{V_x} \end{aligned} \tag{A.8}$$

Substitution of the above equations into equation A.7 yields:

$$\begin{Bmatrix} \dot{V}_y \\ \dot{r} \end{Bmatrix} = \begin{bmatrix} \frac{2(C_f + C_r)}{MV_x} & \frac{2(aC_f - bC_r)}{MV_x} - V_x \\ \frac{2(aC_f - bC_r)}{I_zV_x} & \frac{2(a^2C_f + b^2C_r)}{I_zV_x} \end{bmatrix} \begin{Bmatrix} V_y \\ r \end{Bmatrix} + \begin{bmatrix} \frac{-2C_f}{M} \\ \frac{-2aC_f}{I_z} \end{bmatrix} \delta_f \tag{A.9}$$

Vehicle sideslip angle, β in Figure 4, is defined as the angle between the longitudinal axis of the vehicle, and the velocity vector at the center of gravity.

$$\beta = \arctan\left(\frac{V_y}{V_x}\right) \cong \frac{V_y}{V_x} \tag{A.10}$$

Substitution of the above equation into Equation A.9 yields Equation 1 and concludes the derivation.

Appendix B: Pacejka Tire Model Coefficients

Road surface/coefficient	B_x	p_{Kx}	B_y	C_x	C_y	E_x	E_y	$r_{Bx/y1}$	r_{Bx2}	r_{By2}
Dry asphalt μ=1	$p_{Kx}/\mu/C_x$	12	8	1.45	1.42	-0.8	-1	7	8	9
Wet asphalt μ=0.5		9	10.28	1.05	1.2	-1	-0.75			
Snow μ=0.2		7	10.43	1	1.15	-0.7	-0.7			
Ice μ=0.1		5	10.45	1	1.1	-0.7	-0.7			

Appendix C: Variation of Longitudinal and Lateral Forces with respect to Slip

From Equation 30, the variation of longitudinal force with respect to longitudinal slip can be derived as:

$$\frac{\partial F_{xi}}{\partial s_i} = \mu_i F_{zi} \left\{ \frac{N_1 N_2 N_3}{D1} + \frac{N_4 N_5 N_6}{D2} \right\} \tag{C.1}$$

where

$$D1 = 1 + \left[B_x s_i - E_x \left(B_x s_i - \arctan(B_x s_i) \right) \right]^2 \tag{C.2}$$

$$D2 = \left\{ 1 + \left[r_{Bx1} \cos\left(\arctan\left(r_{Bx2} s_i \right) \right) \alpha_i \right]^2 \right\} \left[1 + \left(r_{Bx2} s_i \right)^2 \right] \tag{C.3}$$

$$N_1 = B_x C_x \left[1 - E_x \left(1 - \frac{1}{1 - B_x^2 s^2} \right) \right] \tag{C.4}$$

$$N_2 = \cos\left\{ C_x \arctan\left[B_x s_i - E_x \left(B_x s_i - \arctan(B_x s_i) \right) \right] \right\} \tag{C.5}$$

$$N_3 = \cos\left\{ \arctan\left[r_{Bx1} \cos\left(\arctan(r_{Bx2} s_i) \right) \alpha_i \right] \right\} \tag{C.6}$$

$$N_4 = \sin\left\{ C_x \arctan\left[B_x s_i - E_x \left(B_x s_i - \arctan(B_x s_i) \right) \right] \right\} \tag{C.7}$$

$$N_5 = \sin\left\{ \arctan\left[r_{Bx1} \cos\left(\arctan(r_{Bx2} s_i) \right) \right] \right\} \tag{C.8}$$

$$N_6 = r_{Bx2} r_{Bx1} \alpha_i \sin\left[\arctan\left(r_{Bx2} s_i \right) \right] \tag{C.9}$$

From Equation 31, the variation of lateral force with respect to longitudinal slip can be derived as:

$$\frac{\partial F_{yi}}{\partial s_i} = \mu_i F_{zi} \left\{ \frac{N_7 N_8 N_9}{D_3} \right\} \tag{C.10}$$

$$D_3 = 1 + \left[r_{By1} \cos\left(\arctan\left(r_{By2} \alpha_i \right) \right) s_i \right]^2 \tag{C.11}$$

$$N_7 = -r_{By1} \cos\left[\arctan\left(r_{By2} \alpha_i \right) \right] \tag{C.12}$$

$$N_8 = \sin\left\{ C_y \arctan\left[B_y \alpha_i - E_y \left(B_y \alpha_i - \arctan(B_y \alpha_i) \right) \right] \right\} \tag{C.13}$$

$$N_9 = \sin\left\{ \arctan\left[r_{By1} \cos\left(\arctan(r_{Bx2} \alpha_i) \right) s_i \right] \right\} \tag{C.14}$$

Appendix D: Fixed Point Control Allocation Algorithm Implemented within an Embedded Matlab Function in Simulink

```
function [U,alpha,n,k,er,T] =
fcn(B11,B12,B13,B14,B31,B32,B33,B34,ep,W_v,W_u,Fx,Md,d_threshold,u_max)
v_d=transpose([Fx Md]); %desired longitudinal force and yaw moment coming from the
high level controller
B=[B11 B12 B13 B14;B31 B32 B33 B34]; %control effectiveness matrix
T=(1-ep)*transpose(B)*W_v*B+ep*W_u; %cost function
n = 1/norm(T,'fro');
alpha=norm(eye(4)-n*T);
k = 1;
U_0=transpose([0 0 0 0]); %initial guess
d = [0.01 0.01 0.01 0.01]'; %accuracy tolerance
U = U_0;
%the iteration
while norm(d)>d_threshold
U=(1-ep)*n*transpose(B)*W_v*v_d-(n*T-eye(4))*U_0;
d=U-U_0;
k = k + 1;
```

```
U_0=U;
for i=1:length(U)
   if U(i)<u_max && U(i)>-u_max %u_max is the slip corresponding to the peak point of the force vs. slip curve
      U(i)=U(i);
   elseif U(i)>=u_max
      U(i)=u_max;
   else
      U(i)=-u_max;
   end
end
end
er=norm(d);
```

Appendix E: CAN Signal List for the Real Time Simulations

Table 3 CAN signal list

Signal	Length bit	Byte order	Unit	Value type	Factor	Offset	Min	Max
Wheel speed	16	Motorola	rad/s	unsigned	0.0125	0	0	819.1875
Motor torque command	16	”	Nm	signed	0.01	0	-327.68	327.67
EHB torque command	16	”	Nm	unsigned	0.03	0	0	1966.05
Lateral/longitudinal acceleration	16	”	m/s^2	signed	0.001	0	-32.768	32.767
Yaw rate	16	”	deg/s	signed	0.001	0	-32.768	32.767
Steering angle	16	”	deg	signed	0.025	0	-819.2	819.175
Accelerator/brake pedal position	16	”	%	unsigned	0.002	0	0	131.07
Roll rate	16	”	deg/s	signed	0.001	0	-32.768	32.767

References

[1] Simpson, A. 2006 "Cost-Benefit Analysis of Plug-In Hybrid Electric Vehicle Technology" *22nd International Battery, Hybrid and Fuel Cell Electric Vehicle Symposium and Exhibition (EVS-22)*, Yokohama, Japan.

[2] Elgowainy, A., Burnham, A., Wang, M., Molburg, J. and Rousseau A. 2009 "Well-to-Wheels Energy Use and Greenhouse Gas Emissions Analysis of Plug-in Hybrid Electric Vehicles" *Argonne National Laboratory Report*, available at http://www.transportation.anl.gov/pdfs/TA/559.pdf

[3] Interview with *Prof. Giorgio Rizzoni*, director of the Center for Automotive Research at The Ohio State University, 2009. (Available at http://www.youtube.com/watch?v=e-OqICweCVQ)

[4] Bosch. "*Driving Stability Systems*", 2005 Edition, Robert Bosch GmbH.

[5] Langwieder, K. 1999 "Mit ESP schwere Unfälle vermeiden oder mildern" *ESP-Workshop*, Boxberg, Germany.

[6] Ferguson S. A. 2007 "The effectiveness of electronic stability control in reducing real-world crashes: a literature review", *Traffic Injury Prevention* Vol. 8 (4), pp. 329-338.

[7] The United States Insurance Institute for Highway Safety report on Vehicle Accidents, 2006. (Available at http://www.iihs.org/news/rss/pr061306.html)

[8] VSC regulation that will be imposed on US market vehicles. (Available at http://www.nhtsa.gov)

[9] Mokhiamar, O., Abe, M. 2002 "Effects of model response on model following type of combined lateral force and yaw moment control performance for active vehicle handling safety", *JSAE* Review 23, pp. 473-480.

[10] Zheng, S., Tang, H., Han, Z., and Zhang, Y., 2006. "Controller design for vehicle stability enhancement". *Control Engineering Practice*, 14, pp. 1413-1421.

[11] Morgando, A. 2006 "Linear Approach to ESP Control Logic Design", *SAE* Paper 2006-01-1017.

[12] Van Zanten A., T. 2000 "Bosch ESP Systems: 5 Years of Experience" *SAE* paper 2000-01-1633.

[13] Shibahata, Y. Shimada, K., Tomari, T. 1993 "Improvement of Vehicle Maneuverability by Direct Yaw Moment Control", *Vehicle Systems Dynamics*, 22, pp. 465 – 481.

[14] Inagaki, S., Kshiro, I., Yamamoto, M. 1994 "Analysis on Vehicle Stability in Critical Cornering Using Phase-Plane Method", *AVEC'94*, International Symposium on Advanced Vehicle Control, October 24 – 28, pp. 287 – 292.

[15] Nguyen, V. 2005. "Vehicle Handling, Stability and Bifurcation Analysis for Non-linear Vehicle Models", *Master of Science Thesis*, University of Maryland.

[16] Shen, S., Wang, J., Peng, S., and Premier, G. 2007. "Nonlinear dynamics and stability analysis of vehicle plane motions", *Vehicle System Dynamics*, Vol. 45, No. 1, January, pp. 15-35.

[17] Liaw, D, and Chung, W. 2008. “A feedback linearization design for the control of vehicle’s lateral dynamics”. Nonlinear Dynamics, 52, pp. 313-329.

[18] Boada, B. L., Boada, M. J. L. and Diaz, V. 2005. “Fuzzy Logic Applied to Yaw Moment Control for Vehicle Stability”. *Vehicle System Dynamics*, Vol. 43, No. 10, October, pp. 753-770.

[19] Cheong, J., Eom, W, and Lee, J. 2009. “Cornering Stability Improvement for 4 Wheel Drive Hybrid Electric Vehicle”, *IEEE International Symposium on Industrial Electronics*, July.

[20] Li, D. Y., Liu, W., Li, J., Ma, Z. M., and Zhang, J. C. 2005 “Simulation of vehicle stability control system using fuzzy PI control method” *IEEE International Conference on Vehicle Electronics and Safety*, pp. 165-170.

[21] Kim, D., Hwang, S., and Kim, H. 2008 “Vehicle Stability Enhancement of Four-Wheel-Drive Hybrid Electric Vehicle Using Rear Motor Control” *IEEE Transactions on Vehicular Technology*, Vol. 57, No. 2, March, pp. 727-735.

[22] Wang, J. and Longoria, R. G. 2009. “Coordinated and Reconfigurable Vehicle Dynamics Control”, *IEEE Transactions on Control System Technology*, Vol. 17, No 3, May, pp. 723-732.

[23] Mokhiamar, O. and Abe, M. 2006. “How the four wheels should share forces in an optimum cooperative chassis control” Control Engineering Practice, 14, pp. 295-304.

[24] Zhou, Q., and Wang, F. 2004 “Driver Assisted Fuzzy Control of Yaw Dynamics for 4WD Vehicles”, *IEEE Intelligent Vehicles Symposium,* June.

[25] Tjonnas, J. and Johansen, T. A. 2006. "Adaptive optimizing dynamic control allocation algorithm for yaw stabilization of an automotive vehicle using brakes", *IEEE 14th Mediterranean Conference on Control and Automation*, pp. 1-6.

[26]Kiencke, U. and Nielsen, L. 2000. "*Automotive Control Systems*", Springer – Verlag.

[27] Tekin. G., and Unlusoy, Y. S., 2010. "Design and simulation of an integrated active yaw control system for road vehicles" *International Journal of Vehicle Design*, Vol. 52, No.1/2/3/4, pp. 5-19.

[28] Buckholtz, K. R. 2002. "Use of Fuzzy Logic in Wheel Slip Assignment-Part 1: Yaw Rate Control", *SAE Transactions*, 2002-01-1221.

[29] Buckholtz, K. R. 2002. "Use of Fuzzy Logic in Wheel Slip Assignment-Part 2: Yaw Rate Control with Sideslip Angle Limitation", *SAE Transactions*, 2002-01-1220.

[30] Tahami, F., Farhangi, S., and Kazemi, R. 2004. "A Fuzzy Logic Direct Yaw Moment Control System for All-Wheel-Drive Electric Vehicles". *Vehicle System Dynamics*, Vol. 41, No. 3, pp. 203-221.

[31] Passino, K. M. and Yurkovich, S. 1998. "*Fuzzy Control*", 1st Ed., Addison-Wesley.

[32] Smakman H. 2000. "Functional Integration of Active Suspension with Slip Control for Improved Lateral Vehicle Dynamics", Proceedings of AVEC 2000.

[33] Manning, W. J.,Crolla, D. A. 2007. "A review of yaw rate and sideslip controllers for passenger vehicles" *Transactions of the Institute of Measurement and Control* 29, 2, pp. 117–135.

[34] EcoCAR competition organized by Department of Energy and GM. (Available at http://www.ecocarchallenge.org)

[35] Bayar, K., Bezaire, B., Cooley, B., Kruckenberg, J., Schacht, E., Midlam-Mohler, S., and Rizzoni, G. 2010 “Design of an Extended-Range Electric Vehicle for the EcoCAR Challenge” submitted to *ASME 2010 International Design Engineering Technical Conferences & Computers and Information in Engineering Conference*.

[36] Schacht, E., Bezaire, B., Cooley, B., and Bayar, K. 2011 “Addressing Drivability in an Extended Range Electric Vehicle Running an Equivalent Consumption Minimization Strategy (ECMS)” *SAE* paper 2011-01-0911.

[37] T. D. Gillespie, *Fundamentals of Vehicle Dynamics*. 1992. Warrendale, PA: SAE.

[38] Dspace Automotive Simulation Models 2010. (Available at http://www.dspace.com/de/pub/home/support/suptrain/hardware_in_the_loop/asm_vehicle_dynamics.cfm)

[39] Borchsenius, F. 2003. “Simulation olhydraulischer Systeme”, Fortschritt-Berichte VDI Reihe 8 Nr. 1005, VDI-Verlag, Dusseldorf.

[40] Backe, W. and Murenhoff, H. 1994 “Grundlagen der Olhydraulik“, Umdruck zur Vorlesung, *Institut fur fluidtechnische Antriebe und Steuerungen der Rheinisch-Westfalischen Hochschule Aachen*, 10 Auflage.

[41] Beater, P. 1999 “Entwurf hydraulischer Maschinen”, Springer, Berlin.

[42] Seewald, D. 1997 “Erstellung eines realitatsgetreuen, physikalischen Erstatzmodells der Mechanik und Hydraulik eines Anti-Blockiersystems als Basis fir ein mechatronisches Gesamtmodell“, *Diplomarbeit*, MLaP, Paderborn.

[43] Reuter, D., F., Lloyd, E. W., Zehnder, J. W., and Elliott, J. A. 2003 ‘Hydraulic Design Considerations for EHB Systems’, *SAE* paper 2003-01-0324.

[44] Pacejka, A., 2006. “Tire and Vehicle Dynamics”, 2nd ed, Elsevier.

[45] Esmailzadeh, E., Vossoughi, G., R., and Goodarzi, A., 2001. “Dynamic Modeling and Analysis of a Four Motorized Wheels Electric Vehicle”. *Vehicle System Dynamics*, Vol. 35, No. 3, pp. 163-194.

[46] Esmailzadeh, E., Vossoughi, G., R., and Goodarzi, A., 2003. “Optimal yaw moment control law for improved vehicle handling”. *Mechatronics*, 13, pp. 659–675.

[47] Goodarzi, A., and Esmailzadeh, E., 2007. “Design of a VDC System for All-Wheel Independent Drive Vehicles”. *IEEE/ASME Transactions on Mechatronics*, Vol. 12, No. 6, December, pp. 632-639.

[48] Segel, L. 1957 “Theoretical prediction and response of the automobile to steering control” *Research in Automobile Stability and Control in Tire Performance*, Proceedings of the Automobile Division of The Institution of Mechanical Engineers, 1956-57, No. 7, pp. 26-46.

[49] Transportation Research Center Inc. testing capabilities. (Available at http://www.trcpg.com/)

[50] Watanabe, K., Kobayashi, K., Cheok, K. J. 1992 “Absolute Speed Measurement of Automobile from Noisy Acceleration and Erroneous Wheel Speed Information”, *SAE* paper 920644.

[51] Song, C.K., Uchanski, M., Hedrick, J. K. 2002 ”Vehicle Speed Estimation Using Accelerometer and Wheel Speed Measurements” *SAE* paper, 2002-01-2229.

[52] Hahn, J., Rajamani, *R.* and Alexander, L. 2002 “GPS-Based Real-Time Identification of Tire–Road Friction Coefficient”, IEEE Transactions of Control Systems Technology, VOL. 10, NO. 3, pp 331-343.

[53] Wang, J., Alexander, L. and Rajamani, R. 2004 “Friction Estimation on Highway Vehicles Using Longitudinal Measurements” *Journal of Dynamic Systems, Measurement, and Control*, Vol 126, n2, pp 265-275.

[54] Rajamani, R., Piyabongkarn D., Lew, J. Y. and Grogg, J. A. 2006 “Algorithms for Real-Time Estimation of Individual Wheel Tire-Road Friction Coefficients“ *Proceedings of the 2006 American Control Conference*, Minneapolis, Minnesota, USA, June 14-16, 2006, pp 4682-4687.

[55] Huang, J., Ahmed, J., Kojic, A. and Hathout, J. 2004 “Control Oriented Modeling for Enhanced Yaw Stability and Vehicle Steerability” *Proceeding of the 2004 American Control Conference*, July.

[56] Anwar, S. 2005 “Generalized predictive control of yaw dynamics of a hybrid brake-by-wire equipped vehicle” *Mechatronics*, 15, pp. 1089–1108.

[57] Hancock, M. and Assadian, F. 2006. “Impact of regenerative braking on vehicle stability” IEEE.

[58] Falcone, P., Pakazad, S. K., and Solyom, S. 2009. Predictive Approaches to Rear Axle Regenerative Braking Control in Hybrid Vehicles” *Joint 48th IEEE Conference on Decision and Control and 28th Chinese Control Conference*, Shanghai, P.R. China, December.

[59] Fredrikson, J., Andreasson, J. and Laine, L. 2004. “Wheel Force Distribution for Improved Handling in a Hybrid Electric Vehicle using Nonlinear Control”, *43rd IEEE Conference on Decision and Control*, December.

[60] Plumlee, J. H., Bevly, D. M, and Hodel, A. S. 2004. “*Proceedings of the 2004 American Control Conference*”.

[61] Simmons, A. T. 2003 “Control Allocation Techniques using Existing and Novel Quadratic Programming Algorithms” *Master's thesis*, Auburn University, August.

[62] Wang, J. 2007 “Coordinated and Reconfigurable Vehicle Dynamics Control” *PhD Dissertation*, The University of Texas at Austin.

[63] Lu, P. 1996. “Constrained Tracking Control of Nonlinear Systems” *Systems and Control Letters*. Vol. 27, pp. 305-314.

[64] Khalil, H. K. 2002. “Non-linear Systems”, 2nd Edition. Prentice Hall.

[65] Johansen, T. A., Petersen, I., Kalkuhl, J., and Ludemann, J. 2003. “Gain-scheduled wheel slip control in automotive brake systems” *IEEE Transactions on Control Sytem Technology*, 11: 799-811

[66] Tanelli, M., Astolfi, A., and Savaresi, S. M. 2008. “Robust nonlinear output feedback control for brake by wire control systems” *Automatica* 44, pp. 1078-1087.

[67] Pasillas-Lepine, W. and Loria, A. 2010 “A New Mixed Wheel Slip and Acceleration Control Based on a Cascaded Design”, *8th IFAC Symposium on Nonlinear Control Systems*, Sept 1-3, University of Bologna.

[68] Chun, K. and Sunwoo, M., 2005, “Wheel slip tracking using moving sliding surface” *Proceedings of the IMechE*, Vol. 219, Part D: Automobile Engineering, pp. 31–41.

[69] Solyom, S. and Rantzer, A. 2002. “Nonlinear and Hybrid systems in Automotive Control. ABS Control-A design model and Control Structure”. *Springer Verlag*, New Jersey.

[70] Beer, F., P. and Johnston, E., R. Mechanics of Materials, metric edition.

[71] DSpace HIL and MicroAutoBox. (Specifications available at http://www.dspaceinc.com)